**University of Crete, Physics Department**
**Foundation for Research and Technology-Hellas**
**Institute of Electronic Structure and Laser**

# *The influence of structure on ultrafast electron dynamics in non-stoichiometric III-V semiconductors and metallic nano-composites*

**Panagiotis A. Loukakos**

**Πανεπιστήμιο Κρήτης, Τμήμα Φυσικής**
**Ίδρυμα Τεχνολογίας και Έρευνας**
**Ινστιντούτο Ηλεκτρονικής Δομής και Laser**

# *Η επίδραση της δομής στην υπερταχεία ηλεκτρονιακή δυναμική σε μη-στοιχειομετρικούς III-V ημιαγωγούς και μεταλλικές νανο-συνθέσεις*

**Παναγιώτης Αριστοτέλους Λουκάκος**

A thesis presented on Tuesday, April 2nd, 2002, in the Physics Department of the University of Crete, in front of the following committee

| | |
|---|---|
| Prof. | Constantinos Fotakis |
| Assoc. Prof. | Ilias Perakis |
| Assoc. Prof. | Panagiotis Tzanetakis |
| Prof. | Eleftherios Economou |
| Prof. | Nikolaos Papanikolaou |
| Assoc. Prof. | Dimitrios Charalampidis |
| Assis. Prof. | Zacharias Hatzopoulos |
| Scient. Advisor | Constantinos Kalpouzos |

to obtain the degree of

***Doctor of Philosophy***

in Physics

*τοῖς μέν εὖ πράττειν*

*ἅπας ὁ βίος βραχύς ἐστίν*

*τοῖς δέ κακῶς*

*μία νύξ ἄπλετος χρόνος*

ανώνυμος

***for those who do good***

***a whole lifetime is short***

***for those who do evil instead***

***one night’s time is abundant***

anonymous

***to my parents,***

***Αριστοτέλη and Μαρία***

# Acknowledgements

It is my wish to express to the future reader how lucky I feel that God gave me my parents, General *Aristoteles Loukakos* and *Maria Loukakou*, whose ethics and honesty brought me up and made me above all what I hope to be a proper human being. Without their support I could have done nothing and I can only say that the word “*gratitude*” is too constrictive to describe my feelings for them.

My basic studies occurred in the Physics Department of the University of Crete and therefore I wish to acknowledge the contribution of my teachers in introducing me to the basics of physics, thus giving me the proper tools to move on to postgraduate studies, again in the same school.

During my postgraduate studies, I was brought in touch with the Director of the nearby Institute of Electronic Structure and Laser of the Foundation for Research and Technology – Hellas, Professor *Constantinos Fotakis*, who gave me the opportunity to work in the laboratories of the Ultrafast Laser Facility.

There, under the expert guidance of my supervisor and friend Doctor *Constantinos Kalpouzos*, I was able to carry out the experiments needed for the work presented in this thesis. Costa, thank you for your patience.

I wish to thank all the members of my thesis committee. Special thanks belong to Professor *Ilias Perakis* and Professor *Panagiotis Tzanetakis* whose support was unmatchable and Professor *Zacharias Hatzopoulos* with whom the collaboration was excellent.

Special thanks to Professor *Christos Flytzanis*, and my friends Doctor *Fabrice Vallee* and Doctor *Cristophe Voisin*. They gave me the possibility to carry out a very important part of this work in the Laboratoire d'Optique Quantique of Ecole Polytechnique. Their expertise made me learn a lot during my stay in Paris, and their friendliness and warmth helped me adapt quickly and easily in a new environment.

I wish to thank Mister *Michalis Sfendourakis* and Doctor *George Konstantinides*. They spend infinite hours of hard work for the special treatment of the semiconductor specimens, without asking anything in return.

Many thanks to Professor *Ioannis Stoimenos* from the Aristoteles University of Thessaloniki, who made possible the structure characterization of the semiconductor specimens.

The laboratory staff in the Institute of Electronic Structure and Laser, helped me in one way or another. It is only because of lack of space that I am not acknowledging each and every one and I am sorry for this. Thanks guys.

The professionalism of the secretaries of the Institute and friends of mine, Miss *Magda Kokolaki* and Mrs. *Ritsa Karali* is worth noticing. Without their support, I am afraid that there would be a lot of delay in this work.

Last but not least, I wish to acknowledge my friends. They tolerated me and all the peculiarities that I have grown during the past years. My gratitude belongs to my friend Doctor *Nektarios Papadogiannis* who is the person that introduced me in the "laboratory world" and taught me a lot about experimental physics during my first steps in this area. Also, many thanks to all the students of the Physics Department with whom I always had a useful interaction.

I thank you all.

# Abbreviations & Notations

| | |
|---|---|
| s | Second |
| µs | Microsecond=$10^{-6}$ s |
| ns | Nanosecond=$10^{-9}$ s |
| ps | Picosecond=$10^{-12}$ s |
| fs | Femtosecond=$10^{-15}$ s |
| m | Meter |
| cm | Centimetre=$10^{-2}$ m |
| mm | Millimeter=$10^{-3}$ m |
| µm | Micrometer=$10^{-6}$ m |
| nm | Nanometer=$10^{-9}$ m |

| | |
|---|---|
| Å | Angstrom=$10^{-10}$ m |
| V | Volt |
| Nt | Newton |
| J | Joule=Ntm |
| eV | Electron Volt=$1.6\times10^{-19}$ J |
| W | Watt=Js$^{-1}$ |
| $^{o}$C | Celsius degree |
| $^{o}$K | Kelvin degree |
| Hz | Hertz=s$^{-1}$ |
| rad | Radian |
| ħ | Planck constant=$6.62607\times10^{-34}$ Js |
| δ-function | Delta-function: $\int_{-\infty}^{+\infty}\delta(x)dx=1$ |
| Erf | Error function: $Erf(t)\equiv\frac{2}{\sqrt{\pi}}\int_{0}^{t}e^{-\tau^2}d\tau$ |
| Ag | Silver |
| Al | Aluminium |
| As | Arsenic |

| | |
|---|---|
| Au | Gold |
| F | Fluoride |
| Ga | Gallium |
| H | Hydrogen |
| Mg | Magganium |
| Nd | Neodymium |
| O | Oxygen |
| S | Sulphur |
| Si | Silicon |
| Ti | Titanium |
| Sapph | Sapphire |
| AlAs | Aluminum Arsenide |
| AlGaAs | Aluminum Gallium Arsenide |
| GaAs | Gallium Arsenide |
| a.u | Arbitrary units |
| BBO | Barium Borate Oxide |
| CC | Cross correlation |

| | |
|---|---|
| CCD | Charge Coupling Device |
| CW | Continuous wave |
| LBO | Lithium Triborate |
| LO | Longitudinal optical |
| LTG | Low-temperature-grown |
| MBE | Molecular Beam Epitaxy |
| PC | Personal Computer |
| PLL | Phase Locked Loop |
| PSD | Phase Sensitive Detection |
| RHEED | Reflection High – Energy Electron Diffraction |
| SPR | Surface Plasmon Resonance |
| TEM | Transmission Electron Microscopy |
| $TEM_{00}$ | Transverse Electromagnetic Mode |

# Table of Contents

Περίληψη 1

Abstract 3

1 Introduction 5

2 Experimental Details 17

2.1 Introduction 17

2.2 Laser Systems 17

2.2.1 The commercial laser system 18

2.2.2 The home made laser system 20

2.3 Ultrafast pump and probe spectroscopy 21

2.4 The lock-in detection 27

2.5 Experimental arrangement 29

2.5.1 Detection principle 29

2.5.2 Degenerate pump-probe setup 31

2.5.3 Non-degenerate pump-probe setup 35

2.6 Laser parameter characterization: spectrum and pulse duration 35

2.7 Transmission Electron Microscopy 42

2.8 References 43

3 III-V Semiconductors: Background 45

3.1 Introduction 45

3.2 Structure 45

3.2.1 Stoichiometric GaAs 46

3.2.2 Stoichiometric AlGaAs and alloys 49

3.2.3 Non stoichiometric GaAs 50

3.2.4 Non stoichiometric AlGaAs 53

3.3 Optical properties 54

3.4 Relaxation Mechanisms 57

3.4.1 Carrier-carrier scattering 57

3.4.2 Carrier-phonon scattering 59

3.4.3 Carrier recombination and diffusion 61

3.5 References 65

4 GaAs & AlGaAs: Electron Trapping 69

4.1 Introduction 69

4.2 Growth and preparation 71

4.3 Sample characterization 73

4.3.1 Structure characterization 73

4.3.2 Optical characterization 81

4.4 Experimental results 83

4.5 Discussion 98

4.6 Conclusions 114

4.7 References 115

5 Metallic Nanocposites: Background 119

5.1 Introduction 119

5.2 Structure of Au 119

5.3 Optical properties 122

5.4 Relaxation mechanisms 127

Appendix 133

5.5 References 135

6 Au Nanocrystals: Electron Dynamics 137

6.1 Introduction 137

6.2 Sample preparation 139

6.3 The pump-probe experiment 141

6.3.1 Typical measurements and phenomenological description 141

6.3.2 Electron-lattice thermalization: Results 149

6.3.3 Electron-lattice thermalization: Discussion 153

6.3.4 Electron-electron thermalization: Results 156

6.3.5 Electron-electron thermalization: Discussion 161

6.4 Conclusions 171

6.5 References 172

7 Summary 177

# Περίληψη

Η τεχνική της υπερταχείας φασματοσκοπίας άντλησης – ανίχνευσης χρησιμοποιήθηκε ώστε να μελετηθεί η ηλεκτρονιακή συμπεριφορά παγίδευσης σε μη-στοιχειομετρικό GaAs και AlGaAs και για να μελετηθεί η επίδραση της μείωσης του μεγέθους νανοσωματιδίων Au στην κινητική κατάσταση του ηλεκτρονιακού πληθυσμού τους.

Η δυναμική κατάσταση των ηλεκτρονίων της ζώνης αγωγιμότητας σε Χαμηλής-Θερμοκρασίας-Ανάπτυξης GaAs και AlGaAs μελετάται μέσω διέγερσης ηλεκτρονίων στην περιοχή του πυθμένα της ζώνης αγωγιμότητας και ανίχνευσης των επαγώμενων μεταβατικών αλλαγών στην απορρόφηση από την κορυφή της ζώνης σθένους προς τον πυθμένα της ζώνης αγωγιμότητας του ημιαγωγού. Οι μη-στοιχειομετρικοί ημιαγωγοί που εξετάζουμε περιέχουν συσσωματώματα As. Η συμπεριφορά παγίδευσης των ηλεκτρονίων βρίσκεται να εξαρτάται από τη μέση ακτίνα $\alpha$ και τη μέση απόσταση $R$ των συσσωματωμάτων As. Η αλληλοσυσχέτιση αυτών των δύο παραμέτρων για πρώτη φορά προκύπτει πειραματικά να καθορίζεται από το νόμο $\tau \propto \frac{R^3}{\alpha}$, ο οποίος μπορεί να προβλεφθεί θεωρητικά υποθέτοντας παγίδευση των ηλεκτρονίων στις επιφάνειες των συσσωματωμάτων As εν μέσω διάχυσης.

Η κινητική κατάσταση των περιορισμένων, μέσα σε νανοσωματίδια Au, ηλεκτρονίων μελετάται μέσω διατάραξης του ηλεκτρονιακού πληθυσμού στην περιοχή της ενέργειας Fermi και ανίχνευσης των μεταβατικών διαζωνικών μεταβάσεων από τις ζώνες-d προς την επιφάνεια Fermi. Από την πειραματική μελέτη προκύπτει μία επιτάχυνση του μηχανισμού της εσωτερικής ηλεκτρονιακής ανακατομής της ενέργειας με τη μείωση (αύξηση) του μεγέθους του νανοσωματιδίου (περιορισμού). Τα αποτελέσματα δείχνουν μία ανεξαρτησία από τον περιβάλλοντα διηλεκτρικό ξενιστή και βρίσκεται σε συμφωνία με ένα αριθμητικό πρότυπο βασισμένο στην μείωση της θωρακισμένης αλληλεπίδρασης Coulomb. Ομοίως, ο μηχανισμός της ψύξης του θερμοποιημένου ηλεκτρονιακού πληθυσμού προς το πλέγμα επιταχύνεται με τη μείωση του μεγέθους.

# Abstract

Ultrafast pump and probe spectroscopy has been utilized in order to study the electronic trapping behavior in nonstoichiometric GaAs and AlGaAs and to study the effect of the size reduction of nanometer sized Au particles on the kinetics of the confined electron population.

The dynamics of conduction band electrons of Low-Temperature-Grown GaAs and AlGaAs is studied by exciting electrons in the vicinity of the conduction band bottom and by probing the induced transient changes in the absorption from the top of the valence to the bottom of the conduction band of the semiconductor. The nonstoichiometric semiconductors, that we examine, contain As precipitates. The electron trapping behavior is found to depend on both the average As precipitate radius $\alpha$ and spacing $R$. The interplay of these parameters is for the first time experimentally determined to be governed by the law $\tau \propto \frac{R^3}{\alpha}$ which can be predicted theoretically by assuming diffusion mediated trapping of electrons on the surfaces of the As precipitates.

The kinetics of the confined electrons in Au nanoparticles is studied by perturbing the electron population in the vicinity of the Fermi energy and by probing the transient interband transition from the d-bands to the Fermi surface. The mechanism of the internal electron energy re-distribution is experimentally found to accelerate with the reduction (enhancement) of the nanoparticle size (confinement). The results show an independency of the surrounding dielectric host and are in good agreement with a numerical model based on the reduction of the Coulomb screening interaction. The mechanism of the cooling of the thermalized electron population to the lattice is also found to accelerate with size reduction.

# Chapter 1 Introduction

The past two decades newly developed condensed phase materials have attracted the interest of various research groups for their high nonlinearities and their ultrashort electronic response times. Semiconductors grown in lower than the usual temperature [Delaney] or intentionally enriched with selected impurities, [Walukiewicz] metals confined to dimensions where the distinction between the separate atom behavior and the bulk material becomes unclear, [Flytzanis] are some examples of novel materials that exhibit unique properties distinguishable from the bulk and can be used in modern optoelectronic devices to meet the need for more powerful and faster signal processing applications.

In the late 80's and the early 90's, research groups discovered that growing Gallium Arsenide (GaAs) in lower than the normal growth temperature (~ 200 $^{o}$C instead of ~ 600 $^{o}$C) results in a nonstoichiometric material. [Kaminska] Such growth has been first used to overcome back-gating effects in circuits that reduced the quality of electronic devices. [Smith] Stoichiometry measurements in such materials showed that a small percentage of excess Arsenic (As) is incorporated in the GaAs matrix (~ 1 %) during growth. The excess As is found mainly in the form of antisite defects and caused an increase (~ 0.1 %) in the lattice parameter of the crystal, [Kaminska] thus reducing its symmetry and its potential applications. However, special thermal treatment (annealing) of the nonstoichiometric material results in the reduction of the As antisite defect concentration, thus gradually leading to reduction of the lattice parameter down to the bulk GaAs value. [Kaminska] The annealed material is found to still contain excess As but in the form of precipitates (clusters), with a size of a few nanometers, rather than in the form of antisite (point) defects. [Melloch] This observation has proven its importance by giving researchers a good crystalline material which is nonstoichiometric and which can be used to enhance the electronic properties of transistors. This material exhibits high resistivity, high crystalline quality and simultaneously relatively high carrier mobility [Kaminska] thus being a very powerful element in constructing state of the art electronic devices.

Shortly after the discovery of Low-Temperature-Grown Gallium Arsenide (LTG-GaAs) it has been demonstrated that this material can be used as a very fast photoconductive switch with ultrafast response times. [Warren] So far, all transistors and semiconductor based circuits were based on Silicon (Si) and related materials. These have very high structural quality but switching applications are limited by the Si carrier lifetime which lies in the order of 1 ns. Now, researchers could pay attention to a new material (LTG-GaAs) that lowered this time limit by three orders of magnitude down to 1 ps and maybe even lower.

The very fast photoconductive switching can only be attributed to the ultrafast carrier dynamics of the semiconductor. Therefore, a number of researchers have since then, tried to understand the basic mechanisms that are involved in the dynamics of the optically generated carriers. The carrier lifetime has been found to strongly depend on the growth conditions (temperature and annealing) of the GaAs. [Harmon] The adjustment of the growth conditions gives the possibility to tailor the material's ultrtafast electronic properties in a controllable and predictable manner. [Smith2] Researchers could now manufacture materials that exhibit carrier lifetime in the order of a few ps or even shorter. So, now this material could be very promising for a variety of not only electronic but also optoelectronic devices and applications.

However, despite of the strong effort to characterize the ultrafast optical properties of these materials, the underlying mechanisms that govern the ultrafast carrier kinetics are still unclear. As a result, much of the expended effort to characterize the carrier dynamics hardly escapes recipes and fabrication procedures. There has been a strong debate in the literature to whether the observed ultrafast behavior has to be attributed to the point defect [Look] or the precipitate [Warren2] form of the excess As. Since the presence of the As precipitates is at the expense of point defects, the As precipitate approach has proven to be more valuable for the strongly annealed material. Since then, there appeared a scarce number of reports trying to associate the observed ultrafast behavior to the As precipitates and their characteristics, with however, little success since, until now, only empirical laws are used for this association. [Melloch2]

One scope of the thesis is to resolve the pending questions related to the connection of the ultrafast electronic behavior of semiconductors with the defects that are intentionally embedded in the host matrix. For this purpose, we chose the GaAs semiconductor because apart from being a typical representative of III-V semiconductors, it is the most favorite candidate in replacing Si and related compounds in the high-repetition rate and ultrafast optoelectronics area. It is our intention to formulate the relationship between the electron relaxation and the structure characteristics of the As precipitates in order to conclude about the mechanisms that are responsible for the ultrafast electronic behavior.

As an extension to these experiments we are also going to investigate the Aluminum Gallium Arsenide (AlGaAs) semiconductor. The AlGaAs material is chosen for two main reasons. First, it is going to be used as a test case, because, since it is a relevant material to GaAs it should be very important to verify the results that are going to be obtained. Second, AlGaAs has its own, distinct importance in the optoelectronics area. Apart from its usage in the quantum well construction technology, [Feng] the controlled amount of the Al mole fraction offers a unique feature: the bandgap energy of the semiconductor is controlled by the Al mole fraction. So, optoelectronic devices can be constructed that can be tuned to a desired wavelength. Therefore, good knowledge of the ultrafast electron dynamics of such a material is very beneficial.

The influence of the nanometric dimension structures inside semiconductors on the electronic behavior of the semiconductor is one field of interest. Another field of interest is the electronic behavior of these nanostructures themselves.

Between the well established domain of the atomic and molecular physics and that of the physics of condensed matter, there is an intermediate region that deals with the properties of small aggregates or clusters or small particles which are neither quite microscopic nor macroscopic in dimensions. The study of these intermediate size systems is very important from both fundamental and technological point of view. Catalysis, chemisorption, aerosols, powder metallurgy, ferrofluids are some examples that are related to the technology aspect. From a more fundamental point of view, the study of this intermediate state of matter (between a molecule or atom and the solid) is crucial and interesting because it can reveal some significant basic physical mechanisms that are usually “screened” when one deals with systems almost infinitely large in dimensions. [Perenboom]

Metal-doped glasses have a very long history. They have been used for centuries to fabricate the stained glasses that usually appear in cathedrals. However, the discovery of such materials was rather accidental and their fabrication empirical. The preparation of well-defined metal crystallites in controlled and reproducible conditions dates back to only a few decades. These include colloidal suspensions of metals, [Turkevich] particles in glasses [Stookey] or other solid matrices and free clusters in gases [Kimoto] or beams. In all cases the purpose is to produce particles with variable average size but with a very narrow size distribution and well characterized in shape and chemical constitution, since these features strongly influence the optical and electronic properties of the materials. [Flytzanis]

The optical properties of confined metallic systems have been extensively studied. The most conspicuous effect of the confinement of the system in its optical properties is the appearance of a morphological feature, the Surface Plasmon Resonance (SPR). This effect is attributed to the confinement of the system either quantum or dielectric. In the first case, where the confinement is very strong, in the metal nanocrystals where otherwise the valence electrons are delocalized to an infinite dimension, now their wavefunctions are localized to much smaller regions. In the second case, where the confinement is not very strong and the electronic wave functions can be considered to slightly differ from those of the bulk, but still, the size of the crystallites remains much smaller than the optical wavelength, the optical properties of the confined material are explained with the approach of the effective dielectric medium and with the fact that the electric field that acts and polarizes the charges of the crystallites can be vastly different from the macroscopic Maxwell field. [Flytzanis]

However, the ultrafast carrier kinetics in these materials are not yet well known and are a field of active and intense study. The scattering events inside such systems when brought under nonequilibrium conditions have been found to be strongly dependent on the confinement of the system with direct influence on the corresponding energy exchange rates between the electron and lattice subsystems. [DelFatti] The early stages associated with the electron-electron interactions, have only been extensively investigated in bulk metals before. [DelFatti2] Very little is known about the influence of the size reduction on the initial ultrafast electron kinetics that are responsible for the redistribution of the stored energy inside the electron subsystem alone. [Voisin] Therefore, further research is needed in order to facilitate the trend of the internal energy redistribution rate in the electron gas immediately after optical ultrafast perturbation.

The last goal of this thesis is to investigate the initial ultrafast electron dynamics in Gold (Au) nanocrystals in order to find whether the trends that are observed in only one other noble metal (Ag) [Voisin] can be extended to noble metal crystallites in general. Au is chosen for two main reasons: First, because of its extensive usage in various technological applications ranging from industry to even decoration. Second, because even though, as Ag, Au is a noble metal, it exhibits its SPR frequency very close to the threshold for interband transitions. So, Au gives us the possibility to investigate if the results that are obtained from the model system of Ag, where the SPR and the interband transition threshold are far apart, also apply in this case.

The interesting phenomena stated above are all dynamical in the sense that they are responsible for bringing a system from a perturbed state towards equilibrium. Thus, one must first perturb the under study system i.e. to bring it in a state away from equilibrium. However, one must be very cautious in choosing the means of the perturbation. For example, if the perturbation lasts for a longer time than the duration of phenomenon we are interested in, then the latter will remain well hidden. Therefore its dynamical evolution will be revealed only if our perturbative action vanishes well before the decay of the under study phenomenon.

Soon after the first demonstration of laser action, research started in the generation of ultrashort laser pulses. Although this research is still active, the scientific community has the opportunity of exploiting the advantages of ultrashort light pulses for the last two decades. Using pulsed light, we are able to study physical mechanisms that evolve in a time window comparable to, or greater than, the duration of the laser pulse. Thus, the shorter the pulse, the faster the physical mechanisms we can study. Current laser technology offers the possibility to study physical processes that take place in a time scale down to 100 fs and even shorter. [Shah] The trend of the future is towards laser systems with even shorter pulse widths in order to monitor sub-fs phenomena. [Papadogiannis]

Even though such laser systems offer the possibility to induce ultrafast responses and terminate long before the onset of decay, the monitoring of such phenomena is not trivial. Typical electronic based devices (i.e. oscilloscopes) offer a time-resolution of a few ns at the best. Even highly sophisticated devices like Streak-Cameras do not have the ability to follow the evolution of events with duration less than a few ps. Therefore, scientists need to develop all-optical techniques that are not restrained by the limited response time of electrical devices. [Othonos]

The most common form of ultrafast spectroscopy is the pump-probe spectroscopy. In its simplest form (degenerate pump-probe spectroscopy), the output pulse train is divided in two. The sample under investigation is excited by one pulse (pump) and the induced changes are probed by the second pulse train (probe), which is suitable delayed with respect to the pump by introducing an optical delay in its path. A property related to the probe (i.e. reflectivity, absorption, Raman scattering, luminescence) is then monitored to investigate the changes in the sample produced by the pump. In the non-degenerate case, one uses two synchronized lasers at different wavelengths. This increases the versatility of the technique enormously by allowing a determination of the changes induced at photon energies different from that of the pump. The time resolution in the pump and probe spectroscopy is mainly limited by the laser pulse duration. [Shah]

Apart from the above, many alterations can be made to this technique in order to optimize it for better performance according to the need of a specific experiment. More details for the techniques that are used for the experiments presented in this thesis are going to be stated in the next chapters.

Concluding, apart from the scopes of this thesis to investigate some ultrafast phenomena in matter, it is also our intention to demonstrate the use of the pump and probe spectroscopy in condensed matter and in the sub-ps regime. Thus, this thesis might also serve as a reference textbook for the (important) details that need to be taken into account in order to develop a know-how and deal with ultrafast, optical techniques.

The work has the following structure:

- The first chapter is the present introductive one.
- The second chapter presents the experimental details of this thesis such as the used laser systems, the principles of the ultrafast pump-probe spectroscopy and the experimental setups.
- The third chapter deals with the basic background concepts that are needed in order to investigate carrier dynamics in III-V semiconductors in general and GaAs and AlGaAs in particular.
- The fourth chapter deals with the experimental investigation of the electronic ultrafast dynamics of LTG-GaAs and LTG-AlGaAs.
- The fifth chapter deals with the background needed in order to investigate the electron dynamics in metallic crystallites.
- The sixth chapter presents the experimental investigation of the ultrafast electron kinetics in Au nanoparticles.
- The seventh chapter finally, summarizes the work done in this thesis and gives the basic results and conclusions obtained by the present experiments.

## References

| | |
|---|---|
| **Delaney** | M. J. Delaney, A. S. Brown, U. K. Mishra, C. S. Chou, L. E. Larson, L. Nguyen, and J. Jensen, Inst. Phys. Conf. Ser. **106**, 189 (1989). |
| **DelFatti** | N. Del Fatti, C. Flytzanis and F. Vallee, Appl. Phys. B **68**, 433 (1999). |
| **DelFatti2** | N. Del Fatti, C. Voisin, M. Achermann, S. Tzortzakis, D. Christofilos, and F. Vallee, Phys. Rev. B **61**, 16956 (2000). |
| **Feng** | W. Feng, Z. G. Zhang, Y. Yu, Q. Huang, P. M. Fu, and J. M. Zhou, J. Appl. Phys. **79**, 7404 (1996). |
| **Flytzanis** | C. Flytzanis, F. Hache, M. C. Klein, D. Ricard, and P. Roussignol, “Nonlinear optics in composite materials” in Progress in optics XXIX, ed. by E. Wolf, Elsevier Science Publishers (1991) pp. 321. |
| **Harmon** | E. S. Harmon, M. R. Melloch, J. M. Woodall, D. D. Nolte, N. Otsuka, and C. L. Chang, Appl. Phys. Lett. **63**, 2248 (1993). |
| **Kaminska** | M. Kaminska, Z. Liliental-Weber, E. R. Weber, T. George, J. B. Kortright, F. W. Smith, B-Y. Tsaur, and A. R. Calawa, Appl. Phys. Lett. **54**, 1881 (1989). |
| **Kimoto** | K. Kimoto, Y. Kamiya, N. Nonoyama, and R. Uyeda, Jpn. J. Appl. Phys. **2**, 702 (1963). |
| **Look** | D. C. Look, D. C. Walters, G. D. Robinson, J. R. Sizelove, M. G. Mier, and C. E. Stutz, J. Appl. Phys. **74**, 306 (1993). |
| **Melloch** | M. R. Melloch, N. Otsuka, J. M. Woodall, A. C. Warren, and J. L. Freeouf, Appl. Phys. Lett. **57**, 1531 (1990). |

| | |
|---|---|
| **Melloch2** | M. R. Melloch, J. M. Woodall, E. S. Harmon, N. Otsuka, F. H. Pollak, D. D. Nolte, R. M. Feenstra, and M. A. Lutz, Annu. Rev. Mater. Sci. **25**, 547 (1995). |
| **Othonos** | A. Othonos, J. Appl. Phys. **83**, 1789 (1998). |
| **Papadogiannis** | N. A. Papadogiannis, B. Witzel, C. Kalpouzos, and D. Charalambidis, Phys. Rev. Lett. **83**, 4289 (1999). |
| **Perenboom** | J. A. A. J. Perenboom, P. Wyder and F. Meier, Physics Reports **78**, 173 (1981). |
| **Smith** | F. W. Smith, A. R. Calawa, C-L. Chen, M. J. Manfra, and L. J. Mahoney, IEEE Electron. Dev. Lett. **9**, 77 (1988). |
| **Smith2** | P. W. E. Smith, S. D. Benjamin and H. S. Loka, Appl. Phys. Lett. **71**, 1156 (1997). |
| **Shah** | J. Shah, Ultrafast Spectroscopy of Semiconductors and Semiconductor Nanostructures, Springer series in Solid-State Sciences **115**, Springer. |
| **Stookey** | S. D. Stookey, J. Amer. Ceram. Soc. **32**, 246 (1949). |
| **Turkevich** | J. Turkevich, P. C. Stevenson and J. Hillier, Discuss. Faraday Soc. **11**, 55 (1955). |
| **Voisin** | C. Voisin, D. Christofilos, N. Del Fatti, F. Vallee, B. Prevel, E. Cottancin, J. Lerme, M. Pellarin, and M. Broyer, Phys. Rev. Lett. **85**, 2200 (2000). |
| **Walukiewicz** | W. Walukiewicz, Z. Liliental-Weber, J. Jasinski, M. Almonte, A. Prasad, E. E. Haller, E. R. Weber, P. Grenier, and J. F. Whitaker, Appl. Phys. Lett. **69**, 2569 (1996). |

**Warren** A. C. Warren, N. Katzenellenbogen, D. Grischkowsky, J. M. Woodall, M. R. Melloch, and N. Otsuka, Appl. Phys. Lett. **58**, 1512 (1991).

**Warren2** A. C. Warren, J. M. Woodall, J. L. Freeouf, D. Grischkowsky, D. T. McInturff, M. R. Melloch, and N. Otsuka, Appl. Phys. Lett. **57**, 1331 (1990).

# Chapter 2 Experimental Details

## 2.1 Introduction

The study of ultrafast dynamic phenomena in condensed matter, where the characteristic time scale is of the order of a few ps or even shorter, requires the use of properly characterized ultrashort, pulsed sources. The newly developed all-solid-state laser systems have proven to be a valuable tool, in this recruit to study such ultra fast phenomena. [Lin, Othonos] In this chapter the details of the laser systems that are used for the experiments are presented followed by a description of the experimental setups, detailed beam characterization techniques and required modeling considerations necessary for the analysis of the detected signals.

## 2.2 Laser systems

For the purposes of this work, two types of lasers are employed.

### 2.2.1 The commercial laser system

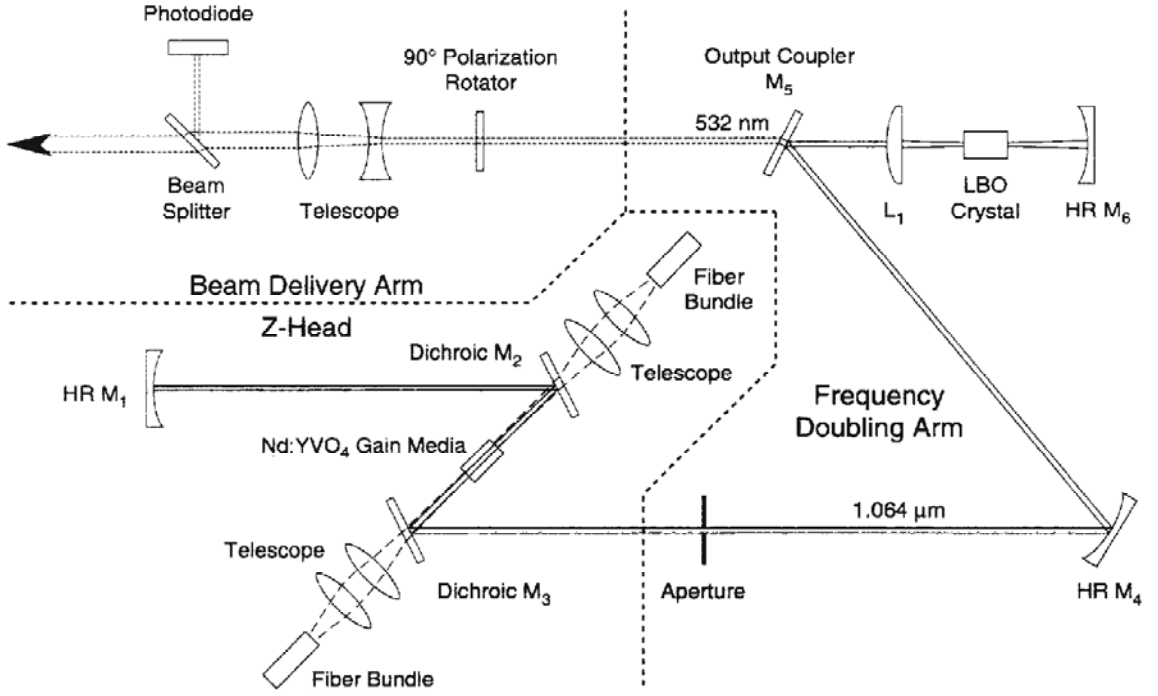

**Figure 2-1** The Millenia V laser system. A Nd:YVO$_4$ crystal is pumped by laser diodes. The resulting 1064 nm is frequency doubled to obtain the 532 nm output.

The laser system used for the experimental work presented in **Chap. 4** is a commercially available Spectra Physics system, comprising a Titanium (Ti) doped Sapphire (Sapph) laser (Tsunami model) pumped by a Spectra Physics Continuous Wave (CW) (Millennia V model). The Millennia V laser head is shown in **Fig. 2-1**. In the Millennia V, the high output power from laser diodes is used to end-pump the lasing medium, which is the Nd$^{3+}$ ions embedded in an Yttrium Vanadate crystalline matrix (Nd:YVO$_4$) host. The resulting 1064 nm output is converted to the visible through intracavity frequency doubling or second harmonic generation (SHG) in a nonlinear crystal. The Millennia V uses a 90 °, non-critically phase-matched, temperature-tuned lithium triborate (LBO) nonlinear crystal as its doubling medium.

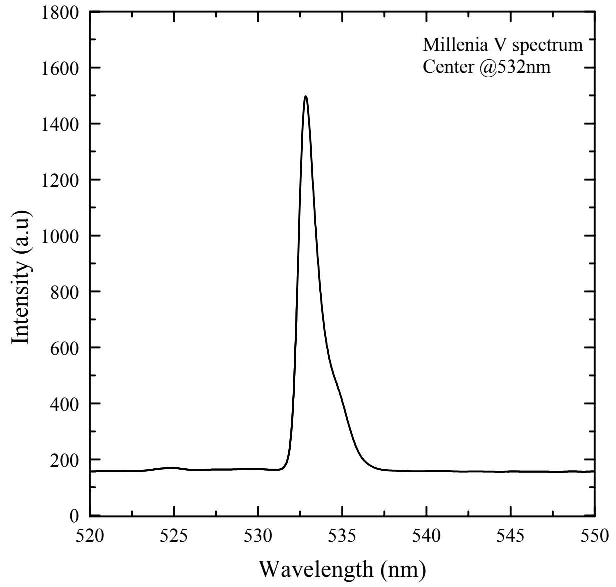

**Figure 2-2** The output beam of the Millenia V laser system as measured by a laboratory spectrometer. The wavelength is 532 nm and the FWHM is below resolution limit (~1 nm).

The resulting output wavelength is 532 nm (green); the spectrum is shown in **Fig. 2-2**. The maximum output CW power is 5.5 W, with a $TEM_{00}$ spatial mode. The beam diameter is 2 mm at $1/e^2$ points and the beam divergence is less than 0.5 mrad. The polarization is more than 100:1 vertical. The power stability is about 1% and the beam pointing stability is less than 5 μrad $^{o}C^{-1}$. The noise is less than 0.1 % rms. This green beam pumps the Tsunami system, shown in **Fig. 2-3**, which can provide pulses tunable from 660 nm up to 1150 nm depending on the installed cavity mirrors set. The repetition rate of the Tsunami is 81 MHz allowing measurements with high

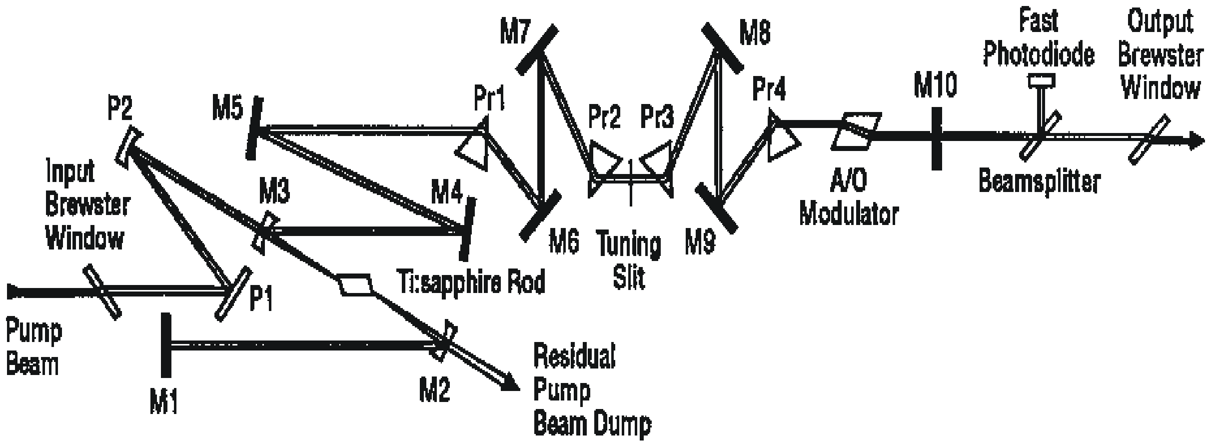

**Figure 2-3** The Tsunami laser system. A Ti:Sapphire rod is pumped by the 532 nm output of the Millenia V. The resulting 660 nm – 1150 nm radiation can oscillate in the cavity. The combination of the p-prisms and the tuning slit selects the wavelength value and width of the output ultrafast pulse.

repetition and stability. The pulse duration varies from 80 fs to 200 fs depending on the operating wavelength of the system. The maximum output power is close to 1 W and varies depending again on the wavelength. The spatial mode is elliptical as shown in **Fig. 2-4**.

### 2.2.2 The homemade laser system

The laser system used in the experiment presented in **Chap. 6** is shown in **Fig. 2-5**. It is a homemade Ti:Sapphire based solid-state laser. It is manufactured by the research personnel in the Laboratoire d'Optique Quantique, Ecole Polytechnique. [Langot] The Ti:Sapphire rod is pumped by a CW Argon-Ion laser operating at a wavelength of 514 nm. The power used to pump the Ti:sapphire crystal is of the order of 12 W. The repetition rate of the laser is 76 MHz and the pulse duration varies from 18 fs to 70 fs depending on the operation wavelength of the system.

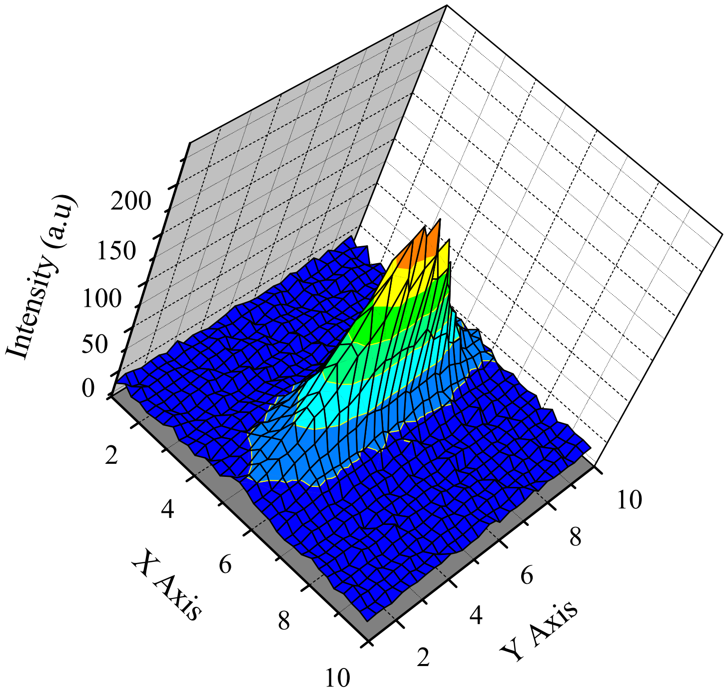

**Figure 2-4** The spatial mode of the Tsunami output beam. The beam is elongated on one dimension, resulting in slightly elliptical geometry.

The beam spatial profile is nearly circular with a diameter of approximately 3 mm and the maximum output power ranges from 1.3 W to 150 mW when operating in the 930 nm to 1070 nm region respectively.

## 2.3 Ultrafast pump and probe spectroscopy

All experimental setups presented in this work, are based on the classic pump probe configuration. A schematic representing the basics of this configuration is presented in **Fig. 2-6**. An intense beam at a specific wavelength pumps or excites the under study material. The moment that the pump beam illuminates the target is usually defined as time zero. The sample is in this way driven out of its equilibrium status. The pump beam is then dumped with the use of appropriate filtering. From time zero and on, the sample returns to its equilibrium status following a specific

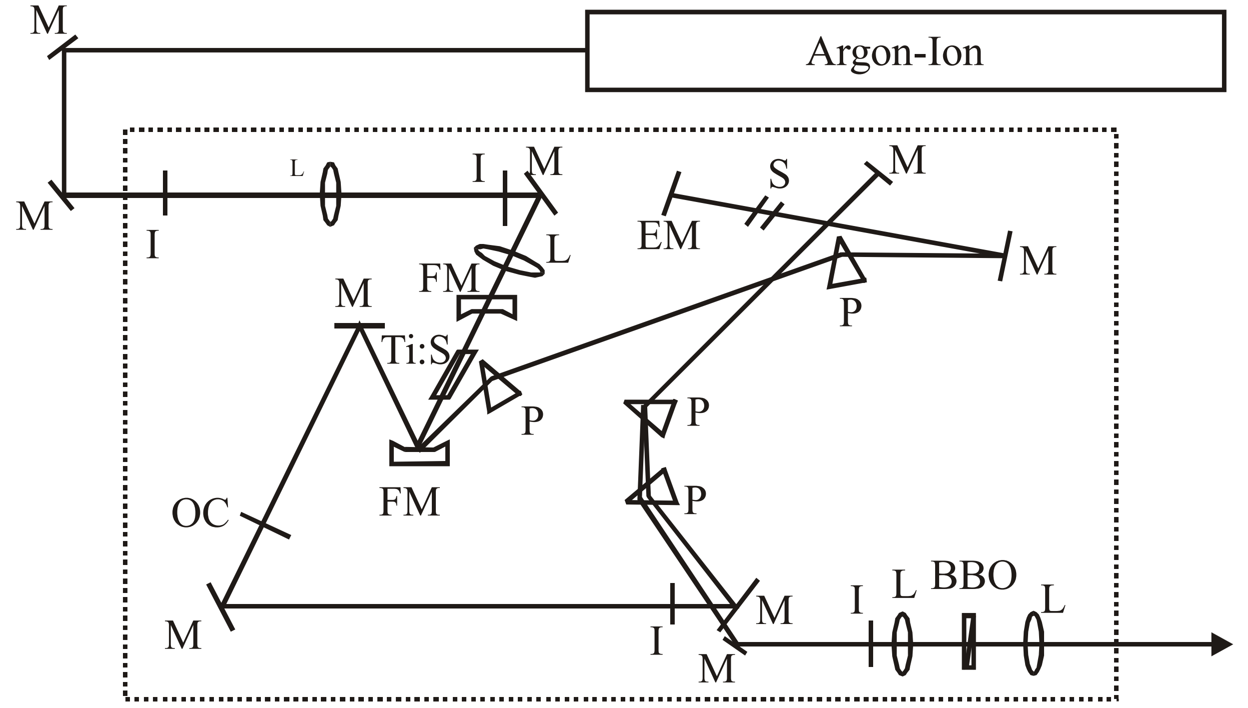

**Figure 2-5** The interior of the laser system built in Ecole Polytechnique. The principle is similar to the commercial Ti:Sapphire system, shown in **Fig. 2-3**.

function of time, *f(t)*. This function, *f(t)*, is in our case the problem to be solved. This is to be done with the use of a weak, time-delayed beam.

The probe beam is always kept much weaker than the pump beam so as not to perturb the sample. This statement is of course never true, but in a good approximation the perturbation caused by the weak beam can be assumed to be much weaker than the perturbation caused by the pump beam, especially if the effect of interest is non linearly dependent on the intensity of the excitation. The probe beam is modified when it arrives at the sample. The modification depends clearly on the delay $\tau$ of the probe beam with respect to time zero (or the "instant" of perturbation by the pump beam) because the behavior of the sample response function is time dependent. This modified probe beam is the only one that selectively passes through the appropriate filter and is collected and measured by the detector. To be more exact, it is the convolution of the cross correlation (CC) of the pump and probe beams with the response function of the material that is measured by the detector as will be shown later in the text. This way, it is a problem of mathematical analysis to de-

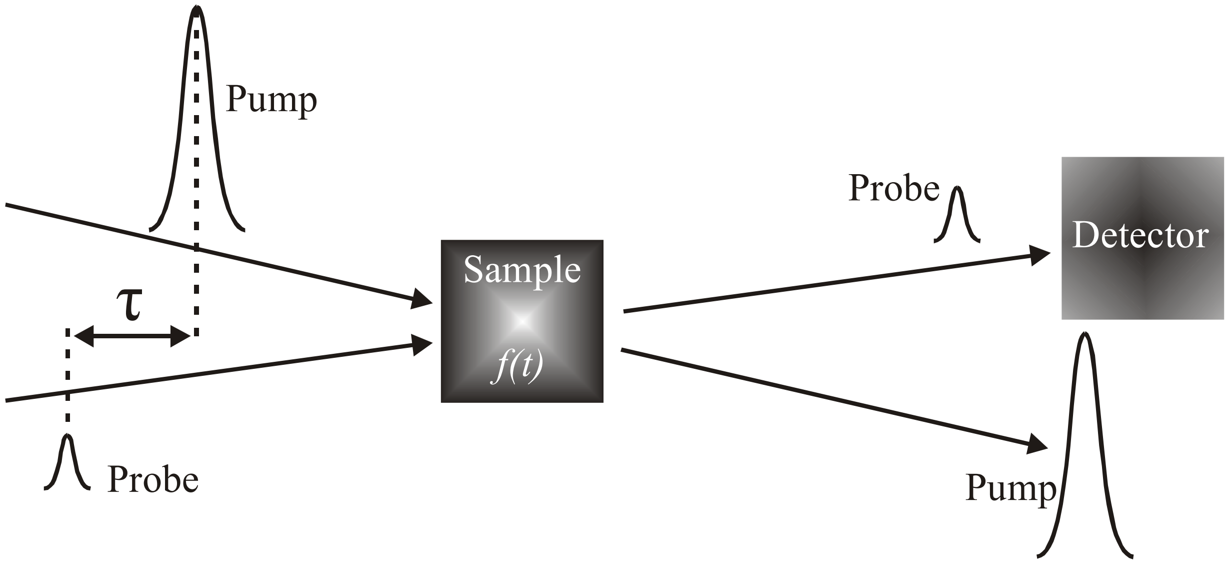

**Figure 2-6** The pump-probe principle. The pump beam excites the system at *t*=0. The system follows a function *f(t)* towards equilibrium. The probe beam convolves with *f(t)* and is selectively detected. With deconvolution of the signal, the function *f(t)* can be obtained.

convolute the detected signal function to its components and derive the characteristic time constants of the sample's response function.

A mathematical description of the detected signal is given below. We consider a simplified example of a three level system (**Fig. 2-7**) where we make the following assumptions:

- Level 1 is completely full with electrons. The analogue can be the valence band of a semiconductor like GaAs under no or small perturbation.

- Level 2 is initially completely empty of electrons. It can accept electrons that are somehow excited to this level. The analogue can be the conduction band of a semiconductor and the excitation can be a laser beam with low enough intensity so as to be considered as a small perturbation to the system.

- Level 3 is initially also completely empty of electrons. It can however, accept electrons that decay from level 2. The analogue can be for example the area that surrounds the initially excited area of the semiconductor where a high density of electrons is formed. Of course, electrons after excitation diffuse from this high density area

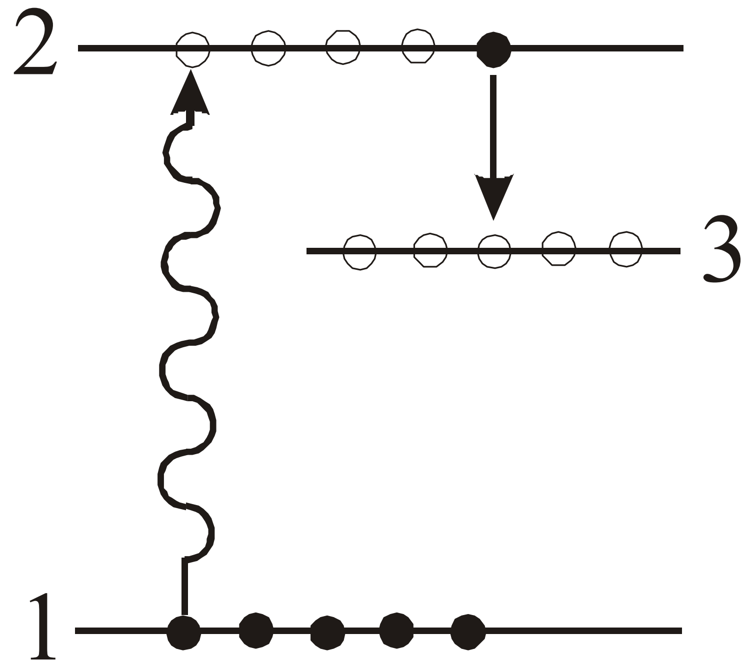

**Figure 2-7** A simplified three-level system to help in modeling the signal considerations.

towards the surroundings.

Let us first suppose that at time $t=0$, a population $n_0$ of electrons is by any means found at level 2. Then, the electron population $n(t)$ is going to decay towards level 3 with its population kinetics being described by:

$$\frac{dn(t)}{dt} = -\frac{n(t)}{\tau_e} \tag{2-1}$$

The solution of the last formula gives the time evolution of the electron population:

$$n(t) = n_0 e^{-\frac{t}{\tau_e}} \tag{2-2}$$

In the above, we do not take into account the means that the electron population $n_0$ is initially excited in level 2. Silently, we have assumed that the population is instantaneously found in level 2. However, this is never true. No matter how rapid an excitation can be, it will always have a finite duration. An analogue in real experimental life, is the finite duration of an exciting laser beam. If we suppose that the exciting (pump) beam intensity time profile is $I_p(t)$, then the electron population in level 2 takes the form: **Tang, Taylor**

$$n(t) \propto \int_{-\infty}^{t} I_p(t') e^{-\frac{t'-t}{\tau_e}} dt' \tag{2-3}$$

Of course, in the case that the laser intensity time profile is infinitely short, i.e. a $\delta$-function in time, the last formula readily reduces to **Eq. 2-2**. In the general case that we are interested in any quantity $F(t)$ that, when found away from equilibrium, freely decays with a function $f(t)$, then in the presence of a finite duration excitation:

$$F(t)=\int_{-\infty}^{t} I_p(t')f(t'-t)dt' \tag{2-4}$$

A change of variables $\tau = t' - t$ gives:

$$F(t)=\int_{-\infty}^{0} I_p(t+\tau)f(\tau)d\tau$$

Usually, in typical pump-probe experiments, one uses a second, time-delayed probe beam *$I_{probe}(t)$*, in order to probe the changes that are induced to the perturbed system by the pump (exciting) beam. The changes are monitored by a detector that records the change in the transmitted (or reflected) intensity of the probe beam. The recorded signal is then the convolution of the probe beam intensity time profile with the quantity *F(t)*: **Tang**

$$Signal(t)=\int_{-\infty}^{+\infty} F(t')I_{probe}(t'-t)dt' \tag{2-5}$$

By substitution of *F(t)* we can get:

$$Signal(t)=\int_{-\infty}^{+\infty} dt' I_{probe}(t'-t)\left[\int_{-\infty}^{0} d\tau I_{pump}(t'+\tau)f(\tau)\right] \Rightarrow$$

$$Signal(t)=\int_{-\infty}^{0} d\tau f(\tau)\left[\int_{-\infty}^{+\infty} dt' I_{probe}(t'-t)I_{pump}(t'+\tau)\right] \tag{2-6}$$

A change of variables $t+\tau=\vartheta$ then gives:

$$Signal(t)=\int_{-\infty}^{0} d\tau f(\tau)\left[\int_{-\infty}^{+\infty} d\theta I_{probe}(\vartheta-\tau-t)I_{pump}(\vartheta)\right]$$

Now, the inner integral is equal to the cross correlation (CC) function of the pump and probe pulses as already shown in a previous paragraph and so, the signal function becomes:

$$Signal(t) = \int_{-\infty}^{0} d\tau f(\tau) CC(\tau + t) \Rightarrow$$

$$Signal(t) = \int_{-\infty}^{+\infty} d\tau \Theta(\tau) f(\tau) CC(\tau + t) \qquad (2\text{-}6)$$

where *Θ(t)* is the Heaviside step function and *CC(t)* is the cross correlation function.

In a real pump probe experiment, usually the function *Signal(t)* is denoted as $\frac{\Delta T}{T}$ which is the transient differential transmission of the system and the function *f(t)* is an exponential decay function either single- or multi-exponential. In this case, one assumes a certain *f(t)* function and reproduces the signal function through numerical calculations. By the best fit of the experimental results, the user is able to determine the function *f(t)* which is the point of interest.

For example, let us consider the case of an intrinsic semiconductor like GaAs. The unterturbed absorption of the system is α and it corresponds to the function *f(t)* in the above description. If the pump pulse is small enough to be considered a perturbation, then it induces a change:

$$\Delta\alpha = (1 - f_e - f_h)\alpha \qquad (2\text{-}7)$$

where $f_e$ and $f_h$ are the distribution functions of free electrons and holes respectively. In this case, the change in the transmission of the probe beam can be written as: **Shah**

$$\frac{\Delta T}{T}(\tau) = \frac{T(\tau) - T_0}{T_0} = -\Delta\alpha(\tau) d \qquad (2\text{-}8)$$

where *d* is the sample's thickness. It this case, as shown by **Eq. 2-5**, or **Eq. 2-6**, the measured signal would be the convolution of the time dependent $\frac{\Delta T}{T}$ with the CC of the pump and probe pulses.

## 2.4 The lock-in detection

A lock-in amplifier is usually used to collect the signal of the detector (in our case the photo multiplier) and a PC to record it. The Lock-in amplifier used, is a commercially available Stanford Research Instruments SR810 model. In general, lock-in amplifiers are used to detect and measure very small AC signals, all the way down to a few nanovolts. The technique used by a lock-in amplifier is known as phase-sensitive detection (PSD) and it is used to single out the component of the signal at a specific reference frequency and phase. Signal frequency components other than the reference frequency are considered noise contributions and are rejected by the lock-in. The reference frequency used to trigger the lock-in amplifier is given by the chopper that modulates the pump beam at a typical frequency of 1 kHz.

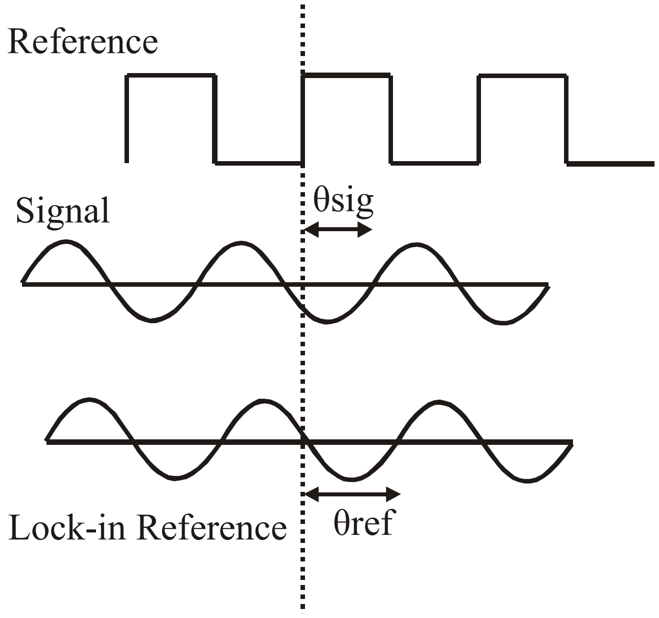

**Figure 2-8** The Lock-in principle.

Lock-in measurements require a frequency reference. Typically an experiment is excited at a fixed frequency (from an oscillator or function generator) and the lock-in detects the response from the experiment at the reference frequency. In **Fig. 2-8** the reference signal is a square wave at frequency $\omega_r$. This might be the sync output from a function generator. If the sine output from the function generator is used to excite the experiment, the response might be the signal waveform shown in **Fig. 2-8**. The signal is

$$V_{sig}\sin\left(\omega_r t+\theta_{sig}\right) \tag{2-9}$$

where $V_{sig}$ is the signal amplitude. The lock-in amplifier generates its own sine wave, shown as the lock-in reference in **Fig. 2-8**. The lock-in reference is

$$V_L\sin\left(\omega_L t+\theta_{ref}\right) \tag{2-10}$$

The lock-in amplifier amplifies the signal and then multiplies it by the lock-in reference using a phase sensitive detector or multiplier. The output of the PSD is the product of two sine waves:

$$\begin{aligned} V_{psd} &= V_{sig}V_L\sin\left(\omega_r t+\theta_{sig}\right)\sin\left(\omega_L t+\theta_{ref}\right) \\ &= \frac{1}{2}V_{sig}V_L\cos\left[\left(\omega_r-\omega_L\right)t+\theta_{sig}-\theta_{ref}\right] \\ &- \frac{1}{2}V_{sig}V_L\cos\left[\left(\omega_r+\omega_L\right)t+\theta_{sig}+\theta_{ref}\right] \end{aligned} \tag{2-11}$$

The PSD output consists of two AC signals, one at the difference frequency $\omega_r-\omega_L$ and the other at the sum frequency $\omega_r+\omega_L$. If the PSD output is passed through a low pass filter, the AC signals are removed. In the general case, nothing will be left. However, if $\omega_r$ equals $\omega_L$, the difference frequency component will be a DC signal. In this case, the filtered PSD output will be:

$$V_{psd}=\frac{1}{2}V_{sig}V_L\cos\left(\theta_{sig}-\theta_{ref}\right) \tag{2-12}$$

This is a nice DC signal proportional to the signal amplitude.

Now suppose the input is made up of signal plus noise. The PSD and low pass filter only detect signals whose frequencies are very close to the lock-in reference frequency. Noise signals at frequencies far from the reference are attenuated at the PSD output by the low pass filter (neither $\omega_{noise} - \omega_{ref}$ nor $\omega_{noise} + \omega_{ref}$ are close to DC). Noise at frequencies very close to the reference frequency will result in very low frequency AC outputs from the PSD ($\left|\omega_{noise} - \omega_{ref}\right|$ is small). Their attenuation depends upon the low pass filter bandwidth and roll-off. A narrower bandwidth will remove noise sources very close to the reference frequency; a wider bandwidth determines the bandwidth of detection. Only the signal at the reference frequency will result in a true DC output and be unaffected by the low pass filter. This is the signal we want to measure.

We need to make the lock-in reference the same as the signal frequency, i.e. $\omega_r = \omega_L$. Not only do the frequencies have to be the same, the phase between the signals cannot change with time, otherwise $\cos(\theta_{sig} - \theta_{ref})$ will change and $V_{psd}$ will not be a DC signal. In other words, the lock-in reference needs to be phase-locked to the signal reference.

Lock-in amplifiers use a phase-locked-loop (PLL) to generate the reference signal. An external reference signal (in this case, the reference square wave) is provided to the lock-in. The PLL in the lock-in locks the internal reference oscillator to this external reference, resulting in a reference sine wave at $\omega_r$ with a fixed phase shift of $\theta_{ref}$. Since the PLL actively tracks the external reference, changes in the external reference frequency do not affect the measurement.

## 2.5 Experimental arrangement

### 2.5.1 Detection principle

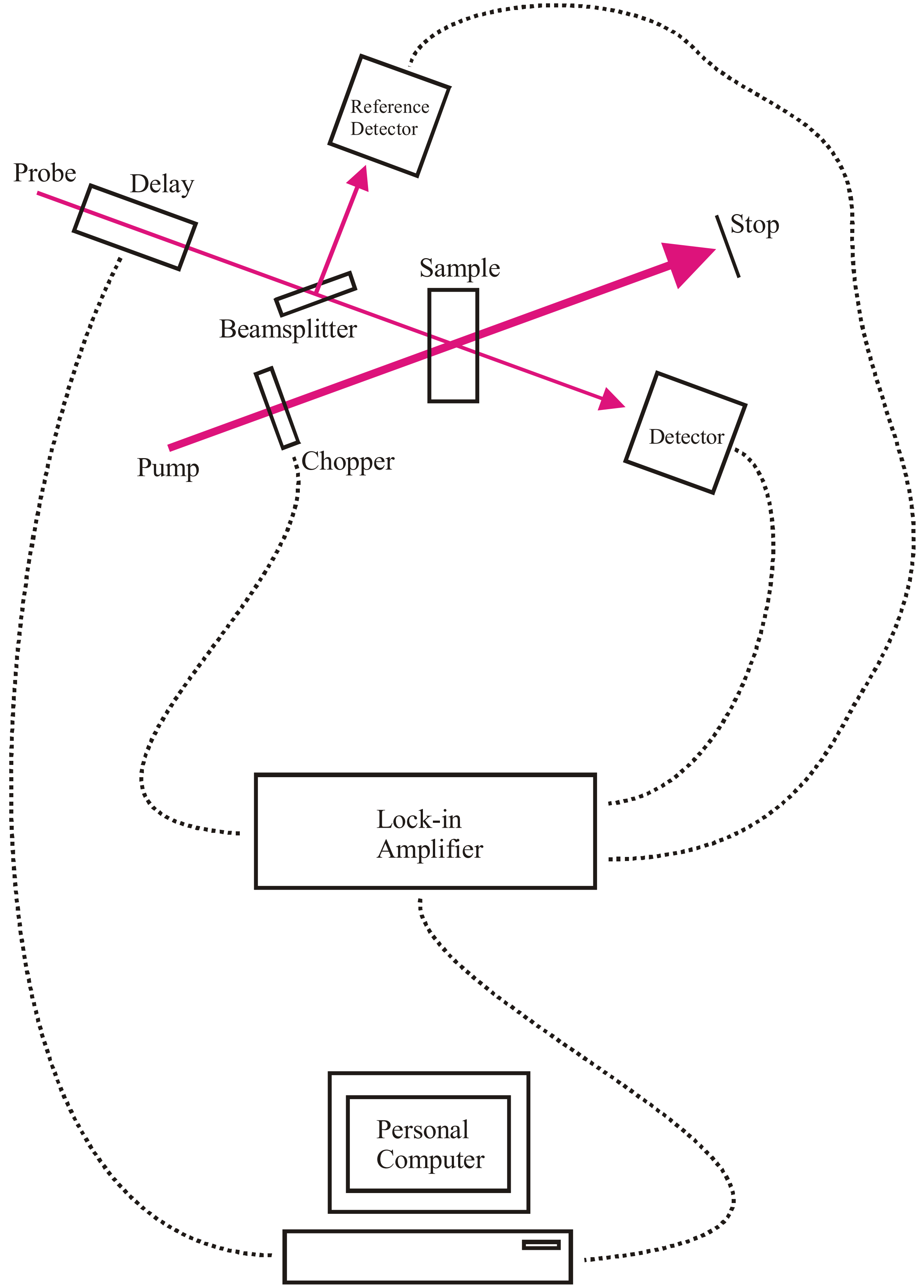

**Figure 2-9** The detection schematic of pump-probe measurements showing the main instruments used in the experiments.

A presentation of the detection schematic is drawn in **Fig. 2-9**. The probe beam passes through a variable delay line, which is controlled by a Personal Computer (PC). A chopper, whose reference frequency signal is sent to a Lock-in Amplifier, modulates the pump beam. The pump and

probe beams cross the sample and while the pump beam is dumped, the probe beam is measured by a detector whose signal is guided to the PC. The output of the Lock-in Amplifier is also guided to the PC where it is monitored and recorded. An optional path involving the reference detector is used in **Chap. 6**: a small portion of the probe beam is obtained from the reflection of a beam splitter and is collected by a reference detector. The signal of this detector is guided to the Lock-in Amplifier and subtracted from the signal of the detector.

### 2.5.2 Degenerate pump-probe setup

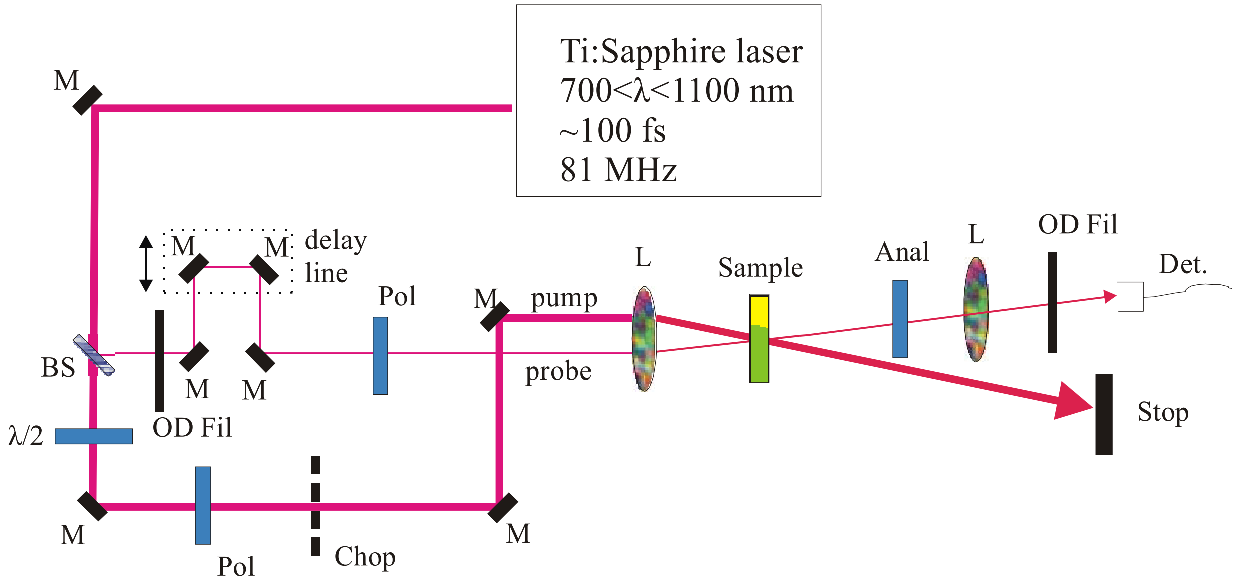

**Figure 2-10** The experimental setup used in the LTG-GaAs and LTG-AlGaAs experiments (**Chap. 4**). The laser beam is splitted in two parts which are focused on the sample with controlable time delays and perpendicular polarizations. The probe beam is selectively collected and detected and its transmission changes are monitored as a function of the time delay with the pump beam.

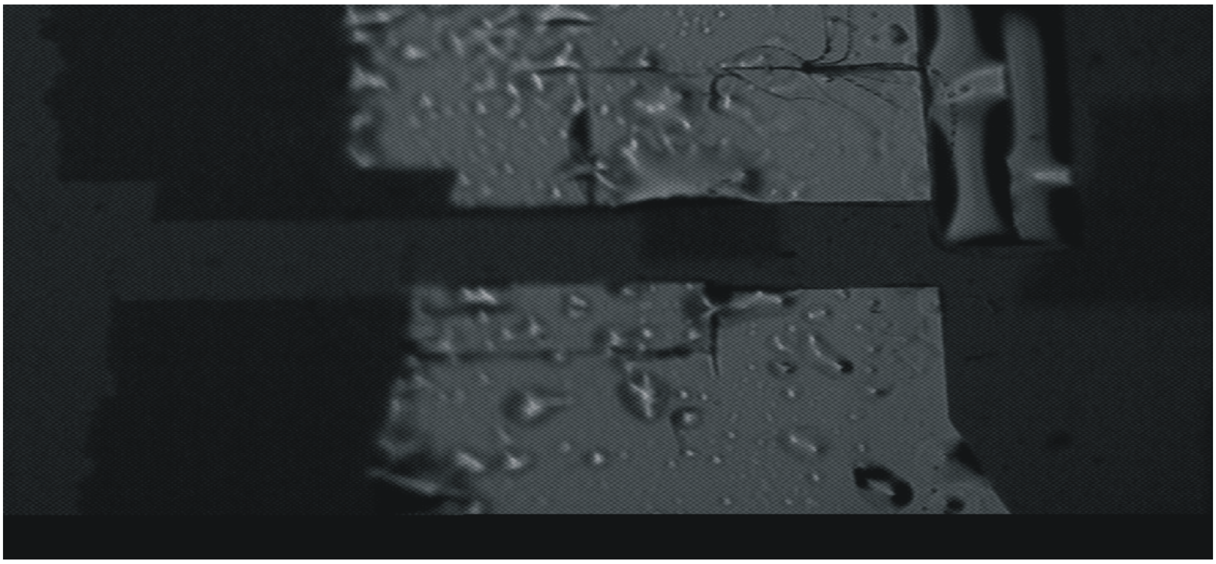

**Figure 2-11** A typical sample area as monitored by a CCD camera. Such monitoring is crucial because as is obvious, the sample may be full of macroscopic defects (i.e. cracks and various anomalies). The pumping and probing in a smooth sample area is this way achieved.

The experimental setup used in **Chap. 4**, is shown in **Fig. 2-10**. It is based on a Mach-Zender interferometer. The laser beam is initially divided in two parts by means of a 90:10 beam splitter. The polarization status of the beams remains unchanged before and after the beam splitter. The transmitted beam, referred to as the pump beam, is always more intense than the reflected beam, referred to as the probe beam. The probe beam is delayed with respect to the pump using a variable delay stepper motor. The stepper motor (available by Microcontrole) has an optimum resolution of 100 nm or equivalently 0.667 fs ($\Delta s = v\Delta t$) and is driven by a PC. The maximum travel of the stepper motor is about 3 cm or equivalently about 200 ps roundtrip delay for the beam. The continuous wave (CW) power of the probe is controlled using a neutral variable density filter. Because of the small beam dimensions it is assumed that the spatial intensity gradient caused by the attenuation is negligible. The polarization of the probe beam is always kept perpendicular with respect to that of the pump beam with the use of a Glan-Thomson polarizer. The Glan-Thompson polarizers (available by CVI, Model CPAS-10.0-670-1064) that are used have an extinction ratio of 100,000:1 in the crossed configuration. The pump beam first passes through a $\frac{\lambda}{2}$ wave plate and

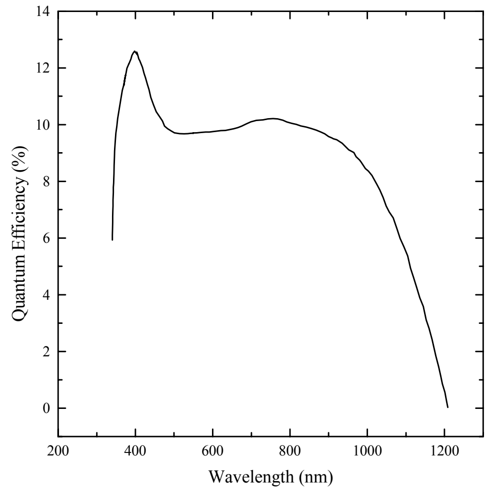

**Figure 2-12** The spectral response of the used photomultiplier.

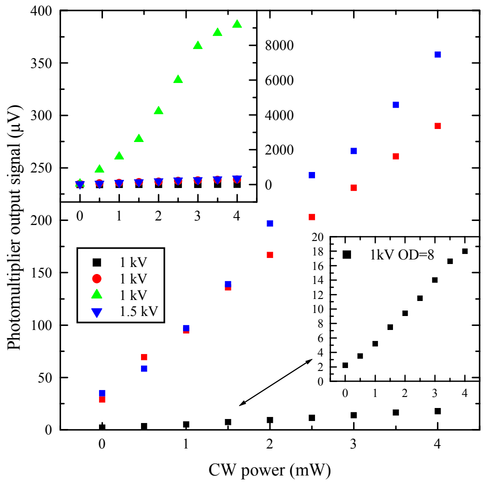

**Figure 2-13** The signal resonse of the used photomultiplier depends linearly on the incident light intensity.

then through a Glan-Thomson polarizer. With this combination of the two wave plates, control is established for the CW power of the beam by rotation of the $\frac{\lambda}{2}$ wave plate, while keeping the polarization of the beam always horizontal after the Glan-Thomson polarizer. This polarization state is chosen in order to minimize possible coherent artifacts caused through the interference of the pump and probe beams on the sample. The pump beam is modulated by a chopper, which is operating at typical frequencies near 1 kHz. The two beams exit the interferometer parallel to each other. The CW power of the two beams is measured with a CW power meter at the exit of the interferometer. The power meter has a resolution of smaller than 1 mW and is wavelength insensitive. The two beams are focused and spatially overlapped on the sample. The dimension of the two beams on the focus is measured using a CCD (Charge Coupling Device) camera with a magnification of 500 to be 50 µm in diameter. The CCD camera is also used in order to ensure the illumination of a smooth, defect-free sample area. A picture of such a sample area is shown in **Fig. 2-11**.

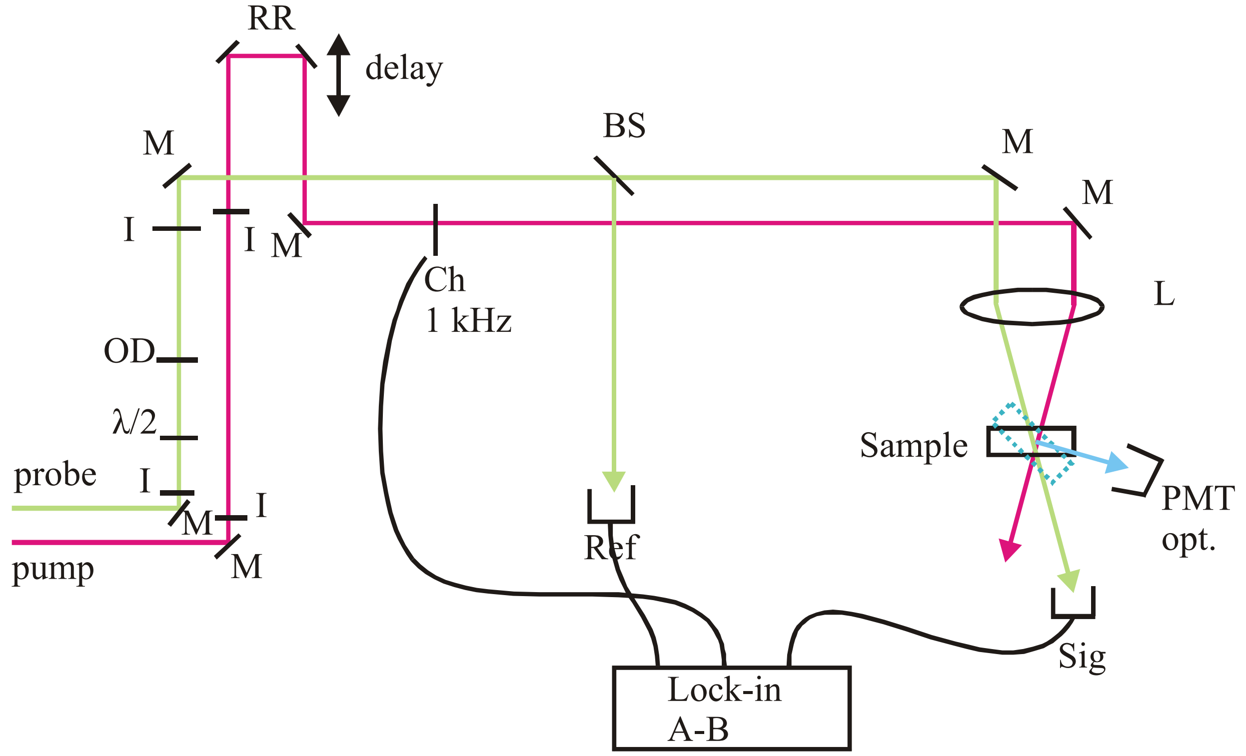

**Figure 2-14** The experimental setup used in the Au nanoparticle experiments (**Chap. 6**). The two colors comprise the two branches of the interferometer. A small portion of the green (probe) beam is used as the reference beam. Optionally, a BBO crystal can be placed instead of the sample in order to obtain CC measurements with the same experimental conditions as the transient absorption measurements.

Another Glan-Thomson polarizer, referred to as analyzer, is used with its optical axis parallel to the probe beam in order to dumb any possible transmission of the pump beam (i.e. due to scattering by macroscopic sample defects, cracks etc.) and to ensure that the only light detected comes from the probe beam. A photomultiplier monitors the transmitted probe beam. The photomultiplier used is a commercially available Hamamatsu R5108 model. Its spectral response ranges from 300 nm up to 1200 nm as shown in **Fig. 2-12**. A set of neutral density filters and a variable neutral density filter are used in order to bring the signal level of the photomultiplier to its linear response region and to ensure that the signal given by the photomultiplier is at the same level for every sample. Measurements of the linear response of the photomultiplier are shown in **Fig. 2-13**.

### 2.5.3 Non-degenarate pump-probe setup

The experimental setup used in **Chap. 6** is shown in **Fig. 2-14**. The configuration is similar to the one used in **Chap. 4**. The initial infrared beam is frequency doubled. The two colors are separated using a set of two prisms. One of the two colors, being more intense than the other, is used as the pump beam; the other is to be referred to as the probe beam. The probe beam passes through a $\frac{\lambda}{2}$ wave plate in order to control its polarization. A neutral density filter set is used to attenuate its CW power. A small portion of the probe beam is sent to a reference photodiode to measure the reference signal. The pump beam passes through a set of mirrors based on a variable delay stepper motor. A chopper, operating at a typical frequency of 1.5 kHz modulates the pump beam. The two beams are focused and are spatially overlapped onto the sample. The transmitted probe beam is then collected on the signal photodiode, which is masked by a band pass filter selected to allow only the probe wavelength to pass, in order to avoid any contribution coming from the pump beam. An optional additional path of the setup is used in order to measure the CC of the pump and probe beams using a Barium Borate Oxide (BBO) crystal at the position of the sample and a photomultiplier as a detector.

## 2.6 Laser parameter characterization: spectrum and pulse duration

The following deals with the characterization of the laser beams that are used in the means of spectra and pulse durations. It is essential for the beam to be well characterized because many measurements performed in this thesis are taken under various operating wavelengths and pulse

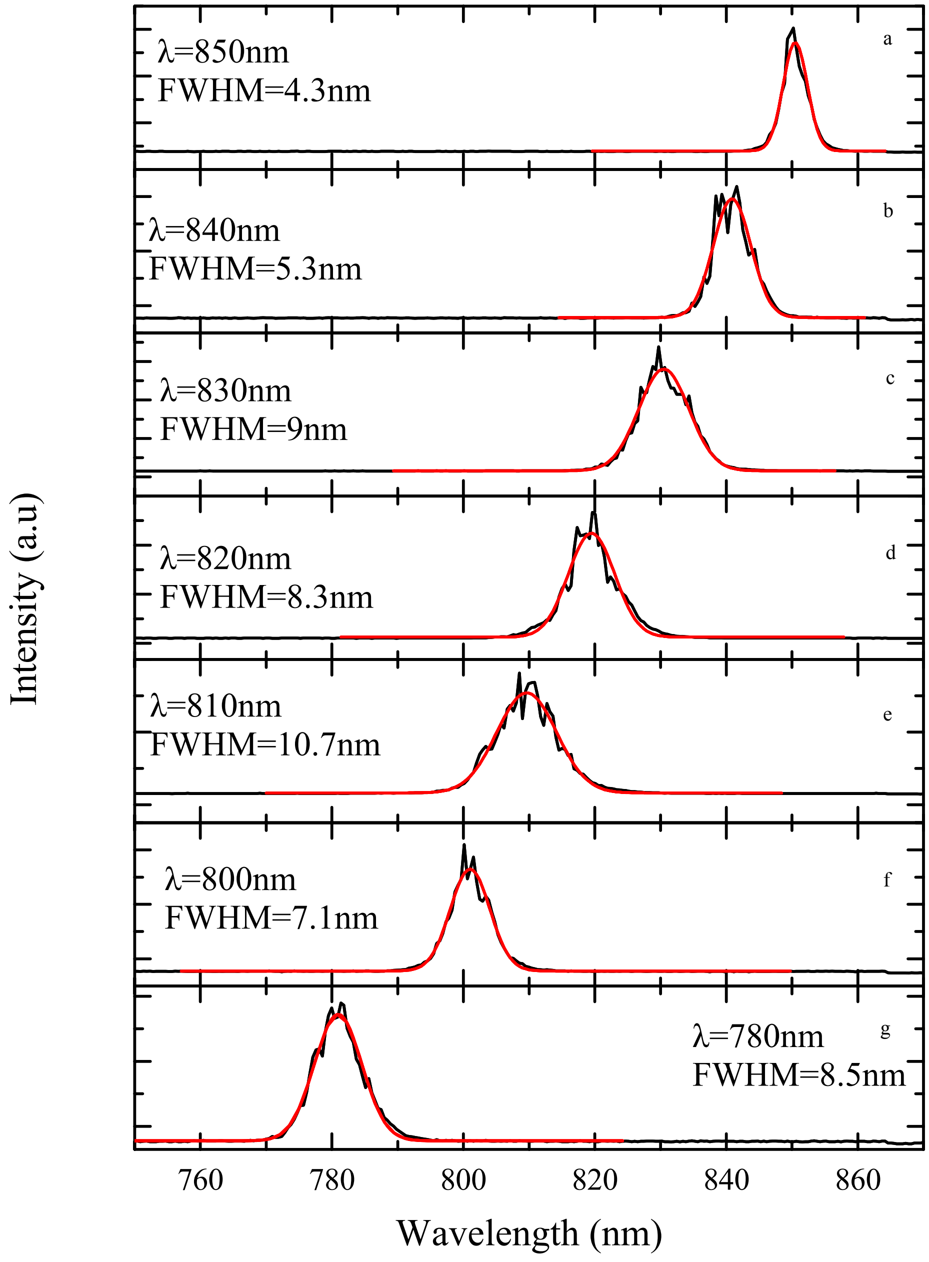

**Figure 2-15** Typical laser pulse spectra obtained with a laboratory spectrometer.

durations, values that are crucial in the experiments presented in the next chapters. The characterization methods are going to be presented for the characterization of only the Tsunami laser system, since the methods are quite similar for the homemade system as well.

The spectrum profile of the laser system used in **Chap. 4** is monitored using an Ocean Optics Model SD-1000 spectrometer. The range of the spectrometer spans the 300 nm - 870 nm region

with a resolution of a few nanometers. In **Figs. 2-15a** to **2-15g**, typical spectra of the Tsunami laser at various wavelengths from 780 nm to 850 nm are given.

All spectra are fitted with a Gaussian function of the form:

$$y = y_0 + Ae^{-\frac{(x-x_c)^2}{2w^2}} \tag{2-13}$$

where $y_0$, $A$, $x_c$ and $w$ are parameters to be calculated by the fitting procedure. The *FWHM* ($\Delta\lambda$) of the above function can be calculated to be:

$$FWHM = \Delta\lambda = 2\sqrt{2\ln 2}\,w \tag{2-14}$$

The fitting function can reproduce well all the experimental data. The computed $\Delta\lambda$ for the various laser spectra are shown in **Tab. 2-1**, as well as the calculated $|\Delta\nu| = c\frac{\Delta\lambda}{\lambda^2}$.

For the characterization of the laser pulse time profile and the measurement of its pulse

| **λ (nm)** | **Δλ (nm)** | **Δν (¥$10^{12}$ $s^{-1}$)** |
|---|---|---|
| | | |
| 780 | 8.5 | 4.2 |
| 800 | 7.1 | 3.3 |
| 810 | 10.7 | 4.9 |
| 820 | 8.3 | 3.7 |
| 830 | 9 | 3.9 |
| 840 | 5.3 | 2.3 |
| 850 | 4.3 | 1.8 |

**Table 2-1** The maximum spectral width that is achieved at the corresponding wavelengths.

duration, an autocorrelation technique is used. Two replicas of the laser beam are cross-focused on a BBO crystal. Under proper phase matching conditions (i.e. incidence angle of the beams and orientation of the crystal's optical axis) the second harmonic beam is produced which propagates at the bisector of the first two and has the double frequency of theirs. Measuring the intensity of this second harmonic radiation with respect to the time delay between the pump and the probe beams, the time profile of the laser pulse can be deduced. The above technique namely the autocorrelation technique is widely used with many variations in order to characterize ultra short pulses. **Papadogiannis, Sala**

For the realization of these measurements, the sample under investigation is simply replaced by a frequency doubling BBO crystal, as shown in **Fig. 2-10**. Using an interference filter in front of the photomultiplier allows the selective collection of the second harmonic light produced by the background free CC of the pump and probe pulses. An analysis based on the mathematical description of the CC of the two beams follows.

Assume that the pump and probe pulse intensities are described by:

$$\begin{aligned} Pump(t) &= Ae^{-\frac{t^2}{T_A{}^2}} \\ Probe(t) &= Be^{-\frac{t^2}{T_B{}^2}} \end{aligned} \tag{2-15}$$

where for the sake of generality different characteristic time constants $T_A$ and $T_B$ have been used to take into account the possibility that the pump and probe beams have a different wavelength and thus, in general, a different time profile, like in the experiments of **Chap. 6**.

The background free autocorrelation or CC of these two pulses is given by: **Sala**

$$CC(t) = \int_{-\infty}^{+\infty} Pump(t')Probe(t-t')dt' = AB\int_{-\infty}^{+\infty} e^{-\frac{T_B^{\,2}t'^2 + T_A^{\,2}(t-t')^2}{T_A^{\,2}T_B^{\,2}}}\,dt' \qquad \text{(2-16)}$$

Forming perfect squares at the power, the last integral becomes:

$$CC(t) = ABe^{-\frac{1}{T_A^{\,2}+T_B^{\,2}}t^2}\int_{-\infty}^{+\infty} e^{-\frac{\left(\sqrt{T_A^{\,2}+T_B^{\,2}}\,t' - \frac{T_A^{\,2}}{\sqrt{T_A^{\,2}+T_B^{\,2}}}t\right)^2}{T_A^{\,2}T_B^{\,2}}}\,dt'$$

which with a change of variables $\frac{\left(\sqrt{T_A^{\,2}+T_B^{\,2}}\,t' - \frac{T_A^{\,2}}{\sqrt{T_A^{\,2}+T_B^{\,2}}}t\right)^2}{T_A^{\,2}T_B^{\,2}} = \tau^2$, becomes:

$$CC(t) = AB\frac{T_AT_B}{\sqrt{T_A^{\,2}+T_B^{\,2}}}e^{-\frac{1}{T_A^{\,2}+T_B^{\,2}}t^2}\int_{-\infty}^{+\infty} e^{-\tau^2}d\tau$$

Since $\int_{-\infty}^{+\infty} e^{-\tau^2}d\tau = \sqrt{\pi}$, the last reduces to:

$$CC(t) = \sqrt{\pi}AB\frac{T_AT_B}{\sqrt{T_A^{\,2}+T_B^{\,2}}}e^{-\frac{1}{T_A^{\,2}+T_B^{\,2}}t^2} \qquad \text{(2-17)}$$

Here, note that the CC of the pump and probe pulses is also Gaussian in shape with the assumption that the intensities of the pump and probe pulses follow a Gaussian time profile. Moreover, the characteristic time constants $T_A$ and $T_B$ can be assumed to be equal in the special case where, (i) the pump and probe beams are replicas of the same laser beam and, (ii) the total optical densities that each of the two beams passes through is equal or in the same order of magnitude and small enough so it can be assumed in a very good approximation that the pulses remain undistorted and unaffected by possible nonlinear dispersion effects. It should also be noticed that the CC is always measured at the position of the sample with exactly the same experimental conditions as in

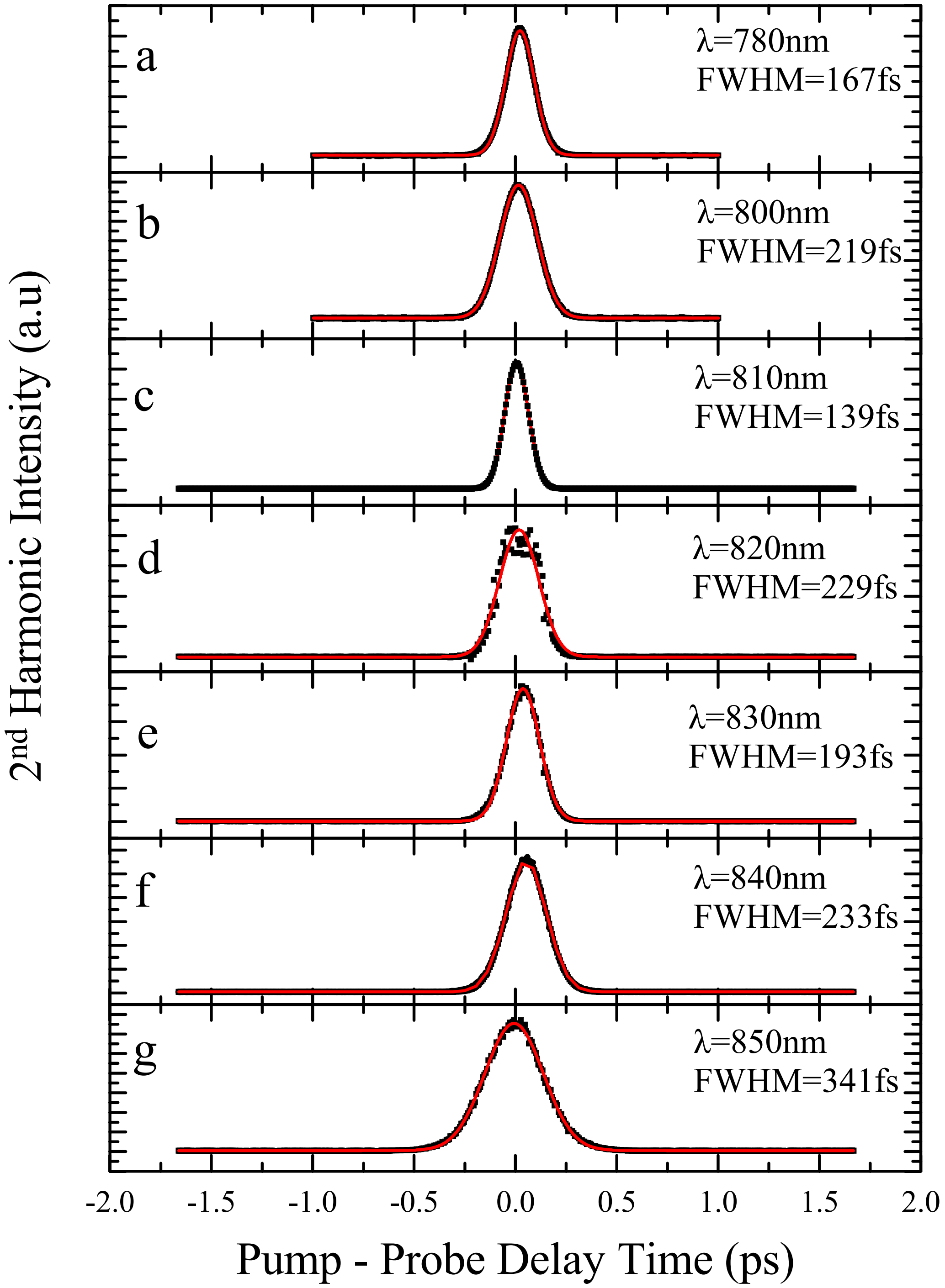

**Figure 2-16** CC measurements of the laser system at various wavelengths.

the case of the semiconductor or nanocomposite measurements. Typical CC measurements are shown in **Fig. 2-16**. The CC are shown at various wavelengths from 780 nm up to 850 nm.

The data points are fitted with a Gaussian function of the form of **Eq. 2-13**:

$$y(x) = y_0 + Ae^{-\frac{(x-x_0)^2}{2w^2}}$$

where the parameters $y_0$, $A$, $x_c$ and $w$ are to be computed by the fitting procedure.

The fitting results for the *FWHM* of the CC at various wavelengths are shown at the second column of **Tab. 2-2**. Now, recalling that (**Eq. 2-15** and **Eq. 2-17**):

$$CC(t) \propto e^{-\frac{t^2}{T^2}} \text{ and } P_A \propto P_B \propto e^{-\frac{t^2}{T^2}}$$

and that the FWHM of the CC(t) should be:

$$\tau_G{}^2 = FWHM^2 = 8(\ln 2)T^2 \Rightarrow \tau_G = 2\sqrt{\ln 2}T \qquad (2\text{-}18)$$

and equivalently the pulse duration (*FWHM* of $P_A$ or $P_B$) should be:

$$\tau_p{}^2 = 8\ln 2\left(\frac{T^2}{2}\right) \Rightarrow \tau_p = 2\sqrt{\ln 2}T \qquad (2\text{-}19)$$

| **λ (nm)** | **FWHM (fs) $\tau_G$** | **$\tau_p$ (fs)** | **$\Delta\nu\ \tau_p$** |
|---|---|---|---|
| | | | |
| 780 | 167 | 118 | 0.49 |
| 800 | 219 | 155 | 0.51 |
| 810 | 139 | 98 | 0.48 |
| 830 | 193 | 136 | 0.53 |
| 840 | 233 | 165 | 0.38 |
| 850 | 200 | 141 | 0.25 |

**Table 2-2** The cross-correlation FWHM and the pulse duration at various wavelengths.

it is straightforward that

$$\tau_p = \frac{\tau_G}{\sqrt{2}} \tag{2-20}$$

The computed pulse durations are shown at the third column of **Tab. 2-2**. Shown also is the product $\Delta\nu\tau_p$, which for Fourier limited pulses should be equal to 0.44. [Sala]

## 2.7 Transmission Electron Microscopy

The technique of the Transmission Electron Microscopy (TEM) is used in order to characterize the structure of systems with dimensions down to a few nanometers in size. The principle of the technique is shown in **Fig. 2-17**. A directional electron beam is directed on the sample. The electron beam comes from the top of **Fig. 2-17**. Electrons are subject to scattering when diffusing through the sample. At the bottom of the sample a photographic film is placed and records the electrons that

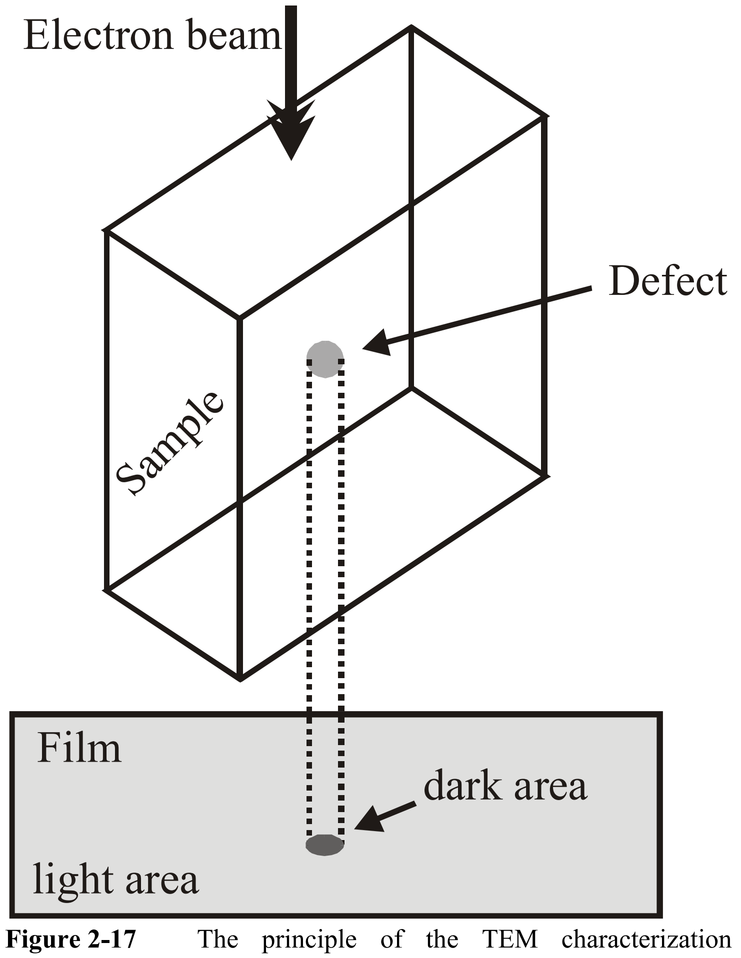

**Figure 2-17** The principle of the TEM characterization technique.

managed to penetrate the sample. In that sense, white areas of the film are interpreted as maximum transmittance of the electron beam while dark areas on the film are interpreted as increased scattering of the beam electrons to various defects of the sample. Through analysis of the photographs, the density, size and shape of the defects can be obtained.

## 2.8 References

**Langot** P. Langot, N. Del Fatti, R. Tommasi and F. Vallee, Opt. Commun. **137**, 285 (1997).

**Lin** W. Z. Lin, L. G. Fujimoto and E. P. Ippen, Appl. Phys. Lett. **50**, 124 (1987).

**Othonos** A. Othonos, J. Appl. Phys. **83**, 1789 (1998).

**Papadogiannis** N. A. Papadogiannis, S. D. Moustaizis, P. A. Loukakos and C. Kalpouzos, Appl. Phys. B **65**, 339 (1997).

**Sala** K. L. Sala, G. A. Kenney-Wallace and G. E. Hall, IEEE J. Quant. Electron. **QE-16**, 990 (1980).

**Shah** J. Shah, Ultrafast Spectroscopy of Semiconductors and Semiconductor Nanostructures, Springer series in Solid-State Sciences **115**, Springer.

**Tang** C. L. Tang and D. J. Erskine, Phys. Rev. Lett. **51**, 840 (1983).

**Taylor** A. J. Taylor, D. J. Erskine and C. L. Tang, Appl. Phys. Lett. **43**, 989 (1983).

# Chapter 3 III-V Semiconductors: Background

## 3.1 Introduction

In this chapter, theoretical considerations are presented regarding the properties of the materials examined in **Chap. 4**, as well as the ultrafast relaxation mechanisms that govern the electronic behavior of the system after the excitation by an ultrafast laser pulse.

The layout of this chapter consists of a theoretical overview of the quantum structure of stoichiometric and nonstoichiometric GaAs and AlGaAs, their optical properties and concludes with the physical procedures that follow their excitation.

## 3.2 Structure

### 3.2.1 Stoichiometric GaAs

GaAs is a compound III-V semiconductor since Gallium (Ga) belongs to column III of the periodic table and As is a column V element. GaAs can form a crystalline structure in the zincblende form with a density of $2.2\times10^{22}$ molecules/cm$^3$. Ga occupies sites on one of the two interpenetrating fcc sublattices; As populates the other fcc sublattice as shown in **Fig. 3-1**. The lattice constant of crystalline GaAs is $\alpha$=5.6533 Å at room temperature (300 $^{o}$K). [Pierret]

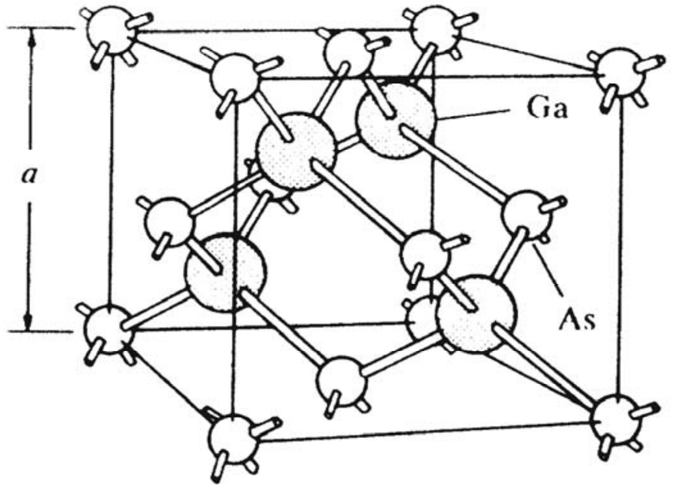

**Figure 3-1** The GaAs crystal structure. Gallium and Arsenic form two fcc sublattices that penetrate each other forming a new lattice with constant $\alpha$=5.6533 Å at 300 $^{o}$K.

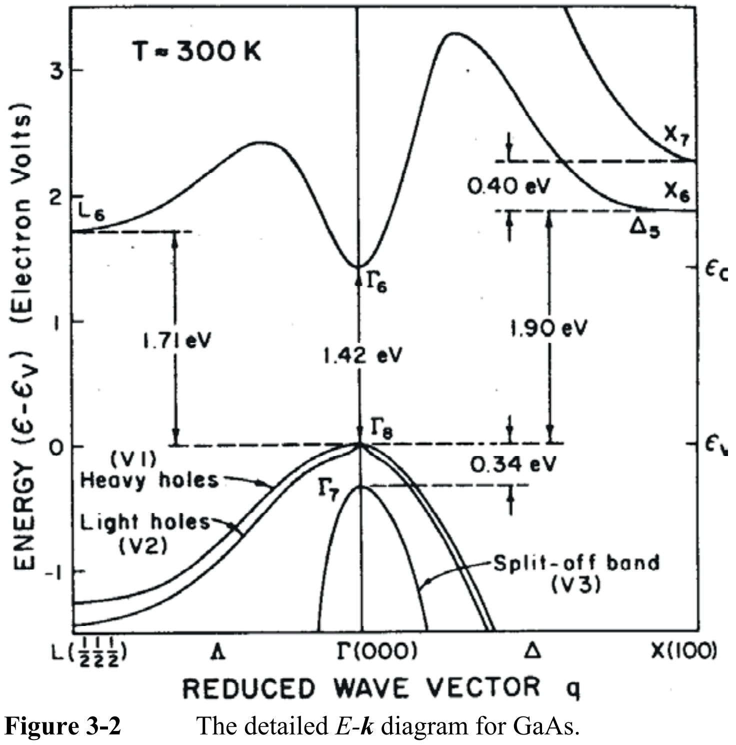

**Figure 3-2** The detailed *E*-***k*** diagram for GaAs.

The detailed band structure of GaAs is shown in **Fig. 3-2**. In general, the conduction band of semiconductor has more than one relative energy minima in ***k***-space. The absolute conduction minimum in GaAs occurs at ***k***=0, known as the Γ-point. The region around this minimum is appropriately known as the Γ-valley. GaAs also has relative minima at permutations of $\vec{k} = (111)\frac{\pi}{\alpha}$ and $\vec{k} = (100)\frac{\pi}{\alpha}$, where $\alpha$ is the lattice spacing. The eight permutations of $\vec{k} = (111)\frac{\pi}{\alpha}$ give rise to the symmetry points known as the L-points while the six permutations of $\vec{k} = (100)\frac{\pi}{\alpha}$ yield the X-points. Not surprisingly, the regions around these symmetry points are called the L-valleys and the X-valleys, respectively. In GaAs at room temperature, the direct energy gap at the Γ-point, which is also the minimum energy gap is equal to 1.42 eV. **Pierret** Pseudopotential calculations show the direct gaps at the L- and X- points to be about 3 and 5 eV respectively. **Chelikowsky** Also, the conduction-band minimum at the L-point is 0.29 eV above the Γ-point conduction-band minimum while that at the X-point exceeds that at the Γ-point by 0.48 eV. **Pierret, Siegal** The first Brillouin zone of reciprocal space for GaAs is shown in **Fig. 3-3**. **Blakemore**

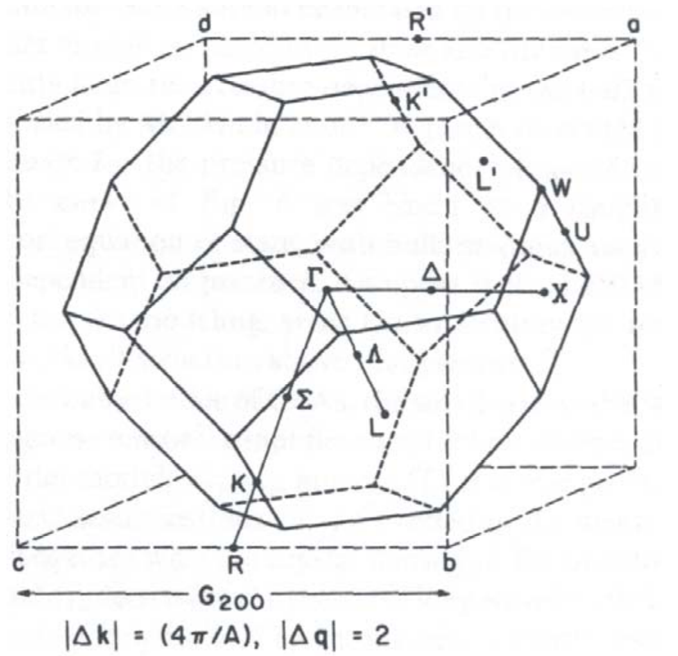

**Figure 3-3** The first Brillouin zone of reciprocal space of GaAs.

The band structure that is used in order to describe the physical mechanisms that are involved in this experimental study is depicted in **Fig. 3-4**. The figure presented is a simplified representation of the solution of Shroedinger equation using Bloch's theorem under the assumptions of the Kronig-Penney model. **Pierret** It is the extended-zone representation of the *E*-***k*** diagram of the potential in a semiconductor like GaAs. For the sake of simplicity, all discontinuities in the diagram have been omitted and a parabolic band structure has been utilized. The last two bands in the quantum structure of crystalline, defect-free GaAs are presented and their energy is plotted versus the ***k*** vector amplitude. The lower one is called valence band because all the electrons that lie in it are the valence electrons of the atoms that comprise the crystal. The higher one is called conduction band because any electrons that may be found in this band are considered to be free and thus conduct.

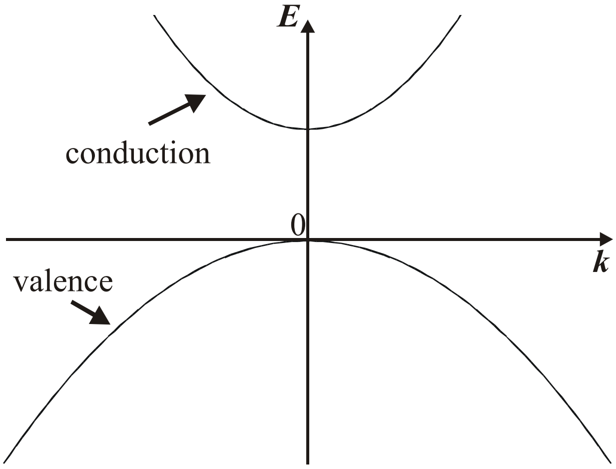

**Figure 3-4** The simplified *E*-***k*** diagram for GaAs, showing the (lower) valence and the (higher) conduction band.

Conductivity in a semiconductor is mediated both by the negatively charged electrons excited to the conduction band and by the positive holes in the valence band, left behind by the excited (missing) electrons. The conducting electrons and holes are often referred to collectively as free charge carriers or simply free carriers due to this property and are considered to be free or more correctly quasi-free from the attracting potential of the cores. The shape of both bands can be assumed to be parabolic. The different curvatures of the two bands are due to the different effective masses of electrons in the conduction band and holes in the valence band. To be more exact, it is the different curvature of the bands in the first place that causes the different effective masses of the carriers in the last two bands as can be readily seen by: **Pierret**

$$m^* \equiv \hbar^2 \frac{dk^2}{d^2E} \tag{3-1}$$

There is a forbidden area between the two bands called the bandgap which does not contain any allowed energy states. No electrons can be found in this forbidden area. The maximum of the valence band coincides in the ***k***-space with the minimum of the conduction band making GaAs a member of the family of the direct gap semiconductors. At 0 Kelvin degrees, where the semiconductor is completely unperturbed, the valence band is completely full with electrons bound in the attracting potential of the cores and the conduction band is completely empty.

### 3.2.2 Stoichiometric AlGaAs and alloys

The structure of stoichiometric AlGaAs ternary alloys is similar to stoichiometric GaAs. AlGaAs is a III-V semiconductor as both Ga and Al elements belong to the third column of the periodic table and As belongs to the fifth column. The concepts that differ from GaAs are the different effective masses and mobilities of carriers. The varying fraction of Al in the alloy results in a varying lattice parameter which in turn results in varying effective mass and mobility.

The band gap energy of $Al_xGa_{1-x}As$ alloys with respect to the Al mole fraction $x$, can be given by the formula: **Allali**

$$E_g(x) = E_g(0) + 1.429x - 0.15x^2 \tag{3-2}$$

for $T$=300 $^oK$ and for $0<x<0.4$ where $E_g(0)$ is the band gap energy of GaAs at room temperature. Note here that the above formula is valid only at room temperature and for Al mole fractions smaller than 40 %. A schematic giving the results of **Eq. 3-2** is given in **Fig. 3-5**. There exist more than one formulas in the literature that give the dependence of the AlGaAs band gap energy on (among others) the Al mole

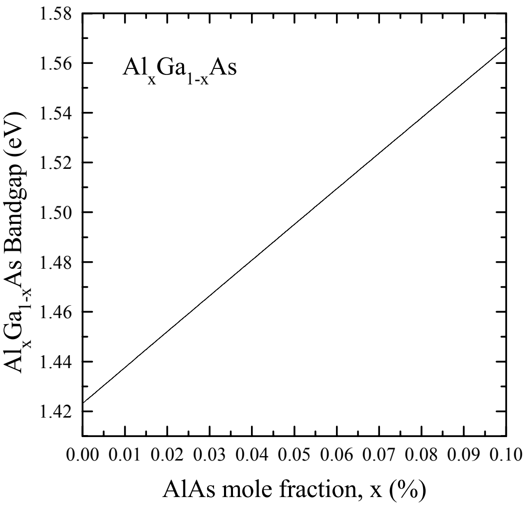

**Figure 3-5** The bandgap energy of AlGaAs with respect to the AlAs mole fractional composition.

fraction [Lourenco, Varshni, Paessler] but for the purposes of this work a high accuracy in determining the band gap energy is not imperative and we will restrict ourselves to the results given by Allalli et al. [Allali]

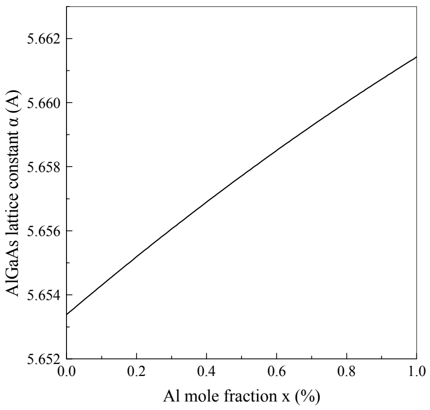

**Figure 3-6** Lattice constant with respect to the Al mole fraction.

The lattice constant of AlGaAs depends on the Al mole fraction, although that the lattice constants of GaAs and AlAs do not differ significantly. This fact is the reason why it is rather easy to construct this kind of alloys with a good crystalline structure. The formula that is used to obtain the dependence of the lattice parameter on the Al mole fraction *x*, is given by the empirical law: [Wasilewski]

$$\alpha_{AlGaAs}(x) = 5.65338 + 9.29\times10^{-3}\left(x - 0.134x^2\right)\text{Å} \qquad (3\text{-}3)$$

The result of **Eq. 3-3** is plotted in **Fig. 3-6**.

### 3.2.3

### Non stoichiometric GaAs

This section deals with GaAs grown via molecular beam epitaxy at unusually low substrate temperatures. Substrate temperatures can be as low as 150 $^{o}$C rather than the usual value of about 600 $^{o}$C. Hence, the most common in the bibliography term Low-Temperature-Grown GaAs, although it is an unfortunate one. During growth of GaAs layers at lower than normal temperatures, high concentration of excess As (up to 1.5 %) is incorporated and distributed in the lattice. This excess As leads to expansion of the lattice parameter. Annealing of the LTG-layers, either during growth or by ex-situ annealing, leads to the formation of As precipitates, a decrease of the lattice parameter to the substrate value and a decrease in the AsGa antisite defect concentration. The annealed layers show high resistivity, a large trap density and breakdown strengths about ten times that of normal GaAs. This material applied to photodetectors makes possible a temporal response in the sub-ps range. [Liliental1]

Much effort has been expended in order to understand the semi-insulating behavior and the short carrier lifetime of these layers. Two models exist to explain the properties of LTG-GaAs.

The first that tries to explain the semi-insulating behavior, is the defect model proposed by Look et al. [Look, Look2] Within their assumptions, two approaches might explain the semi-insulating behavior of LTG-GaAs. In the first one, they assume that there exists a $As_{Ga}$-related center with an

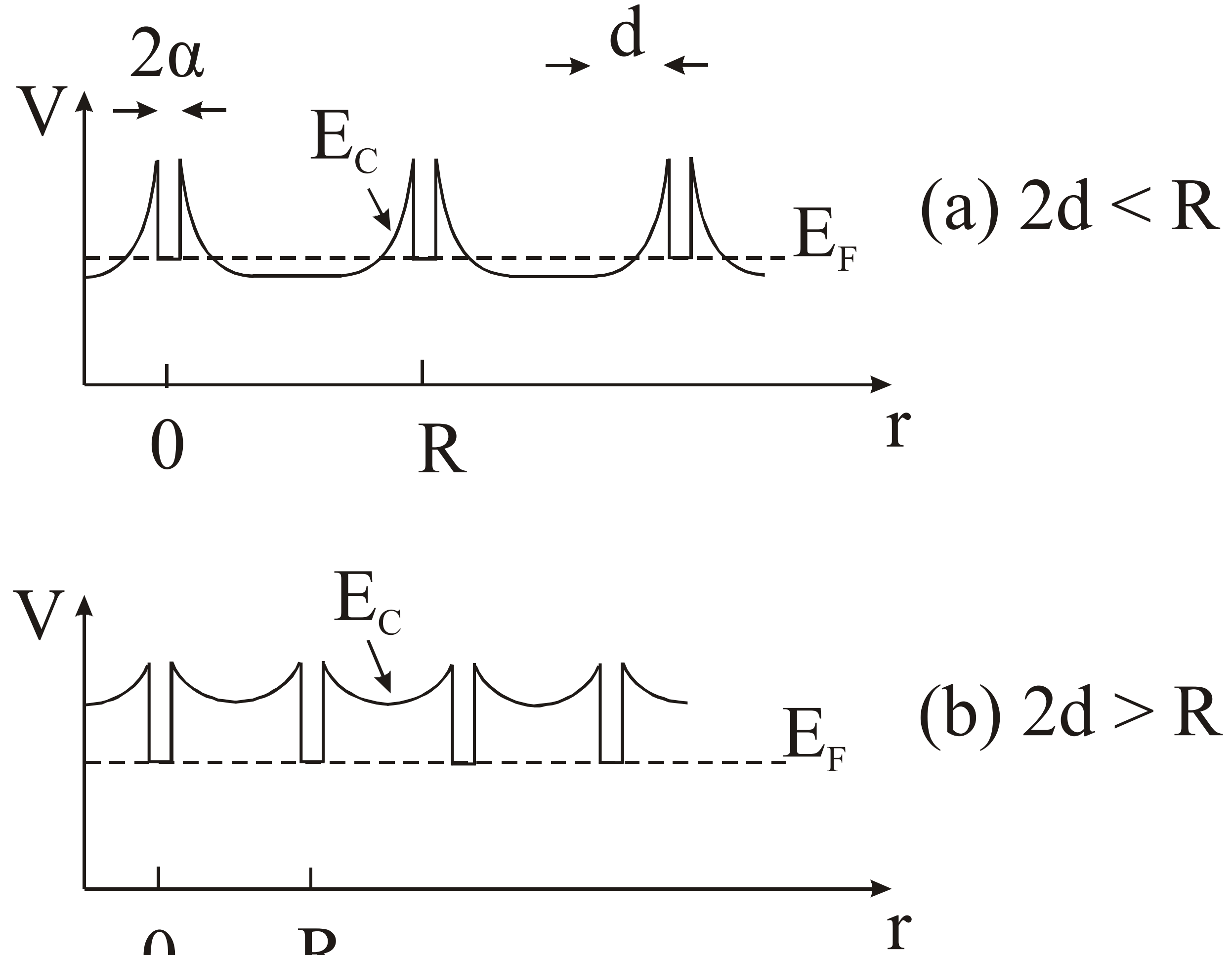

**Figure 3-7** Band bending for (a) low and (b) high As precipitate density in n-doped GaAs (taken from Warren et al. [Warren]).

energy of 0.65 - 0.70 eV. In the second one, they assume that there are two donors, one near 0.7 eV and the other near 0.5 eV. In both approaches, the existence of donors and acceptors near the center of the band gap is involved. The concentration of these antisite related defects decreases with increasing annealing temperature except some anomaly at the range of annealing temperatures around 300 - 400 °C. Near-infrared absorption measurements (NIRA) indicate that there are ~$10^{20}$ $cm^{-3}$ neutral As-antisite ($As_{Ga}^{0}$) –related defects in as-grown layers. As-deposited layers are conductive with hopping conductivity between the defect levels. However, when the layers are annealed, the density of these defects is decreased by two orders of magnitude. The density of defects approaches the level of donors observed in semi-insulating bulk GaAs or neutron-irradiated materials.

The second model explains the semi-insulating behavior by a buried Schottky barrier model. [Warren] According to this model, As clusters can be associated with Schottky barrier formation (**Fig. 3-7**) either through their role in generation of metal-induced gap states or in their role in native defect generation which pins the interface Fermi level at a value which corresponds to the Schottky barrier height. Within this model, As clusters will be surrounded by spherical depletion regions analogous to the planar regions at two dimensional metal GaAs interfaces, with characteristic barrier heights of 0.8 eV and 0.6 eV, for n- and p-type material respectively. When these depletion regions are isolated, namely for low cluster density and/or high doping density the GaAs will be partially compensated but still conducting. In contrast, for high cluster density and/or low doping density the GaAs will be completely depleted and semi-insulating. In **Fig. 3-7a**, the depletion radius *d* is smaller than the average As precipitate spacing *R*. The depletion regions with radius *d* do not overlap and thus the semiconductor is still conducting. In **Fig. 3-7b**, the *d* is bigger than *R*. In this case, through a tunneling mechanism, the carriers can be trapped in the Fermi level of the metal surface. Thus, the semiconductor becomes semi-insulating because of the lack of free carriers. The situation here refers to n, or p-doped semiconductor but the situation is similar to the intrinsic material as well, since barrier formation in GaAs is always existent independently of the metal contact or the doping level and type of the semiconductor. **Tersoff, Warren**

LTG-GaAs layers grown by MBE around and above 200 $^{o}$C are typically monocrystalline. However, it has been observed that the quality of the layers is thickness dependent. In MBE growth, lowering the growth temperature eventually leads to the termination of monocrystalline growth and a transition to an amorphous phase. This transition is explained by surface roughening that takes place at very low growth temperatures. At low temperature, formation of pyramidal defects having polycrystalline cores can take place if a specific critical layer thickness is exceeded. Incorporation of excess As in the layer is reciprocal to the growth temperature. The lower the growth temperature the more As is incorporated and the longer is the expansion of the lattice parameter. This leads to a tetragonal distortion of the layer due to excess As incorporation (expansion of the lattice parameter along the c axis). This explains the existence of the critical layer thickness and the strain build-up, which leads to the formation of dislocations. **Liliental1**

### 3.2.4 Non-stoichiometric AlGaAs

Like GaAs, AlGaAs is normally grown at temperatures around 600 $^{o}$C. The growth of the alloy in lower than the normal growth temperatures results in incorporation of excess As. This excess As initially is again found in the form of point defects, that is antisites and interstitials. Other defects like Ga vacancies always exist in the semiconductor matrix. Post growth annealing of the semiconductor results in the precipitization of the excess As into clusters or precipitates. The higher the anneal temperature and the longer the anneal time, the more effective the precipitization is. The precipitization of the As always occurs in expense of the As point defects. In a completely precipitized semiconductor, no As point defects should exist. **Melloch**

## 3.3 Optical properties

The electronic configuration of a material is the primary determinant of its optical properties. Classically, the higher charge-to-mass ratio of the electrons compared to that of the ions accounts for the more important role of the former in the optical response of a material. Quantum mechanically, this dominant role for the electrons arises because optical photon energies and the energy spacings between electronic levels fall in the same range. The energy spacings between ionic levels are much larger than optical photon energies, resulting in negligible transition probabilities. While electromagnetic radiation can produce collective excitations of the lattice by exciting phonons (lattice vibrations), phonon frequencies are generally in the far infrared, well below the frequencies of interest in this discussion. Thus, when light is incident on a material, it excites the electronic system without directly perturbing the ionic system. **Siegal**

It is seen so far that under no external perturbation at 0 degrees Kelvin, the valence band is completely full and the conduction band is completely empty. When the temperature rises, valence band electrons get thermally excited to the conduction band, where they get rid of the attracting potential of the cores and become very mobile. The higher the temperature, the bigger the possibility for an electron to be excited to the

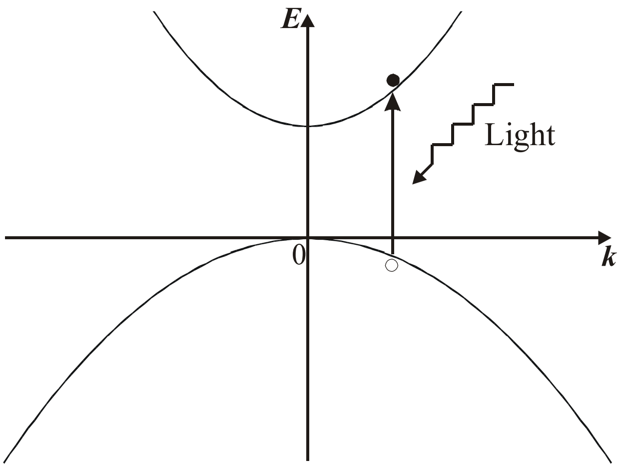

**Figure 3-8** Optical excitation of electrons from the valence to the conduction band.

conduction band, or equivalently, the more electrons we find in the conduction band as can be seen in: Pierret

$$n = N_c e^{\frac{(E_F - E_c)}{k_B T}} \tag{3-4}$$

However, at room temperature no or very little population is exited in the conduction band and can be considered to be zero for the purposes of this work.

The principle way to inject energy to the carriers is with the use of a light source and is shown in **Fig. 3-8**. As presented, the energy of the photons of the light source equals or exceeds the band gap energy. A bound electron can absorb all the energy of a photon and be excited to a higher electronic level in the conduction band. The photon vanishes. Furthermore, the initial and the final state of the electron has the same momentum since GaAs is a direct gap semiconductor (the momentum of a photon can be assumed to be negligible to that of an electron). An optically induced interband electronic transition must conserve energy and crystal momentum. Thus, transitions to the conduction band are allowed and excitation of the semiconductor under those circumstances is possible. Regarding the intensity of the light source, a population of electrons will emigrate to the conduction band leaving behind (in the valence band) an equal population of holes. Absorption of light in a semiconductor can occur either through interband or intraband

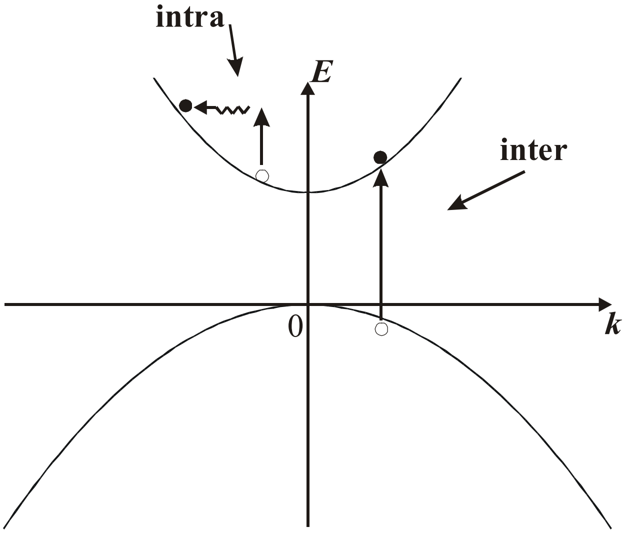

**Figure 3-9** Inter- and intra-band absorption in a semiconductor.

electronic excitations (**Fig. 3-9**). However, only when a significant number of electrons have been transferred from the valence to the conduction bands does intraband absorption, also known as free-carrier absorption, become an important mechanism for absorption of light. Usually, interband absorption is the principal mechanism for absorption of light in a semiconductor. [Siegal]

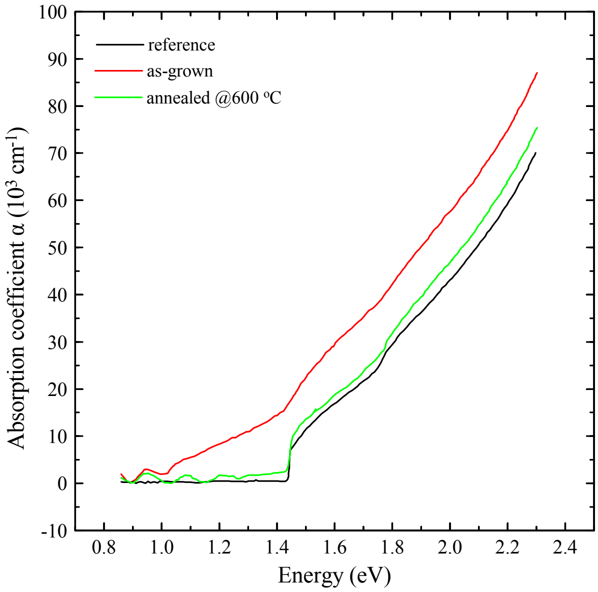

**Figure 3-10** Absorption spectra of GaAs samples grown at: normal temperature, at 250 °C and as-grown, and at 250 °C and annealed at 600 °C (taken from Dankowski et al. [Dankowski]).

Some examples of the linear absorption of GaAs are shown in **Fig. 3-10**. The black line corresponds to the sample grown in normal temperature and has the best possible crystalline structure. The absorption edge is 1.42 eV or 870 nm. Growing the sample in lower than the normal temperature results in As point defect formation and a typical absorption spectrum is shown with a red line in **Fig. 3-10**. It is clear that the point defect contributes to the absorption spectrum as a continuum background. When the sample is annealed at 600 °C, the As point defect concentration is expended in favor of As precipitates. The lattice constant of the sample returns back to the value of the normal grown GaAs and so does the absorption spectrum, as shown with a green line in **Fig. 3-10**. Note that the bandgap energy in all cases remains constant. [Dankowski] The situation is similar for AlGaAs as well but with a difference in the bandgap energy, depending on the Al mole fraction as already discussed.

## 3.4 Relaxation mechanisms

The following apply for III-V semiconductors in general and thus there will be no distinct reference between GaAs and AlGaAs. The optical excitation of electrons from the valence band to the conduction band in a semiconductor leads to a complicated set of processes through which the energy of the excited electrons is distributed to the rest of the electronic system as well as to the lattice. For quasi-monochromatic light, such as a laser pulse, electronic excitation can occur only in regions of ***k***-space satisfying the direct transition condition

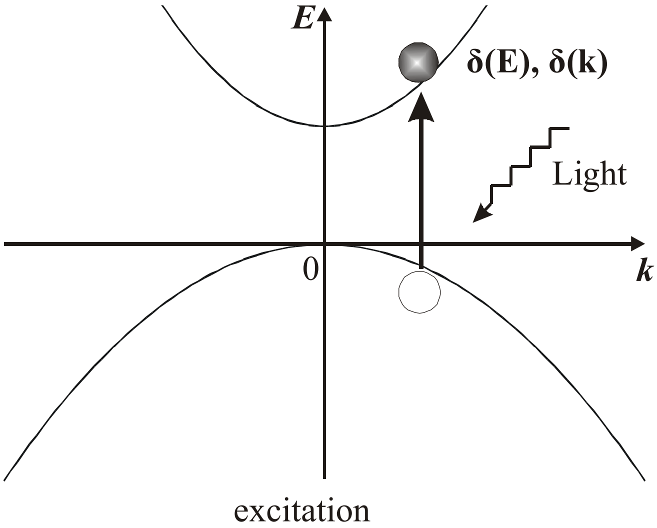

**Figure 3-11** The incident light creates a nonequilibrium population of free electrons with a narrow distribution of crystal momentum and energy.

$$E_{final}(\vec{k}) - E_{initial}(\vec{k}) = \hbar\omega \tag{3-5}$$

where $\omega$ is within the spectral bandwidth of the incident light. As a result, the incident light creates a nonequilibrium population of free carriers (electrons in the conduction band and holes in the valence band) with a very narrow distribution of crystal momentum (localized ***k***-space) and carrier energy, as shown in **Fig. 3-11**. [Othonos]

### 3.4.1 Carrier-carrier scattering

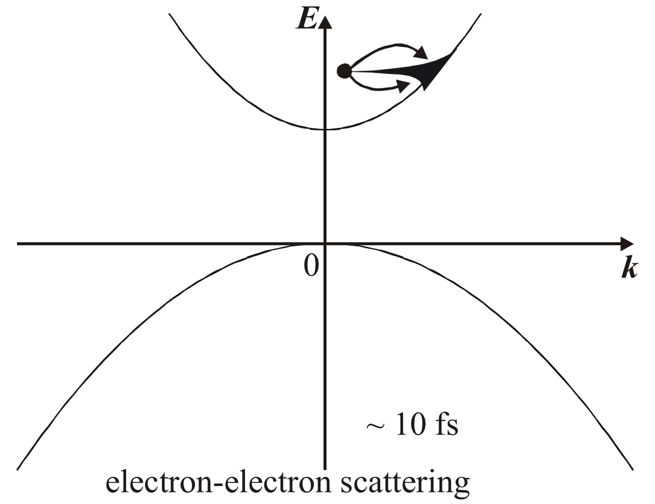

**Figure 3-12** The carrier-carrier scattering process imediately after excitation randomizes the carrier momenta and redistributes the energy. The figure is only a schematic. The electron in reality should "touch" the dispersion curve.

The nonequilibrium free-carrier population quickly spreads out in ***k***-space mainly through carrier-carrier scattering (**Fig. 3-12**). The time scale for electron-electron scattering decreases with increasing conduction electron density and is shorter than 20 fs (for a single event) for electron densities greater than $10^{18}$ cm$^{-3}$. Within one or few hundred fs, the initial, nonequilibrium distribution of free carriers becomes a thermalized Fermi-Dirac distribution (ensemble of events, **Fig. 3-12**). The temperature of this thermal distribution is set by the initial free-carrier excess energy, corresponding to the energy above the conduction band minimum for electrons and the energy below the valence band maximum for holes. Thus carrier-carrier scattering merely redistributes the energy among the excited electrons and holes and does not change the average energy of the excited free carriers. [Othonos]

Carrier-carrier scattering includes three similar but separate processes:

- electron-electron scattering
- hole-hole scattering
- electron-hole scattering

The first two lead to internal thermalization of the excited electron and hole populations while the third leads to equilibrium of the conduction electron population with the hole population in the valence band. Electron-hole equilibrium is driven by the initial difference in average excess energies between excited electrons and holes. In GaAs, for example, a difference between electron and hole excess energies arises during direct interband transitions in the Γ-valley because of the higher curvature of the conduction band compared to that of the valence band. [Siegal]

### 3.4.2 Carrier-phonon scattering

While the excited free carriers become internally thermalized within few hundred fs, they are still far out of equilibrium with the lattice on this time scale. Energy transfer from the excited electronic system to the lattice occurs through the slower process of carrier-phonon scattering, visualized in **Fig. 3-13**. The time scale for carrier-phonon scattering is longer than that for carrier-carrier scattering because the coupling of free carriers to phonons is weaker than the coupling of free carriers to each other under nonequilibrium conditions. Typical carrier-phonon scattering times are on the order of a few hundred fs. However, the phonons primarily responsible for cooling the hot electrons have energies that are on the order of 30 meV. So, for example, for initial electron excess energies on the order of 500 meV (corresponding to excitation of GaAs with 2 eV photons), significant energy transfer from the electrons to the lattice requires about 15 phonon emission events per electron. Thus, electron-lattice thermalization occurs on a time scale of a few ps. However, if the initial electronic excess energy is less than the minimum amount required for electron-phonon interaction

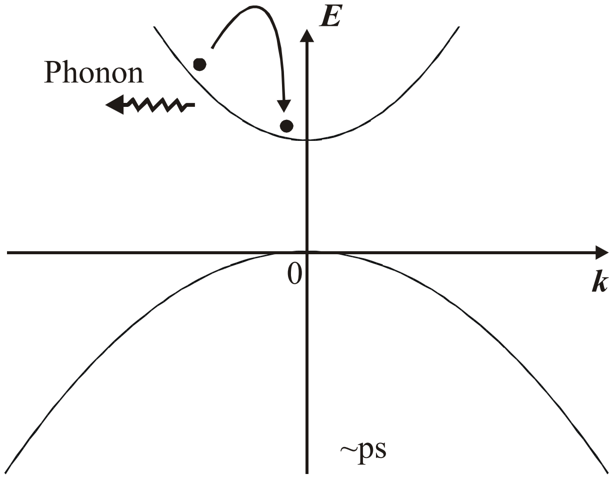

**Figure 3-13** Electron-phonon scattering.

(~30 meV), this process is absent.

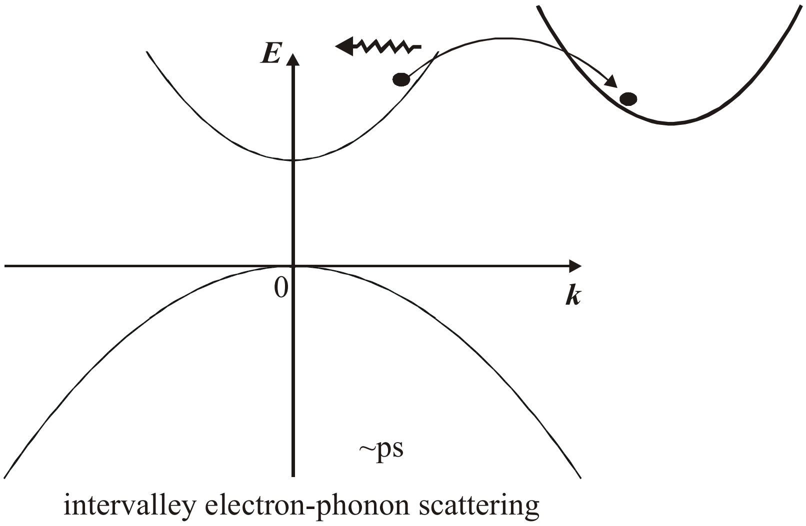

**Figure 3-14** Intervalley phonon scattering. Excited electrons scatter onto a different conduction band valley through phonon emission or absorption.

Intervalley phonon scattering, shown in **Fig. 3-14**, can also play an important role in energy transfer following the optical generation of free carriers. Siegal In intervalley scattering, excited electrons scatter onto a different conduction band valley through phonon emission or absorption. Since the various conduction band valleys are centered at very different values of crystal momentum, intervalley scattering requires large $|\vec{q}|$ (short wavelength) optical or acoustic phonons to satisfy the requirement of crystal momentum conservation. Thus, the deformation potential mediates this type of scattering. Note that intervalley scattering will not occur for an electron if its energy in the conduction band is lower than a phonon quantum below the minimum of the destination valley. In the experiments presented in this thesis, intervalley transfer of electrons is considered to be absent because electrons are excited at the vicinity of the conduction band edge, having an

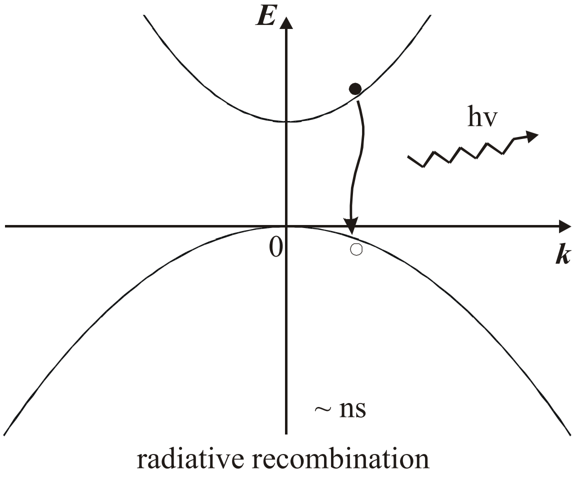

**Figure 3-15** Radiative recombination of an electron (with a hole). The released energy is emmited as a photon.

excess energy (10 – 20 meV) much smaller than the threshold for intervalley transition energy (0.48 eV).

### 3.4.3 Carrier recombination and diffusion

While the scattering processes discussed so far distribute the initial excitation energy throughout the electronic system and lattice, none of these processes changes the density of the excited free carriers. Two important processes that do change the free carrier density are carrier recombination and carrier diffusion. Carrier recombination, or electron-hole recombination, refers to processes in which an electron in the conduction band and a hole in the valence band recombine, as shown in **Fig. 3-15**. In other words, an electron previously excited to the conduction band makes a transition back down to the valence band. Carrier diffusion, on the other hand, refers to the average motion of free carriers from high carrier-density regions to low carrier-density regions (**Fig. 3-16**). Recombination lowers the total number of free carriers in a crystal while diffusion redistributes free carriers in real space. For the purposes of the work presented in this thesis, both types of processes reduce the number of free carriers in a local, laser-excited region. **Siegal**

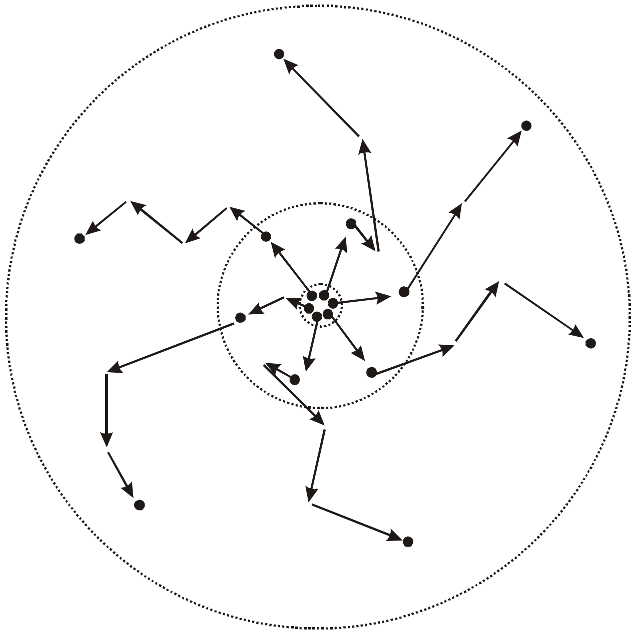

**Figure 3-16** A visualization of the diffusion process of electrons out of the initial high-concentration, laser-excited region. The dotted circles represent the time evolution of this process: the bigger the circle, the longer the elapsed time.

Time scales for recombination processes depend on the free carrier density and on the specific type of process. The various types of recombination differ according to how the energy lost by the electron in the downward transition to the valence band is given off. Two of the most important types of recombination are radiative recombination, in which the transition energy is radiated as a photon, and Auger recombination, in which the transition energy is transferred to another free carrier and are shown in **Fig. 3-17**. **Siegal**

A radiative recombination event occurs when a conduction band electron and a valence band hole annihilate each other, giving off a photon. Thus, the radiative recombination rate is proportional to the product of the conduction electron density times the hole density:

$$R_{radiative} = C_{radiative} np \tag{3-6}$$

where $n$ is the conduction electron density, $p$ is the density of holes in the valence band and $C_{radiative}$ is a constant. **Siegal** In the case of optical generation of free carriers in an intrinsic semiconductor, $n = p = N$, where $N$ is the density of electron-hole pairs. We can define an instantaneous recombination time $\tau_{radiative}$ by setting

$$R_{radiative=} = \frac{N}{\tau_{radiative}} \tag{3-7}$$

Then for radiative recombination, we have that

$$\tau_{radiative} = \frac{1}{C_{radiative} N} \tag{3-8}$$

In GaAs, $C_{radiative}$=7.2×$10^{-10}$ cm$^3$s$^{-1}$, giving a recombination time of about 1 ns for a carrier density on the order of $10^{18}$ cm$^{-3}$. For the ultrafast time domain that is investigated in this thesis, the contribution of radiative recombination can be considered to be negligible because of its long duration.

In contrast, an Auger recombination event involves three free carriers because the electron-hole annihilation transfers energy either to another conduction electron or to a hole in the valence band. Therefore, the Auger recombination rate $R_{Auger}$ in the case of optically generated free carriers with density $N$ is given by

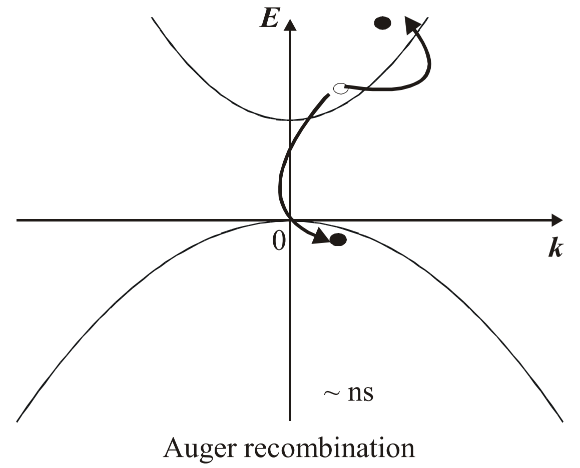

**Figure 3-17** Auger recombination. The energy is transferred to another free carrier.

$$R_{Auger} = C_{Auger} N^3 \tag{3-9}$$

This expression gives an instantaneous Auger recombination time of

$$\tau_{Auger} = \frac{1}{C_{Auger} N^2} \tag{3-10}$$

In GaAs, $C_{Auger}$ is on the order of $10^{30}$ cm$^6$s$^{-1}$ **Siegal** so Auger recombination becomes faster than radiative recombination at a carrier density of about $10^{21}$ cm$^{-3}$. In the work presented in this thesis, fs laser pulse excitation generates initial carrier densities much lower than the above value (in the order of $10^{17}$ cm$^{-3}$ maximum), so Auger recombination is a negligible recombination mechanism in this case.

Carrier diffusion is another important mechanism for reducing the free carrier density in the region excited by the laser pulse. The current density out of a local region is given by: **Pierret**

$$\begin{aligned} \vec{J}_p &= -qD_p \vec{\nabla} p \\ \vec{J}_n &= qD_n \vec{\nabla} n \end{aligned} \tag{3-11}$$

for holes and electrons respectively, where $D_p$ and $D_n$ are the corresponding diffusion coefficients and $q$ the charge of the carrier. Because of the higher effective masses of holes, the electrons are in most cases considered to be much more mobile than the holes so that electron diffusion is more effective than hole diffusion. The continuity equations reads:

$$\frac{d\rho}{dt} = -\vec{\nabla} \cdot \vec{J} \tag{3-12}$$

where $\rho = nq$ is the charge density. So, applying the continuity equation to the expression for the electron diffusion current we get the rate $R$ of the loss of electrons due to diffusion out of a local region:

$$R_{diffusion} = \frac{dn}{dt} = \frac{n}{\tau_{diffusion}} = D_n \nabla^2 n \tag{3-13}$$

If the laser spot size on the sample surface is much bigger than the absorption depth $\delta$, then the carrier density varies only in the direction normal to the sample surface:

$$n(z) = n(0)e^{-\frac{z}{\delta}} \tag{3-14}$$

In this case, the diffusion time is given by

$$\tau_{diffusion} = \frac{\delta^2}{D_n} \tag{3-15}$$

For example, an absorption depth of 500 nm (corresponding to linear absorption of 870 nm light in GaAs) and a diffusion constant on the order of 50 $cm^2$ $s^{-1}$ gives a diffusion time of roughly 50 ps.

The above discussion of energy transfer in a semiconductor is not meant to be a comprehensive treatment of this expansive subject. Many other scattering mechanisms play a role in the distribution of the laser-deposited energy, such as scattering with plasmons (collective electronic excitations), impurity scattering and combinations of the above. A full review of these processes can be found in Semiconductor Physics, by K. Seeger. [Seeger] The goal of this section is to provide a sense for the relevant time scales for energy transfer following fs laser pulse excitation of a semiconductor. In particular, carrier-carrier scattering thermalizes the free carrier population within a few hundred fs, carrier-phonon scattering leads to carrier-lattice equilibration on a time scale of a few ps and carrier recombination and diffusion reduce the free carrier density in the excited region in several tens to several hundreds ps.

## 3.5 References

**Allali** M. El Allali, C. B. Sorensen and E. Veje, Phys. Rev. B **48**, 4398 (1993).

**Blakemore** J. S. Blakemore, J. Appl. Phys. **53**, R123 (1982).

**Chelikowsky** J. R. Chelikowsky and M. L. Cohen, Phys. Rev. B **14**, 556 (1976).

**Dankowski** S. U. Dankowski, D. Streb, M. Ruff. P. Kiesel, M. Kneissl, B. Knuepfer, G. H. Doehler, U. D. Keil, C. B. Soerenson, and A. K. Verma, Appl. Phys. Lett. **68**, 37 (1996).

**Liliental1** Z. Liliental-Weber, J. Ager, D. Look, X. W. Lin, X. Liu, J. Nishio, K. Nichols, W. Schaff, W. Swider, K. Wang, J. Wasburn, E. R. Weber, and J. Whitaker, Semi-insulating III-V Materials Warsaw, Poland, p.305 (1994).

**Look** D. C. Look, G. D. Robinson, J. R. Sizelove, and C. E. Stutz, J. Elec. Mat. **22**, 1425 (1993).

| | |
|---|---|
| **Look** | D. C. Look, D. C. Walters, G. D. Robinson, J. R. Sizelove, M. G. Mier, and C. E. Stutz, J. Appl. Phys. **74**, 306 (1993). |
| **Lourenco** | S. A. Lourenco, I. F. L. Dias, J. L. Duarte, E. Laureto, E. A. Meneses, J. R. Leite, and I. Mazzaro, J. Appl. Phys. **89**, 6159 (2001). |
| **Melloch** | M. R. Melloch, D. D. Nolte, J. M. Woodall, J. C. P. Chang, D. B. Janes, and E. S. Harmon, Critical Reviews in Solid State and Materials Sciences **21**, 189 (1996). |
| **Melloch2** | M. R. Melloch, K. Mahalingam, N. Otsuka, J. M. Woodall, and A. C. Warren, J. Cryst. Growth **111**, 39 (1991). |
| **Melloch3** | M. R. Melloch, N. Otsuka, J. M. Woodall, A. C. Warren, and J. L. Freeouf, Appl. Phys. Lett. **57**, 1531 (1990). |
| **Matyi** | R. J. Matyi, M. R. Melloch, and J. M. Woodall, Appl. Phys. Lett. **60**, 2642 (1992). |
| **Othonos** | A. Othonos, J. Appl. Phys., **83**, 1789 (1998). |
| **Paessler** | R. Paessler, Phys. Status Solidi B **200**, 155 (1997). |
| **Pierret** | R. F. Pierret, "Advanced Semiconductor Fundamentals", Modular Series on Solid State Devices, Addison-Wesley Publishing Company, Volume VI, (1987). |
| **Seeger** | K. Seeger, "Semiconductor Physics", in Solid State Sciences, Springer. |
| **Siegal** | Y. Siegal, Thesis, Harvard University, Cambridge, Massachusetts, (1994). |
| **Tersoff** | J. Tersoff, Phys. Rev. Lett. **52**, 465 (1984). |
| **Varshni** | Y. P. Varshni, Physica (Utrecht) **34**, 194 (1967). |

**Warren** A. C. Warren, J. M. Woodall, J. L. Freeouf, D. Grischkowsky, D. T. McInturff, M. R. Melloch, and N. Otsuka, Appl. Phys. Lett **57**, 1331 (1990).

**Wasilewski** Z. R. Wasilewski, M. M. Dion, D. J. Lockwood, P. Poole, R. W. Streater, and A. J. SpringThorpe, J. Appl. Phys. **81**, 1683 (1997).

# Chapter 4 GaAs & AlGaAs: Electron Trapping

## 4.1 Introduction

Low-temperature-grown Gallium Arsenide (LTG-GaAs) [Murotani] has been a subject of intensive research during the past decade because it exhibits properties like high mobility, resistivity, crystalline quality, and ultrafast electro-optic behavior. [Warren, Gupta, Kaminska] The designing of high quality and ultrafast response optoelectronic devices [Witt] requires the understanding of the dependence of these properties on the fundamental structural parameters of the material.

Annealed LTG-GaAs has been shown to contain excess Arsenic (As) only in the form of As clusters (precipitates) under proper annealing conditions of temperature and time. [Melloch, Melloch4] The ultrafast electronic behaviour of the annealed material is attributed to carrier trapping on the surface of the As clusters. [Warren, Melloch, Schaff, Gupta, Lochtefeld] The replacement of a fraction of Ga with Al during growth results in a series of AlGaAs alloys that are a key material in constructing quantum wells that also exhibit interesting optoelectronic properties [Lahiri, Feng] and are used in ultrafast devices. Furthermore, the tunability offered by the Al mole fraction in AlGaAs makes this material very important in optoelectronic device engineering. Thus, good knowledge of the ultrafast electronic behavior of alloys of this category is a key issue in the ultrafast optoelectronic applications area.

Many research groups have studied the carrier trapping and recombination times for LTG-GaAs with respect to the growth and annealing conditions. [Schaff, Fauchet, Liliental, Lochtefeld, Harmon, Siegner, Loka, Marcinkevicius, Liliental2, Liliental3, McIntosh] However, little effort has been expended to associate the ultrafast behaviour directly to the As precipitate characteristics themselves. [Harmon, Melloch2] In LTG-AlGaAs and related alloys, where the effect of the low-temperature growth is similar to GaAs, [Mahalingam] the ultrafast electronic behavior is even less studied and the picture is still very unclear. [Melloch2, Melloch, Melloch3]

The scope of this work is to investigate the effect and interplay of the most basic structural parameters of the As precipitates, namely their spacing and size, on the photoexited electron trapping times. Also, it is our intention to compare our compiled data for LTG-GaAs with data for LTG-AlGaAs and to investigate whether the trends observed for trapping times in LTG-GaAs are applicable for LTG-AlGaAs as well, thus giving the possibility of further extending the model to III-V semiconductors.

In this chapter, the experimental results from the pump-probe measurements on various GaAs and AlGaAs samples are presented, followed by analysis, discussion and comparison with existing results in the bibliography. Also, the preparatory conditions and the characterization procedure of the samples are presented.

## 4.2 Growth and preparation

All samples used in the work presented in this chapter (LTG-GaAs and LTG-AlGaAs) have been prepared by research personnel in the Microelectronics Laboratories in the Physics Department of the University of Crete (growth: Prof. Z. Hatzopoulos, lift-off and etching: Mr. M. Sfendourakis and Dr. G. Konstantinidis). The sample code names and the corresponding growth characteristics are presented in **Tab. 4-1** and **Tab. 4-2** for LTG- GaAs and LTG-AlGaAs respectively.

The samples studied in this work are grown in a VG V80H solid-source molecular beam epitaxy (MBE) system on (001) semi-insulating GaAs substrates. The growth temperature is measured by a calibrated thermocouple placed in the vicinity of the molyblock. The ratio of group V to group III beam equivalent pressure is 20 and the growth rates are typically 1 μm/hr for GaAs and AlAs respectively. After the desorption of the native oxide at 580 $^{o}$C, a 250 nm buffer layer is grown followed by a 500 Å AlAs sacrificial layer. The AlAs sacrificial layer for the LTG-GaAs samples is grown in order to be used for lift-off process discussed below. Growth is then

| Code name | Growth Temperature ($^{o}$C) | Annealing Temperature ($^{o}$C) | Annealing Time (min) |
|---|---|---|---|
| GaAs-113 | 170 | 600 | 20 |
| GaAs-181 | 185 | 600 | 30 |
| GaAs-112 | 200 | 600 | 20 |
| GaAs-87 | 250 | 600 | 30 |
| GaAs-107 | 300 | 600 | 30 |
| GaAs-206 | 325 | 600 | 20 |
| GaAs-106 | 600 | 600 | 0 |

**Table 4- 1** GaAs sample code names, growth and annealing temperatures and annealing times.

interrupted, the substrate temperature is ramped down to the desired low temperature (170 to 600 $^{o}$C) and a ~ 1 μm of LTG-GaAs is grown. A reference sample is also grown with the 1 μm thick GaAs layer grown at 580 $^{o}$C. The same growth sequence is used for the LTG-AlGaAs samples with the exception of the sacrificial AlAs layer. The flux ratio of Ga to Al is adjusted so that the Al mole fraction in the AlGaAs structures stays just below 10 %. We are interested to keep the Al mole fraction low enough so that the bandgap energy of the samples will stay in the limits of the wavelength operation of the laser system. In situ Reflection High-Energy Electron Diffraction (RHEED) is used during growth, in order to monitor the evolution of the grown front. Immediately after the growth completion, the samples are annealed for 20 to 30 min at 600 $^{o}$C in $As_4$ overpressure in the MBE system.

In order to measure the pump-probe transmission changes through the samples, the underlying substrate must be removed. This can be achieved by the lift-off procedure for the case of the LTG-GaAs samples. The purpose of this procedure is to lift the LTG sample-epilayers off their substrates. The samples are first cut to parallelograms with dimensions of about 5 mm × 10 mm. Then, the as-grown material is cleaned from any surface impurities by plunging into trichloroethene. The samples are then inserted into acetone to dissolve trichloroethene and then they are plunged into isopropanole to remove the acetone. Subsequently, distilled water is used to

| Code name | Growth Temperature ($^{o}$C) | Annealing Temperature ($^{o}$C) | Annealing Time (min) |
|---|---|---|---|
| AlGaAs-225 | 200 | 600 | 30 |
| AlGaAs-227 | 225 | 600 | 30 |
| AlGaAs-210 | 250 | 600 | 30 |
| AlGaAs-211 | 250 | 600 | 30 |
| AlGaAs-229 | 275 | 600 | 30 |
| AlGaAs-228 | 300 | 600 | 30 |
| AlGaAs-226 | 325 | 600 | 30 |
| AlGaAs-224 | 350 | 600 | 30 |

**Table 4-2** AlGaAs sample code names, growth and annealing temperatures and annealing times.

remove isopropanole. After drying the samples, they are heated to 114 $^{o}$C and a uniform layer of wax is laid on the surface. The samples are left heated for about 15 min for the wax layer to smoothen. The sample perimeters are then cleaned from the wax using trichloroethene. Then the samples are plunged into a ~ 10 % solution of $HF/H_2O$ that selectively interacts only with the intermediate AlAs layer. After a period of a few (2-3) weeks the epi-layer cuts off from the substrate and with the use of a thin hair it is lifted off and deposited on a glass substrate. The remaining acid is cleaned off with distilled water.

For the LTG-AlGaAs epilayers, a different procedure (etching) is followed. The LTG-AlGaAs epilayers are mechanically lapped down to 25 μm ± 20 μm. Then, they are chemo-mechanically polished. Following, resist is applied to them and a small portion towards one edge of the samples is exposed and developed. The exposed semiconductor area is wet etched in ($1H_2SO_4$: $8H_2O_2$: $4H_2O$) until the semiconductor is completely etched away. Following the resist removal, the actual thickness of the sample is measured and the etching rate is calculated to be ~ 850 Å /s. Then, the sample is again covered with resist and a 3 mm diameter hole is patterned in the middle of the sample. The sample is subsequently etched in ($1H_2SO_4$: $8H_2O_2$: $4H_2O$) in order to reveal the AlGaAs layer. In most cases as soon as the AlGaAs layer is reached its reddish appearance becomes evident.

## 4.3 Sample characterization

### 4.3.1 Structure characterization

The structural characterization of all the LTG epilayers has been performed by research personnel in the laboratories of the Aristoteles University of Thessaloniki under the supervision of

Prof. I. Stoimenos. The structural characterization of the samples is performed using the Transmission Electron Microscopy (TEM) technique. The principle of this technique is shown in **Chap. 2**. It is capable of measuring the structural characteristics of samples that can contain nanoparticles with dimensions even down to approximately 1 nm. Thus, we are able to obtain information for the shape, density and size of the nanoparticles that are formed in all our samples during their growth.

For the TEM characterization of the LTG-GaAs epilayers, the proper samples are those that are not yet subject to the lift-off procedure, but those that contain both the LTG-GaAs epilayer and the underlying substrate, as grown in the MBE chamber. A typical cross-section TEM micrograph obtained from an LTG-GaAs sample (grown at 170 $^{o}$C and annealed at 600 $^{o}$C for 20 min) is shown in **Fig. 4-1**. The top of the picture corresponds to the outer surface of the epilayer. The bottom of the picture shows the AlAs sacrificial layer that is grown for the lift-off procedure and separates the LTG epilayer from the underlying substrate. The sample is singe-crystalline. As precipitates are observed that are homogeneously distributed all over the LTG-GaAs epilayer. Also a few cracks and macroscopic defects are observed near the surface of the LTG-epilayer.

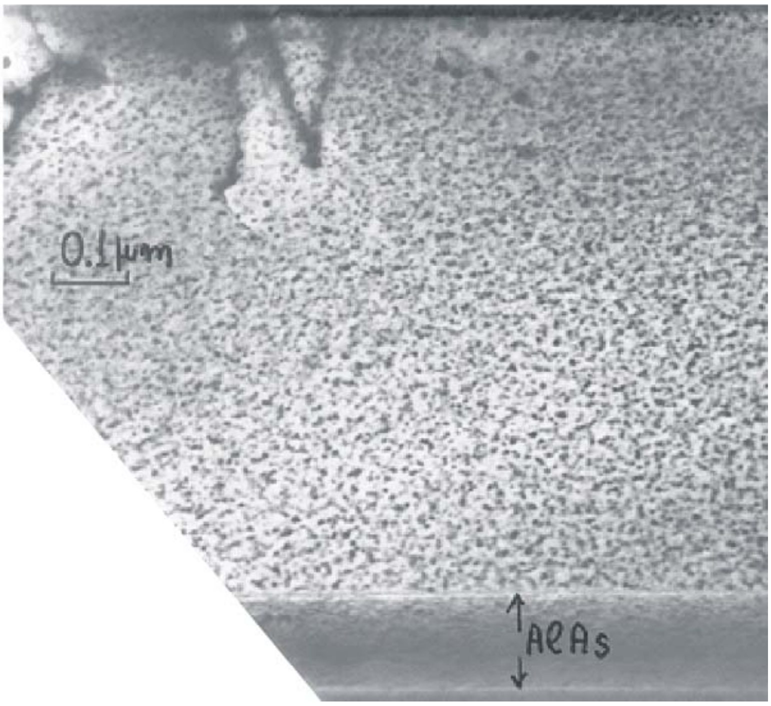

**Figure 4-1** A typical TEM micrograph for LTG-GaAs grown at 170 $^{o}$C. The top is the outer surface and the bottom shows the AlAs layer that separates the LTG epilayer from the substrate.

For the same epilayer, a high-magnification TEM micrograph is also obtained. The corresponding picture is shown in **Fig. 4-2**. From this figure, we are able to obtain the density and average size of the As precipitates. This figure also shows that the As precipitates are nearly spherical in shape.

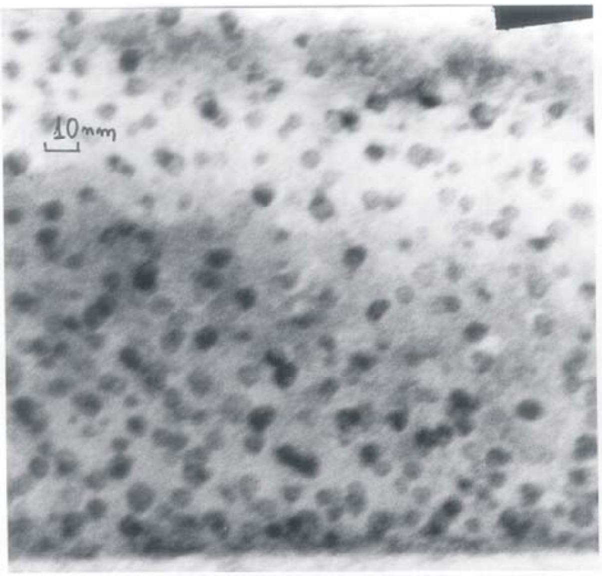

**Figure 4-2** High magnification TEM micrograph for an LTG-GaAs epilayer grown at 170 $^{o}$C and annealed at 600 $^{o}$C for 20 min. As precipitates are clearly distinguished. Their density and mean size can be obtained. Their shape is nearly spherical.

Typical TEM micrographs for two more LTG-GaAs samples are shown in **Fig. 4-3**. In general, the same observations can be extracted for all the samples: The As precipitates are nearly spherical in shape and are homogeneously distributed all over the LTG-GaAs epilayers. Also, the density and mean radii can be obtained for all the samples that contain observable precipitates from their corresponding high-magnification cross-section micrographs. The general trend that is observed is that the lower the

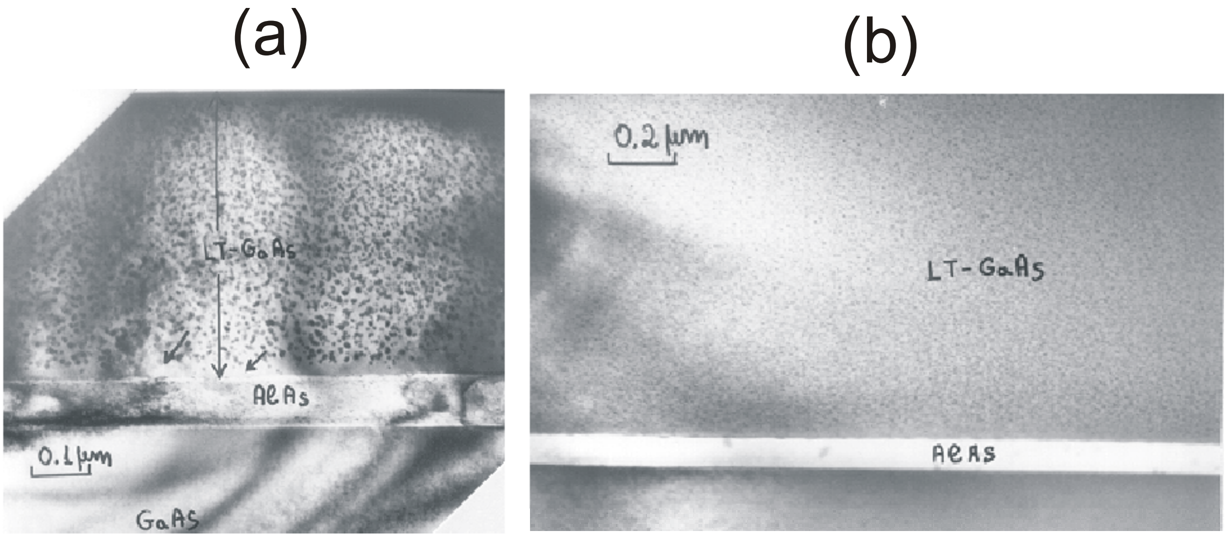

**Figure 4-3** TEM pictures for LTG-GaAs epilayers grown at (a) 185 $^{o}$C and (b) 275 $^{o}$C.

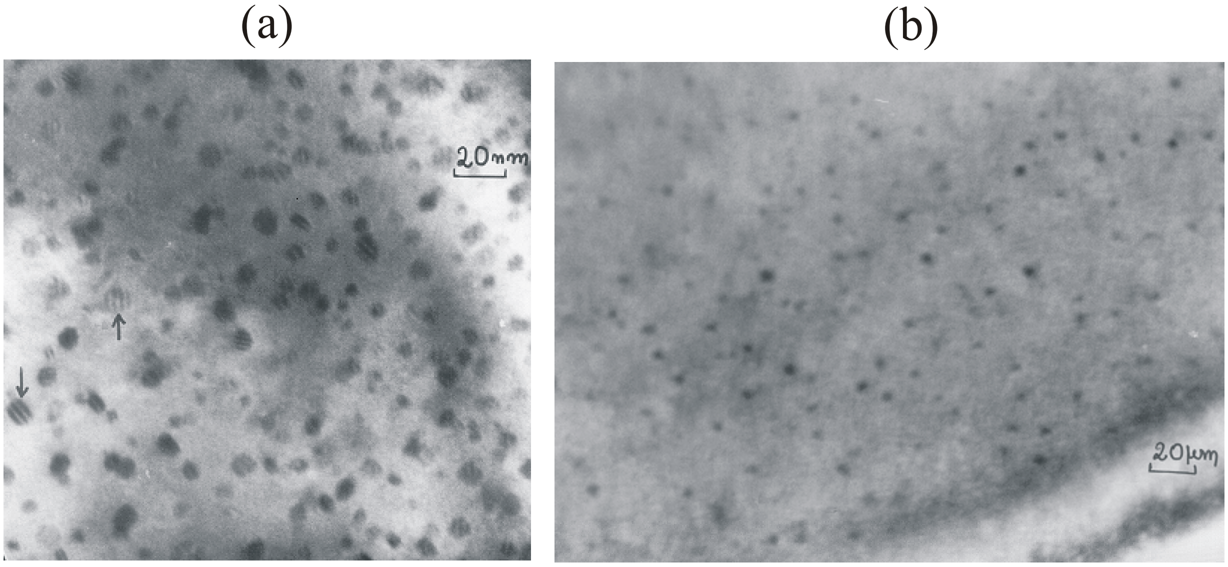

**Figure 4-4** High magnification TEM micrograph for two different LTG-GaAs epilayers grown at (a) 185 °C and (b) 275 °C. The difference in the density and the size of the As precipitates is evident.

growth temperature of the LTG-GaAs epilayers, the higher the density and the bigger the radius of the As precipitates as obtained by high magnification cross-sectional TEM micrographs, shown in **Fig. 4-4**.

The results for the densities and mean sizes of the As precipitates with respect to the growth temperatures of the epilayers are summarized in **Tab. 4-3**.

| **Specimen** | **$T_{growth}$ ($^oC$)** | **As density ($cm^{-3}$)** | **As diameter (nm)** |
|---|---|---|---|
| | | | |
| GaAs 113 | 170 | $2\times10^{17}$ | 5 |
| GaAs 181 | 185 | $5\times10^{16}$ | 6 |
| GaAs 112 | 200 | $1\times10^{17}$ | 4.9 |
| GaAs 87 | 250 | $3.4\times10^{16}$ | 3.4 |
| GaAs 107 | 300 | $1\times10^{16}$ | 3.6 |
| GaAs 206 | 325 | $2.5\times10^{15}$ | 2.5 |
| GaAs 207 | 350 | ? | ? |

**Table 4-3** Structure data for the LTG-GaAs epilayers

For the TEM characterization of the LTG-AlGaAs samples the un-etched samples are used, as grown in the MBE chamber as in the case of LTG-GaAs. A typical cross-section TEM micrograph is shown in **Fig. 4-5**. The top of the picture corresponds to the outer surface of the epilayer. The bottom of the picture shows the underlying substrate. The sample is singe-crystalline and As precipitates are observed that are homogeneously distributed all over the LTG-AlGaAs epilayer.

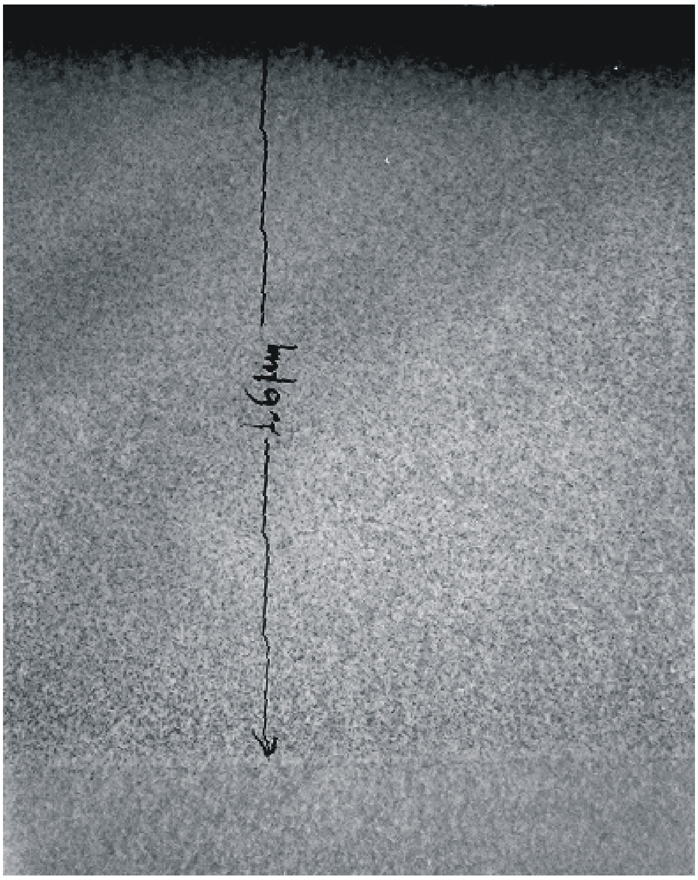

**Figure 4-5** LTG- AlGaAs grown at 250 °C and annealed at 600 °C for 30 min. The difference with the LTG-GaAs epilayers is the absence of the sacrificial AlAs layer. Here, the LTG epilayer contacts the GaAs substrate.

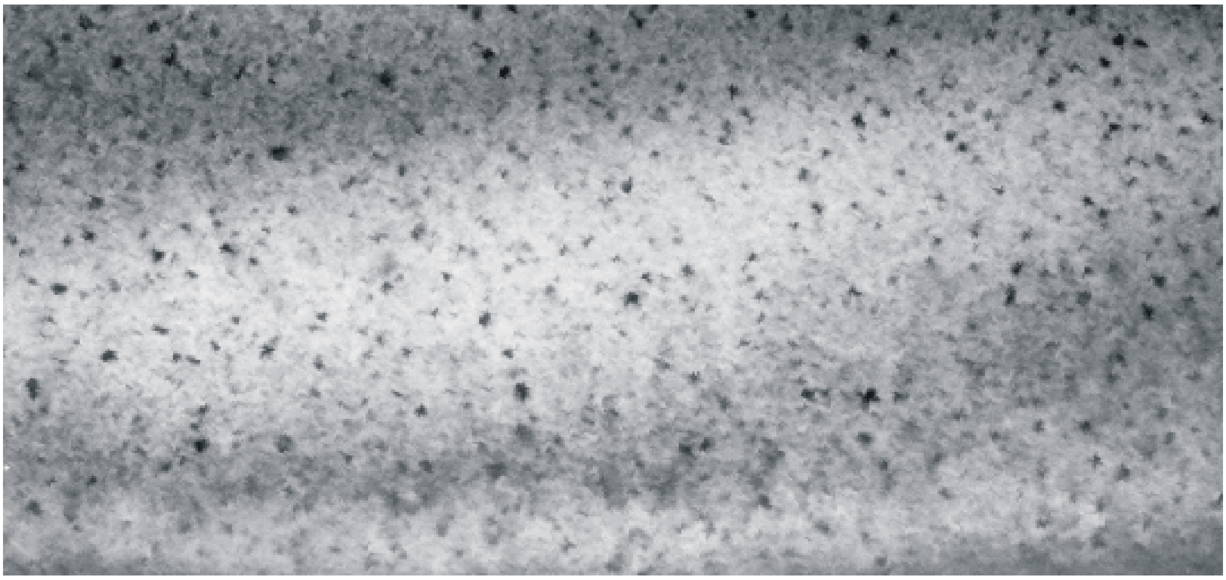

**Figure 4-6** High magnification of LTG-AlGaAs grown at 250 °C and annealed at 600 °C for 30 min. The As precipitates are nearly spherical in shape and the mean radii and density can be obtained.

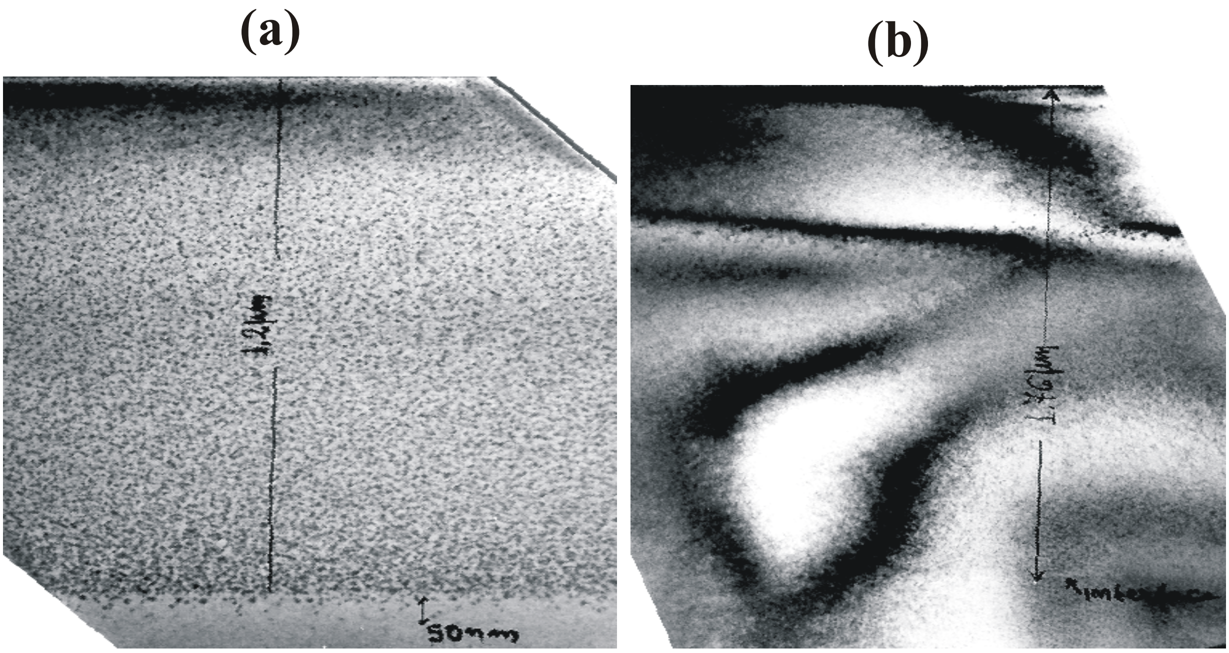

**Figure 4-7** TEM micrographs for LTG-AlGaAs annealed at 600 $^oC$ for 30 min and grown at (a) 200 $^oC$ and (b) 300 $^oC$. In (b) the precipitates are very few and the interface between the epilayer and the substrate is hardly distinguishable.

For the same epilayer, a high-magnification TEM micrograph is also obtained. The corresponding picture is shown in **Fig. 4-6**. From this figure, we are able to obtain the density and average size of the As precipitates. This figure also shows that the As precipitates are nearly spherical in shape.

Typical TEM micrographs for other LTG-AlGaAs samples are shown in **Fig. 4-7**. Similarly to the LTG-GaAs samples, the As precipitates are nearly spherical in shape and are homogeneously distributed all over the LTG-AlGaAs epilayers. Also, the density and mean radii can be obtained for all the samples that contain observable precipitates. The general trend that is observed is that the higher the growth temperature of the LTG-AlGaAs epilayers, the lower the density and the bigger the radius of the As precipitates as obtained by typical high magnification cross-sectional TEM micrographs shown in **Fig. 4-8**.

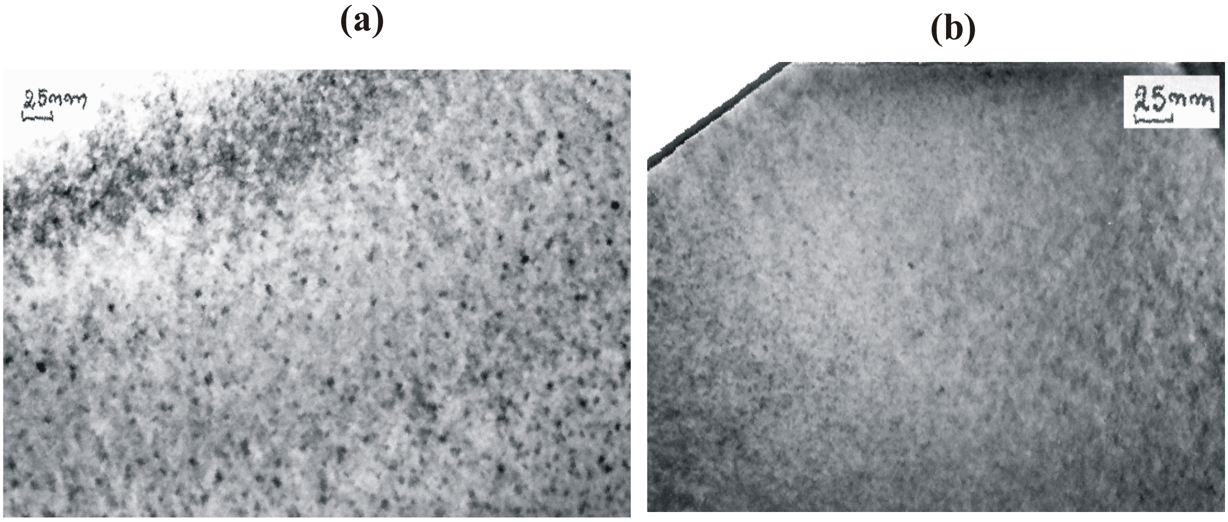

**Figure 4-8** High magnification cross-sectional TEM micrographs for AlGaAs epilayers annealed at 600 °C for 30 min and grown at (a) 200 °C and (b) 300 °C. In (b) very few precipitates are observed.

The results for the densities and mean sizes of the As precipitates with respect to the growth temperatures of the epilayers are summarized in **Tab. 4-4**.

In **Fig. 4-9**, **Fig. 4-10**, **Fig. 4-11**, **Fig. 4-12**, the reader can see plotted the results for the mean diameter and the density (inverse spacing) of the As precipitates with respect to the growth temperature for the LTG-GaAs and LTG-AlGaAs samples respectively. Despite the dispersion of the data, the trend is clear for both the density and the diameter versus the growth temperature. Note that for both materials the behavior of the data with respect to the growth temperature is quite similar. The only differences are observed for the absolute values of the data. The solid lines are

| Specimen | $T_{growth}$ (°C) | As density ($cm^{-3}$) | As diameter (nm) |
|---|---|---|---|
| | | | |
| AlGaAs-225 | 200 | $3.6x10^{16}$ | 4.17 |
| AlGaAs-227 | 225 | $6x10^{16}$ | 3.83 |
| AlGaAs-210 | 250 | $3.3x10^{16}$ | 3.55 |
| AlGaAs-229 | 275 | $1.2x10^{16}$ | 3.00 |
| AlGaAs-228 | 300 | $1.2x10^{15}$ | 2.50 |
| AlGaAs-226 | 325 | - | - |

**Tab. 4-4** Structure data for the LTG-AlGaAs epilayers

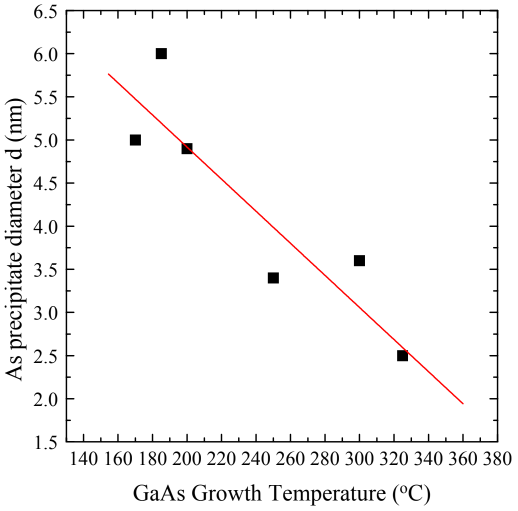

**Figure 4-9** The diameter of the As precipitates versus the growth temperature of the GaAs epilayers. The higher the temperature, the lower the precipitate diameter. The dependence is close to linear.

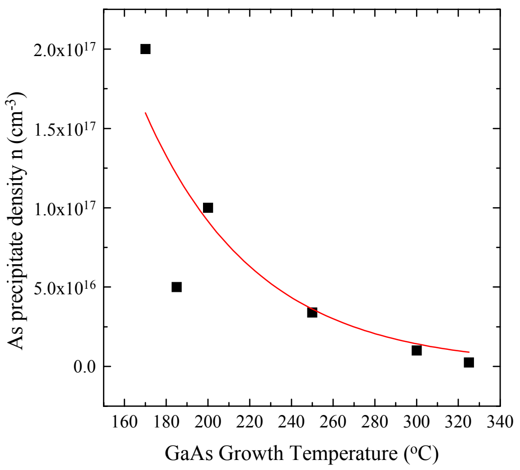

**Figure 4-10** As precipitate density versus $T_{growth}$. The function used for extrapolation is an exponential decay.

extrapolations based on the data. For example, for the diameter (or radius) versus the growth temperature the behavior is very close to a linear one, while for the density versus $T_{growth}$ it is close to an exponential rise for the temperature interval that is used. In the calculations to follow in this chapter, only the raw data have been used, however, both the raw data and the extrapolations give

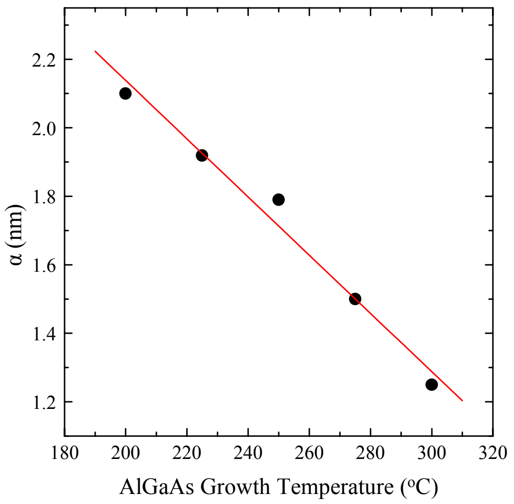

**Figure 4-11** The mean radii of the As precipitates in the LTG-AlGaAs samples with respect to the growth temperature.

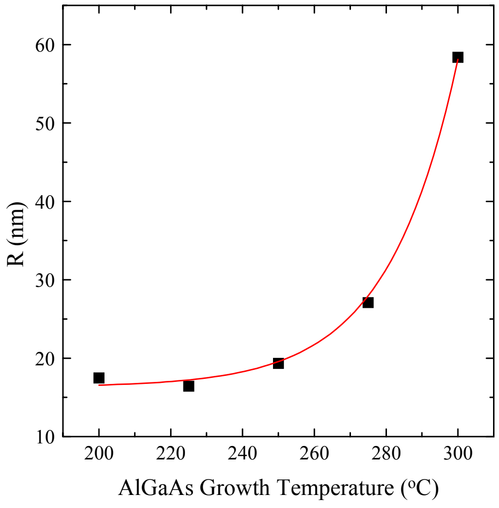

**Figure 4-12** The As precipitate spacing *R* of the LTG-AlGaAs samples versus the growth temperature.

almost the same results.

### 4.3.2 Optical characterization

The optical properties of normal grown GaAs are well established in the literature. [Blakemore] Measurements of the reference GaAs samples, grown at normal conditions (600 °C) are plotted with black line in **Fig. 4-13**. The GaAs exhibits an absorption edge that corresponds to electron transitions from the top of the valence band to the vicinity of the bottom of the conduction band. In **Fig. 4-13**, a typical absorption spectrum from a LTG sample is presented with red line. As can be seen, the features in this absorption spectrum are nearly the same as in the case of the sample grown under normal conditions The only difference is a bluntness of the absorption edge. The latter stays within experimental error limits (a few nm) at the same wavelength. The trend is the same for all the produced LTG-GaAs samples. These results show that for the preparation conditions of our samples, the growth under low temperature and the subsequent annealing leaves the structure of the samples in the same state as the structure of the normal grown semiconductor. No absorption features are observed in the wavelength vicinity of the band gap, giving the

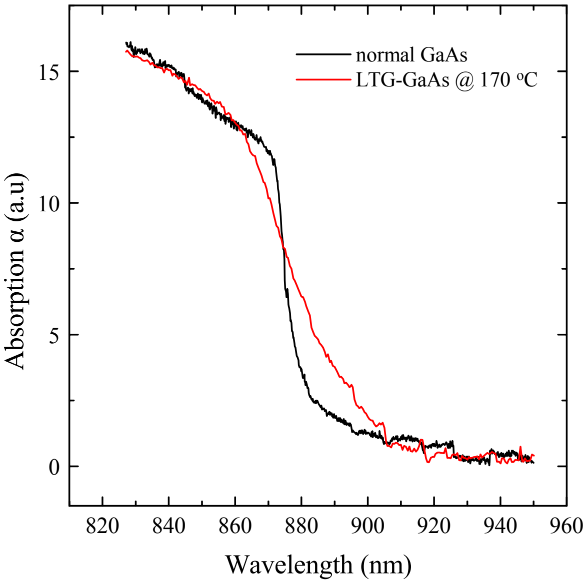

**Figure 4-13** The linear absorption spectrum of normal grown GaAs (black line) at the wavelength region we are interested. The red line shows the absorption spectrum of an LTG-GaAs sample grown at 170 °C and annealed at 600 °C for 20 min.

conclusion that any optically active defects that might contribute to our measurements are absent in all our samples.

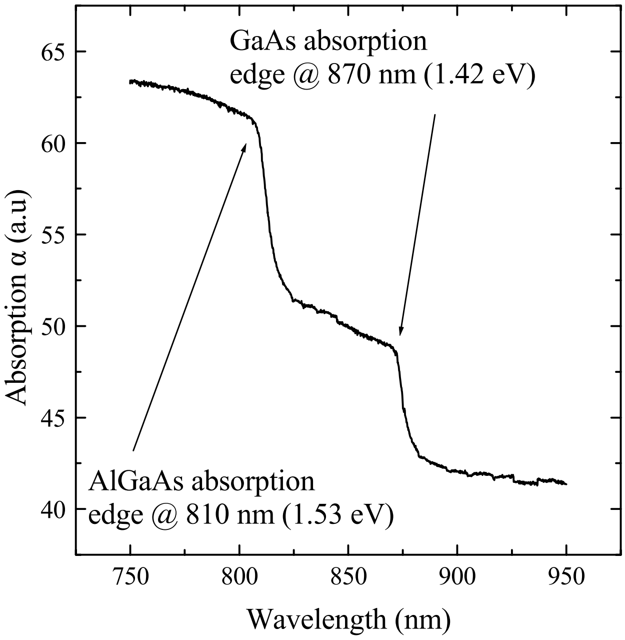

**Figure 4-14** Absorption spectrum from an AlGaAs sample where the GaAs substrate is not completely etched away. In this way, we can obtain the bandgap energy of our AlGaAs samples.

Optical characterization is crucial in order to establish the band gap energy of our LTG-AlGaAs samples. In the case of AlGaAs, the fraction of Al in the alloy is difficult to control with high accuracy. During growth, the percentage of the Al in the AlGaAs alloy can be controlled with an accuracy of a few %. The samples are grown so that the Al mole fraction does not exceed 10 %. However, we are not able to know the exact percentage. Therefore, optical characterization is crucial, in contrast to GaAs, whose optical properties are well established in the literature.

**Fig. 4-14** shows an absorption spectrum for one of our AlGaAs samples. These samples are prepared in such a way so that epilayers of AlGaAs and GaAs coexist. That is, the GaAs substrate is not completely etched away. So, in such samples, there is a GaAs substrate of a few μm thick and on top there is the LTG-AlGaAs epilayer. In this way, the obtained transmission spectra contain information from both the remainder GaAs substrate and the LTG-AlGaAs epilayer, allowing us to obtain unambiguous results about the band gap of AlGaAs and to compare it with the GaAs value which is well established in the literature. The AlGaAs band gap, as can be seen in **Fig. 4-14** is measured to be 810 nm (1.53 eV). Allali et al. **Allali** have given an expression connecting the Al fraction with the band gap energy of AlGaAs alloys (Eq. 3-2):

$$E_g(x) = E_g(0) + 1.29x - 0.15x^2$$

for T=300 $^o$K and for 0<x<0.4 (see **Chap. 3**). Using their formula and the measured band gap energy for our samples we obtain a value for the Al fraction 8 % which is in good agreement with the projected Al fraction from the growth conditions in the MBE chamber, taking into account the experimental growth error of a few percent. All the AlGaAs samples have the same absorption spectrum and the same band gap energy, thus establishing the Al fraction in all our samples at 8 %. Moreover, optical characterization of the etched samples helps in obtaining transient optical spectra from areas of the samples that contain only LTG-AlGaAs. This way, we are able to ensure that possible remainders of the GaAs substrate do not distort our measurements and results.

## 4.4 Experimental results

The laser system used for the measurements of the LTG-GaAs and LTG-AlGaAs samples is the Tsunami laser system described in **Chap. 2**. The technique used in order to reveal the electron dynamics of LTG-GaAs is a standard pump probe technique and the experimental arrangement is shown in **Fig. 2-10**. An intense pump pulse tuned close and above the band gap, excites at time $t = 0$ a population of electrons from the valence to the conduction band. The most convenient definition of time t=0 in this case should be the moment that coincides with the peak intensity of the pump pulse or the pump-probe pulses cross-correlation (CC) that is assumed to have an instantaneous time response. For the LTG-GaAs measurements, the wavelength is kept at 860 nm

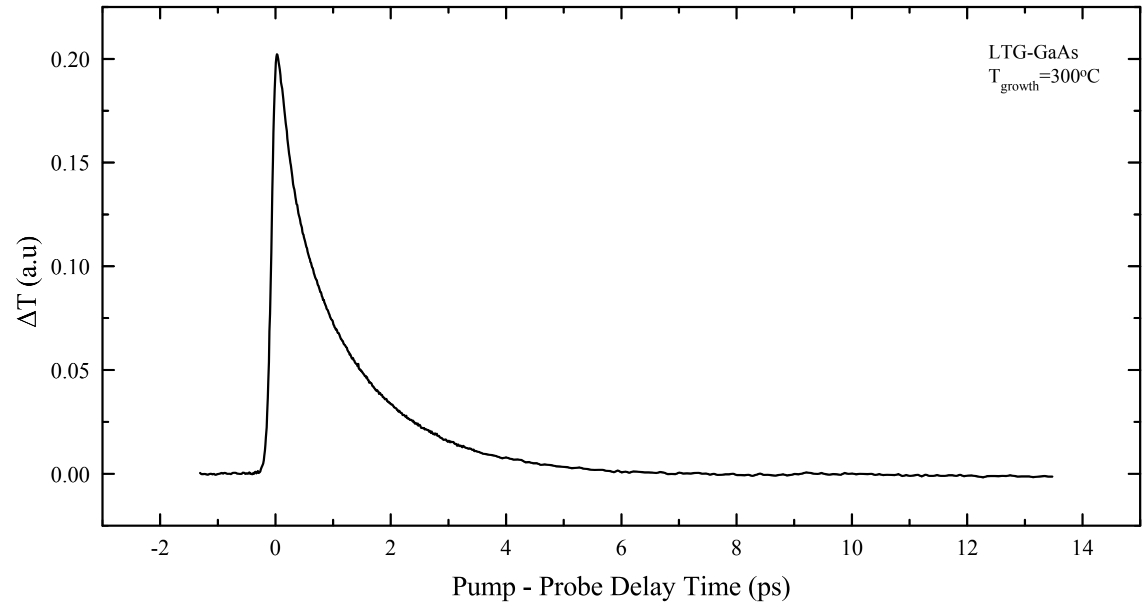

**Figure 4-15** Pump-probe transient transmission spectrum of LTG-GaAs. The signal abruptly rises to a maximum and "slowly" decays to its initial background value.

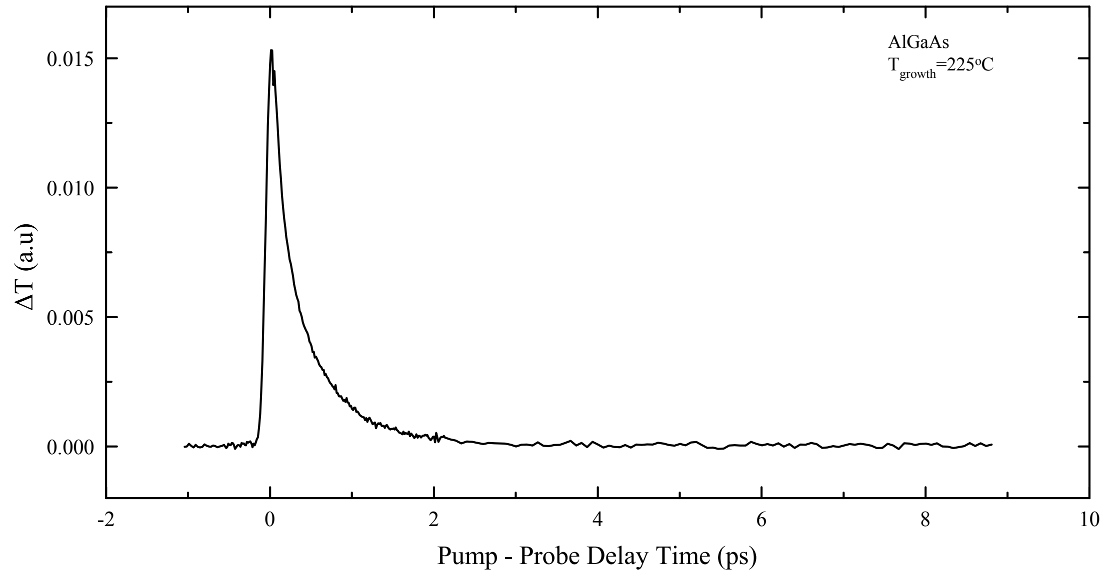

**Figure 4-16** A typical transient transmission spectrum for an LTG-AlGaAs sample. The behaviour is similar to LTG-GaAs.

(1.44 eV) which is less than 20 meV above the room-temperature band gap of crystalline GaAs (1.42 eV), in order to minimize carrier-cooling effects (carrier-lattice thermalization). For the LTG-AlGaAs measurements, the wavelength is kept at 800 nm (1.55 eV) for the same reason~~s~~. A typical laser pulse duration is approximately 100 fs. The pump and probe beams had the same wavelength and are orthogonally polarized so as to avoid any coherent artifact contributions in the signal, which is measured by a standard lock-in detection technique, as shown in **Chap. 2**. The excitation density had an upper limit of about $2\times10^{17}$ cm$^{-3}$ which lies in the moderate excitation density regime.[Siegner, Sosnowski] The latter value is calculated using the value $a$=8000 cm$^{-1}$ for the absorption coefficient.[Blakemore] The excitation density is kept constant and low enough in order to avoid saturation and bottleneck phenomena associated with trap filling.[Siegner, Sosnowski]

A typical measurement for a LTG-GaAs sample is shown in **Fig. 4-15**. The experimental data are the black square points. A typical measurement for a LTG-AlGaAs sample is shown in **Fig. 4-16**. As in the LTG-GaAs case, the signal first exhibits a fast rise to a maximum value and then slowly decays to its background value. This transient behavior of the signal can be explained with a bandfilling[Benjamin] effect as it is visualized in **Fig. 4-17**. At time $t<0$, i.e. when the system is still unperturbed and in equilibrium, no electrons are found in the conduction band. Therefore interband absorption by the probe beam has the maximum efficiency. The probe beam suffers the maximum absorption and therefore the signal in **Fig. 4-15** (**Fig. 4-16**), which is the transmission of the probe beam is minimized (set to zero). At time $t=0$ (**Fig. 4-17b**) the pump beam excites a population of electrons in the conduction band. In this case, the probe beam that “tries” to excite electrons to the conduction band, finds it harder since a lot of the available states in the vicinity of the conduction band bottom are already occupied. Therefore, the probe beam passes through the sample suffering less absorption and therefore the signal in **Fig. 4-15** (**Fig. 4-16**) at time $t=0$ is maximum. At times $t>0$ (**Fig. 4-17c**) the pump beam fades away or is already finished and the electron population starts

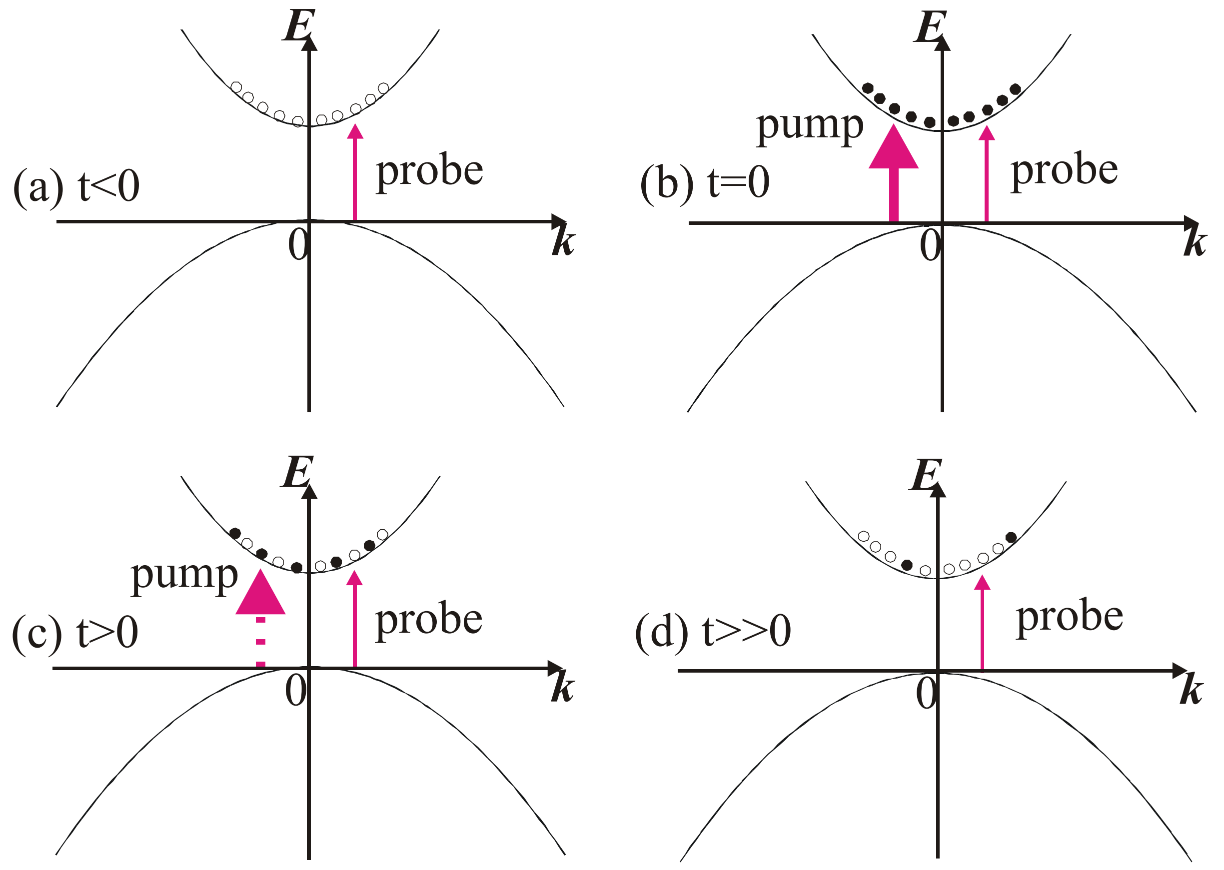

**Figure 4-17** (a) Before perturbation by the pump. The probe beam is "easily" absorbed. (b) The pump has just created free electrons. The probe is "hardly" absorbed. (c) The pump vanishes and the free carrier population decays. (d) Most of the electron population has decayed and the probe is again "easily" absorbed.

to decay with various mechanisms as mentioned in **Chap. 3**. Therefore there is an opening of some available states in the conduction band and the probe beam starts again to suffer some absorption by the material. So, the probe transmission reduces and so does the signal in **Fig. 4-15** (**Fig. 4-16**) at positive time delays, right to the peak. At times t>>0 (**Fig. 4-17d**) the electron population has decayed so much that there are very few (if not any) electrons in the conduction band at the laser spot area. So, the probe beam suffers progressively bigger absorption and therefore the signal in **Fig. 4-15** (**Fig. 4-16**) "slowly" returns back to the background value, the same as before the excitation by the pump beam (negative time delays).

For the description of the signal behavior we utilize a phenomenological model. In a first approach we try to describe the evolution of the electron population with:

$$\frac{dn}{dt} = -\frac{n}{\tau} \tag{4-1}$$

where $n$ is the electron concentration, which gives a solution

$$n(t) = n_0 e^{-\frac{t}{\tau}} \tag{4-2}$$

where $n_0$ is the concentration at time $t$=0. Now, this response function of the system corresponds to the function *f(t)* as it is mentioned in the signal analysis in **Chap. 2 (Eq. 2-4**). We also consider the transmission of the probe beam *T(t)* to linearly depend on the electron concentration, which is valid for a small perturbation. So, this function (*T(t)*) convoluted with the cross-correlation (CC) of the pump and probe pulses will give a signal of the form (see also **Eq. 2-6**):

$$Signal(t) = \int_{-\infty}^{+\infty} CC(t-t')T(t')dt' \tag{4-3}$$

where $CC(t) \sim e^{-\frac{t^2}{2w^2}}$; the parameter $w$ is associated with the FWHM of the CC curve (**Eq. 2-18**) or the laser pulse duration, and $T_c(t) \sim \Theta(t)e^{-ct}$, with $c = \frac{1}{\tau}$. So:

$$Signal(t) \sim \int_0^{+\infty} e^{-\frac{(t-t')^2}{2w^2} - ct'} dt'$$

or:

$$Signal_c(t) \sim e^{-ct} \int_0^{+\infty} e^{-\frac{1}{2w^2}\left(t - w^2 c - t'\right)^2} dt'$$

With a change of variables we can get:

$$Signal_c(t) \sim e^{-ct} \int_{\frac{t-w^2c}{\sqrt{2}w}}^{-\infty} e^{-\tau^2}\, d\tau$$

Now, using the definition of the Error function:

$$Erf(t) \equiv \frac{2}{\sqrt{\pi}} \int_0^t e^{-\tau^2}\, d\tau$$

and the known formula: $\int_{-\infty}^{+\infty} e^{-x^2}\, dx = \sqrt{\pi}$, we can finally get:

$$Signal_c(t) \sim e^{-ct}\left[1 + Erf\left(\frac{t - w^2 c}{\sqrt{2}w}\right)\right] \qquad \textit{(4-4)}$$

So, the next step is to try to fit the experimentally obtained data as the one shown in **Fig. 4-15** (**Fig. 4-16**) with the last formula. We can see that only three parameters are free for the fitting procedure: the constant *w*, the constant of proportionality of the *Signal(t)* with the error function and the most important, the characteristic decay time $\tau = \frac{1}{c}$. In most cases, for the fitting procedure to be more efficient, we experimentally determine the parameter *w*, by separately obtaining a CC curve of the pump and probe pulses under exactly the same experimental conditions as the measurements of the transient transmission spectrum of the semiconductor as in **Fig. 4-15** (**Fig. 4-16**). In **Fig. 4-18** the reader can find the results of this fitting attempt. As it is obvious, this attempt is rather unsuccessful. The decay of the fitting function cannot quite well describe the decay of the experimental curve, thus resulting in a characteristic time constant that is not very reliable. In a closer look, in the inset of **Fig. 4-18**, it can be seen that the fitting problem starts from the early dynamics of the signal: even the rise of the signal cannot be adequately described by the fitting function, thus resulting in a peak shift and at longer time delays in a deviation from the data. Thus

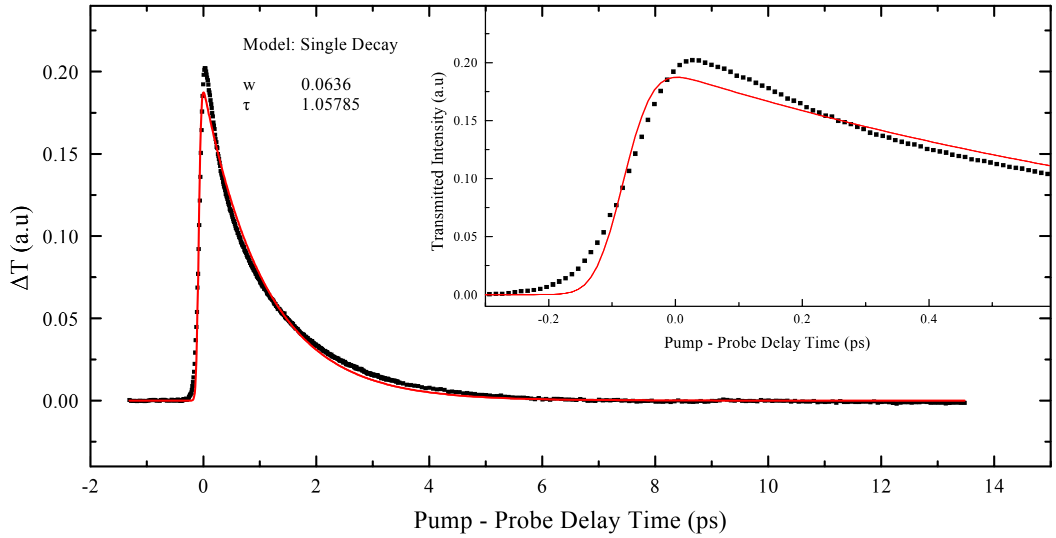

**Figure 4-18** The result of the phenomenological model taking into account only one decay mechanism cannot adequately describe the signal evolution. Inset shows the problem from the early stages.

we conclude that we must readapt our phenomenological model and to take into account a possible phenomenon that influences the very early stages of the signal and results in a modification of its rise.

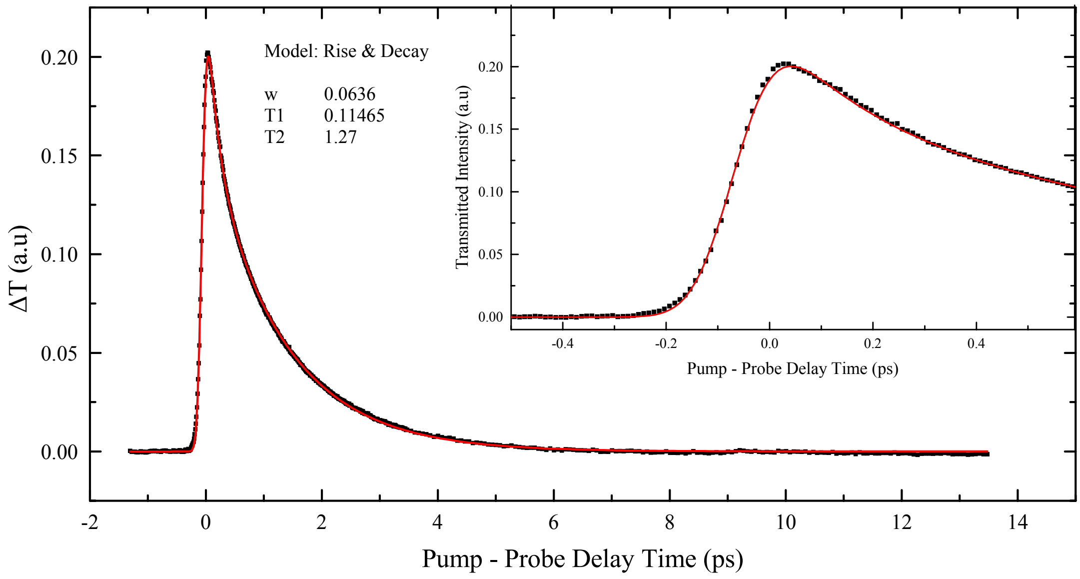

**Figure 4-19** The phenomenological description can adequately describe the signal only if we take into account the delayed rise as well. Inset shows the good reproduction of the data from the early stages.

Thus, now, apart from the decay of the phenomenological model that describes the decay of the electron population we now attempt to insert a certain deposit that acts additively to the electron population. The phenomenological model then becomes:

$$\begin{aligned} \frac{dn_1}{dt} &= -\alpha n_1 \\ \frac{\partial n_2}{\partial t} &= +\alpha n_1 - \beta n_2 \end{aligned} \tag{4-5}$$

where $n_1$ is the new deposit that is initially created by the pump pulse and that decays only to our familiar electron deposit $n_2$ with a rate $\alpha$. The old deposit $n_2$ decays with the characteristic rate $\beta = \frac{1}{\tau}$. With the mentioned conditions, the solution of the above coupled system of differential equations becomes:

$$\begin{aligned} n_1(t) &\propto e^{-\alpha t} \\ n_2(t) &\propto \left(e^{-\beta t} - e^{-\alpha t}\right) \end{aligned} \tag{4-6}$$

and we assume that the transmission of the probe beam is a linear combination of the two distinct electron populations $n_1$ and $n_2$:

$$\begin{aligned} T(t) &= An_1(t) + Bn_2(t) \Rightarrow \\ T(t) &= Ae^{-\beta t} + Be^{-\alpha t} \end{aligned} \tag{4-7}$$

thus resulting to a signal function of the form:

$$Signal(t) = Ae^{-\beta t}\left[1 + Erf\left(\frac{t - w^2\beta}{\sqrt{2}w}\right)\right] + Be^{-\alpha t}\left\{1 + Erf\left[\frac{t - w^2\alpha}{\sqrt{2}w}\right]\right\} \tag{4-8}$$

A fitting of the same experimental data with this last function and with the same procedure is shown in **Fig. 4-19**. Thus we conclude from this phenomenological analysis there are two decay mechanisms that contribute to the signal, one in the very early stages and the rise of the signal that is unavoidably convoluted with the laser pulse, and one that dominates the last stages and the decay of the signal.

In order to study the early electronic behavior of the samples, one must limit the time window of the measurements to small values, like the measurement presented in **Fig. 4-20**. The pulse CC is also shown. As can be easily seen, there is a time shift between the peak of the pump-probe CC and the peak of the transient transmission of the sample. This can be explained as follows: all the energy of the pump pulse is instantaneously stored at a non-equilibrium population of electrons that does not follow a Fermi-Dirac energy distribution. This distribution evolves to a thermalized one, which follows the Fermi-Dirac law. This evolution happens through carrier-carrier interactions, as discussed in **Chap. 3**. The time scale of this process lies in the order of several tenths of fs. As shown in **Fig. 4-20**, the signal rises slower than the CC of the pump and probe pulses. Also, the maximum intensity of the signal is positively shifted in time relatively to the peak of the CC of the

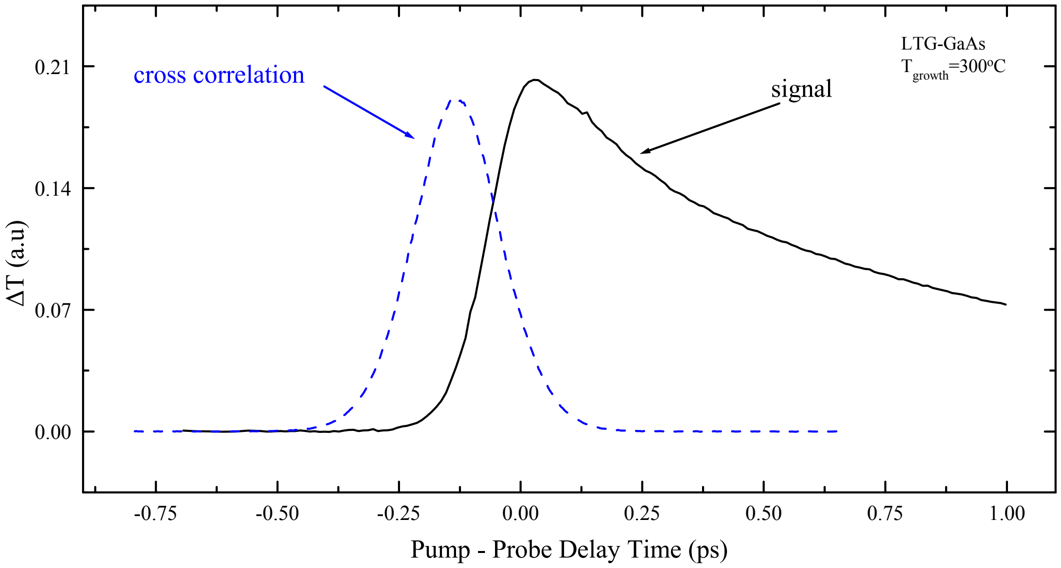

**Figure 4-20** Transient transmission spectrum obtained within a short time window. The peak of the signal does not coincide with the "instant" of the perturbation.

pump and probe pulses. These two facts are the observed result of the noninstantaneous thermalization of the hot electron population i.e. the delayed evolution towards a Fermi-Dirac thermalized electron energy distribution. This delayed thermalization contributes not only to the shifted peak of the signal but to the rise and decay of the signal as well. The time scale of this mechanism is in the order of 100 fs as established in the literature for normal grown ($T_{growth}$ ~ 600 $^oC$) GaAs. **Marcinkevicius2, Lin** Typical transient spectra of LTG-GaAs and LTG-AlGaAs samples for rather short time windows limited to few ps are shown in **Fig. 4-21** and **Fig. 4-22** respectively. The CC of the pump and probe laser beams is also shown for comparison, as taken under exactly the same experimental conditions using a Barium Borate Oxide (BBO) crystal in the place of the samples. As can be seen in **Fig. 4-21** and **Fig. 4-22**, LTG-GaAs and LTG-AlGaAs exhibit a delayed rise and a time shifted peak with respect to the CC curve. The characteristic times for this mechanism that are extracted for both LTG-GaAs and LTG-AlGaAs samples using the previous phenomenological description lie in the vicinity of 100 fs with a dispersion of 10-20 fs. This value

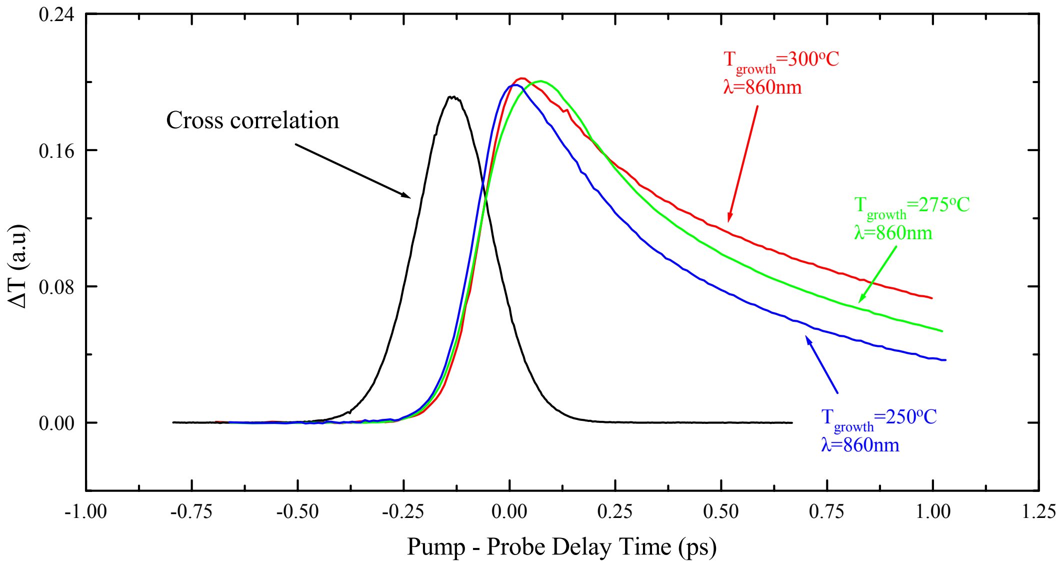

**Figure 4-21** Typical short-scale transient spectra for three different LTG-GaAs epilayers. The trend for the thermalization times is similar to all samples.

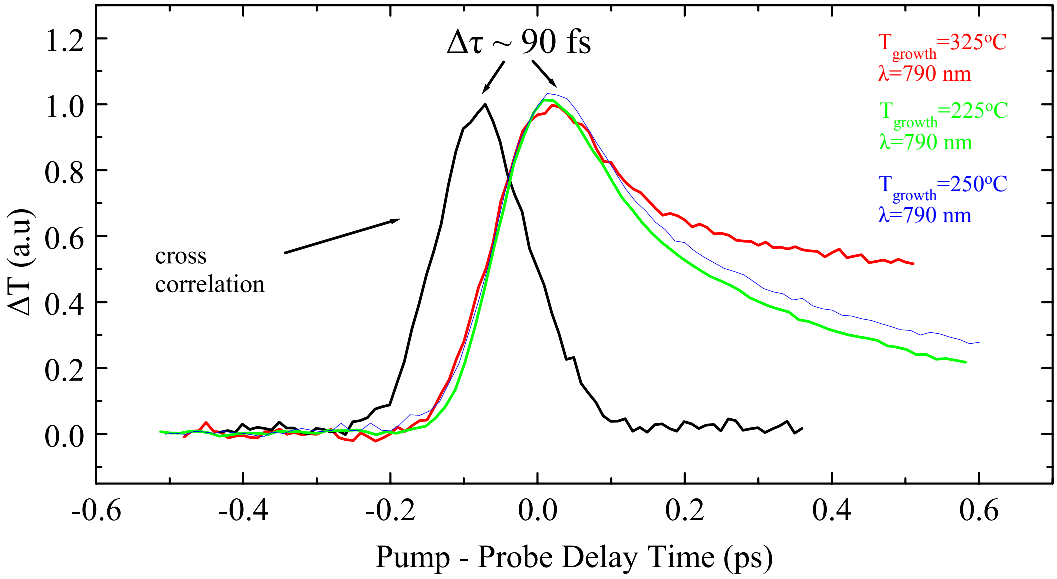

**Figure 4-22** Short scale transient spectra for various LTG-AlGaAs epilayers. Like in LTG-GaAs, the signal exhibits the same behaviour for the early stages for all samples.

agrees with the values reported for the electron thermalization times for normal grown GaAs that are already reported in the literature. **Marcinkevicius2, Lin** Lin et al. **Lin** have established a dependence of the electron thermalization times on the Al mole fraction. No observable deviation of the thermalization times of AlGaAs to those of GaAs has been found, probably due to the low mole fraction of Al in our AlGaAs epilayers (~8 %). Furthermore, no specific trend is observed for the thermalization times with respect to the As precipitate characteristics i.e. density and size implying that the latter have no effect on the electron thermalization times. On the other hand, the limited time resolution of our experimental setup (~ 100 fs) prevents us from deducing unambiguous results for any possible trend of the thermalization times in LTG-GaAs and LTG-AlGaAs with respect to the As precipitate size and spacing or the Al mole fraction.

After the initial electron population internal thermalization the signal decays to the initial background value. All the decay processes contribute to the signal decay as this is shown in **Fig. 4-15** and **Fig.4-16**. To evaluate the function that describes the decay of the signal we try to make logarithmic plots of the signal. Typical results are shown in **Fig. 4-23**. From these plots it is evident that the signal exhibits a single-exponential decay behavior in time windows after about 0.5 ps from the peak of the signal. This implies that the electron population is subject to only one decay mechanism after the excitation. By fitting the decay of the signal either with a single exponential function in plots like **Fig. 4-15** (**Fig. 4-16**) or by linear functions in plots like in **Fig. 4-23**, we are able to obtain the characteristic decay times of the signal that represent the decay of the electron population. Notice that, the fitting to the decay of the signal is performed to points at least 0.5 ps after the peak of the signal in order to make sure that at this time window there are no contributions from either the convolution of the signal with the pump-probe CC or the rise of the signal due to thermalization of the initial carrier population. Also, this single-exponential behavior is consistent with the signal function that is obtained using the previously mentioned phenomenological model (**Eq. 4-8**), since the function *Signal(t)* is very well approximated by an exponential $Signal(t) \propto e^{-\frac{t}{\tau}}$ for sufficiently long delay times.

A similar procedure is followed to study the decay of the signal for the LTG-AlGaAs samples as well. As can be seen in **Fig. 4-24**, the decay is single exponential after about 0.5 ps from the peak, implying that there is only one channel of decay. By fitting this decay with a single exponential, the characteristic time can be obtained. As in the case of LTG-GaAs, the fitting to the decay of the signal is performed to points at least 0.5 ps after the peak of the signal in order to make sure that in this time window there are no contributions from either the convolution of the signal with the pump-probe CC or the rise of the signal due to thermalization of the initial carrier population. The pumping and the probing wavelengths are always kept at the most 30 meV above the bottom of the conduction band. This way, the contribution to the signal of the electron decay towards the bottom of the conduction band via electron – phonon interactions is minimized. This

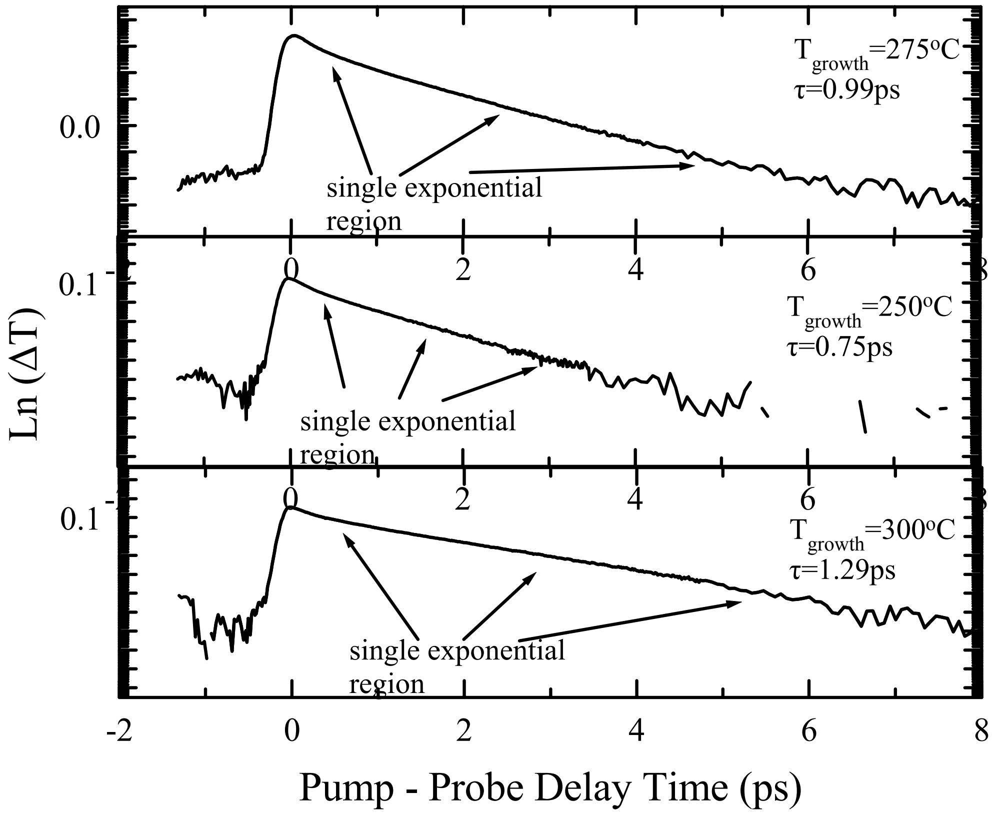

**Figure 4-23** Logarithmic plots of extended transient spectra for three LTG-GaAs epilayers. These plots are used to evaluate the signal decay function.

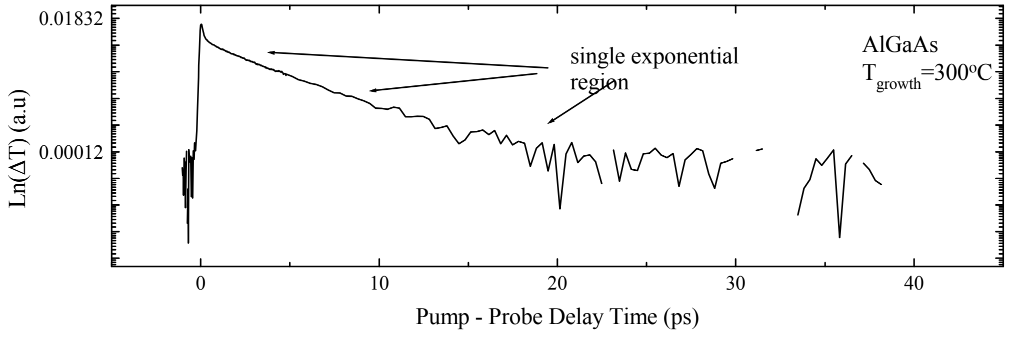

**Figure 4-24** Ln-linear plot of the signal for an LTG-AlGaAs epilayer.

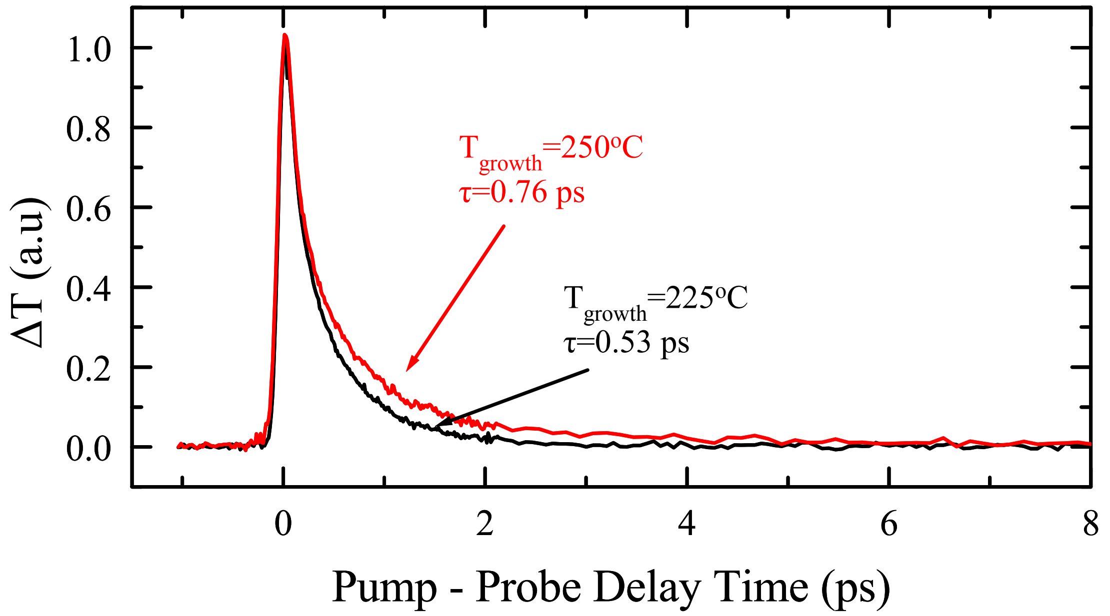

**Figure 4-25** Transient transmission spectra for two LTG-AlGaAs samples grown at 250 °C and 225 °C.

decay rate can either be obtained by an exponential fitting in **Fig. 4-15** or a linear fitting in **Fig. 4-24**. Typical transient transmission spectra obtained for LTG-AlGaAs samples are shown in **Figs. 4-25** and **4-26**. The pump and the probe wavelengths are at 790 nm or 1.57 eV which is about 40 meV above the band gap.

Aluminum (Al) is a material that suffers oxidation under atmospheric conditions. Therefore, in room conditions where the experiment is being carried out, the suspicion of corruption of the measurements due to oxidation of the Al part of the semiconductor is justified. To resolve this matter, an AlGaAs sample grown at 250 °C with a cup-layer of GaAs that prevents the oxidation of Al is also grown. The transient spectra obtained for this sample are compared with the transient spectra obtained for the corresponding AlGaAs sample grown at 250 °C which does not have a GaAs cup-layer. The results are shown in **Fig. 4-27**. As can be seen, there is no observable difference in the ultrafast electronic response of these samples, which suggests that no oxidation has occurred, or it is low enough to have negligible contribution to our measurements.

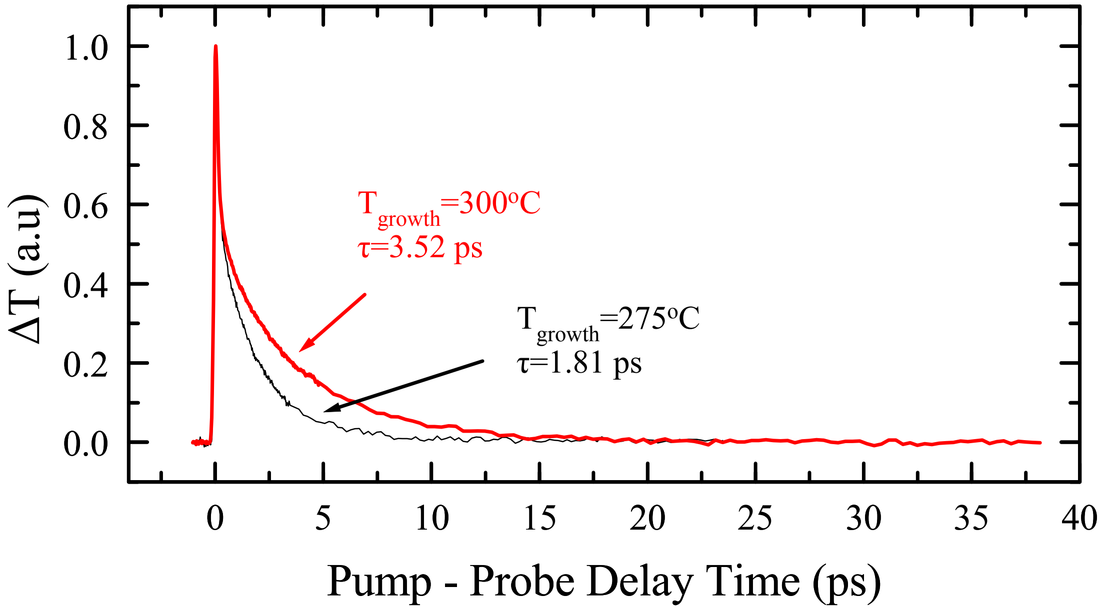

**Figure 4-26** Transient spectra for two different growth temperatures of AlGaAs.

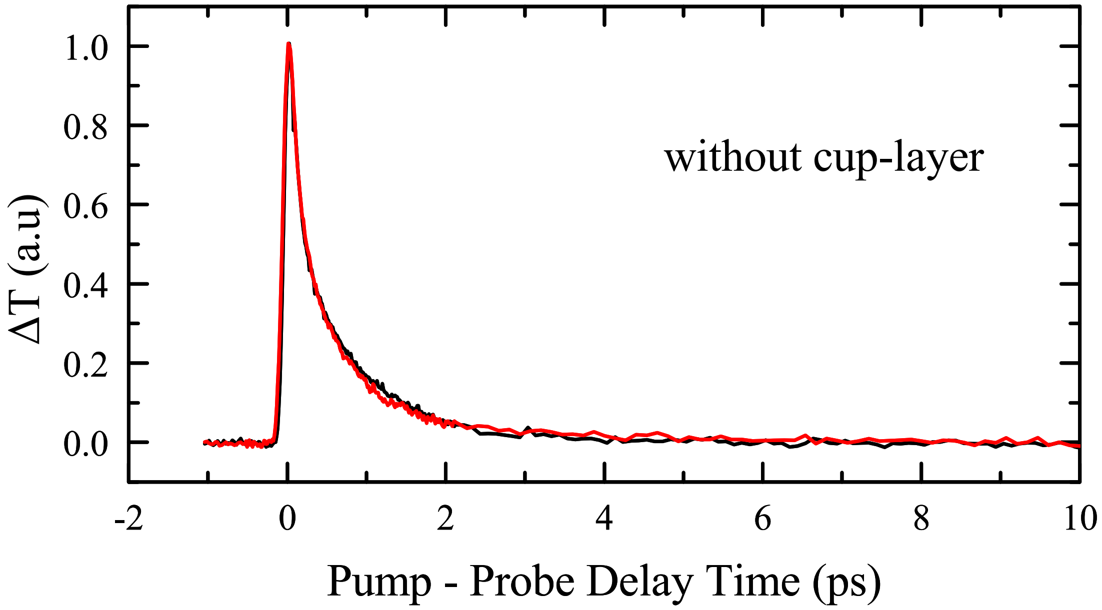

**Figure 4-27** Transient spectra obtained for two AlGaAs samples grown at the same temperature, one of them having an extra GaAs cup-layer. The behavior is the same.

## 4.5 Discussion

The results of the electron trapping times with respect to the growth temperature are summarized in **Fig. 4–28** and **Fig. 4-29** for LTG-GaAs and LTG-AlGaAs respectively. The general trend that is observed for both cases is that the higher the growth temperature, the higher the characteristic signal decay time. The dependence is superlinear and there appears to be a “jump” or a high nonlinearity at the higher presented temperatures, when we approach the normal growth temperature of the materials. A discussion will follow in order to associate this observed trend with the mechanisms that are involved in the electron dynamics in the semiconductors.

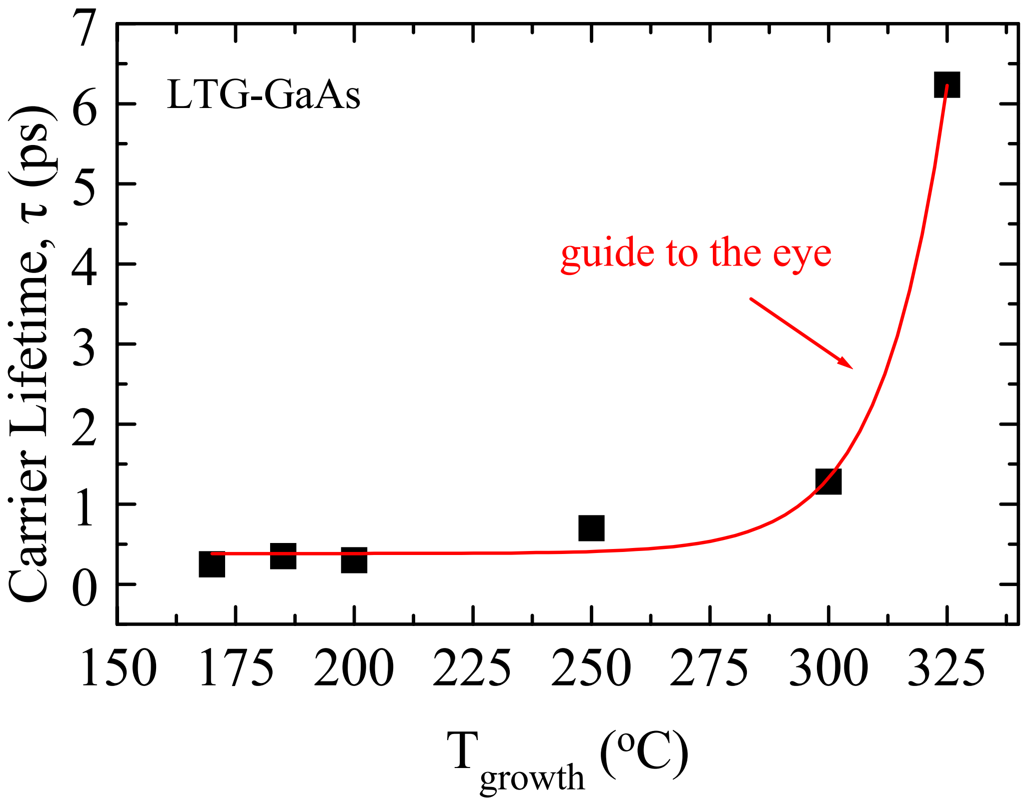

**Figure 4-28** The observed decay times with respect to the growth temperature for GaAs.

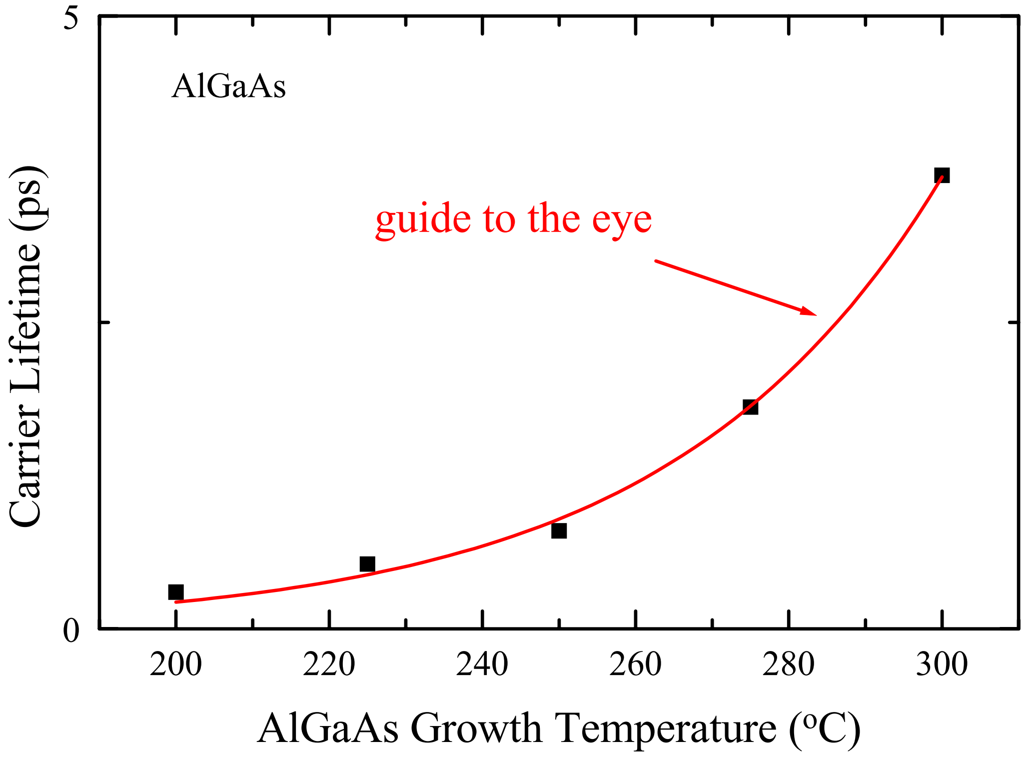

**Figure 4-29** The observed decay times with respect to the growth temperature for AlGaAs.

The thermalized distribution loses energy through various mechanisms. Carrier-optical phonon interaction is responsible for carrier intravalley relaxation towards the bottom of the conduction band, as shown in **Fig. 3-13**, and is the dominating process for electrons excited high in the conduction band. However, because in our experiments the electrons are excited near the bottom of the conduction band and have an excess energy in the vicinity of 20-40 meV which is less, or at most, equal to the energy quantum of one phonon, this process can be considered to be negligible if not completely absent in both the LTG-GaAs and the LTG-AlGaAs cases.

Another way of relaxation is the interaction of the carriers with large wave-vector phonons where the electrons are scattered from the central valley of the Brillouin zone towards side valleys, a process called intervalley scattering, which is shown in **Fig. 3-14**. Again, we consider this process to negligibly affect our measurements because the excess energy of the laser excited electrons is much less than the value of 290 meV which corresponds to the transition energy difference from the bottom of the Γ-point to the bottom of the L-point of the conduction band of GaAs.

From the bottom of the conduction band the electrons can relax to the valence band through radiative emission or via three-body Auger interaction, as shown in **Fig 3-15** and **Fig. 3-17**. Both of the last two processes take place in a time scale that is of the order of 100 ps or much greater **Othonos** and therefore can be considered to have a negligible contribution to the ultrafast processes that we are interested in. In other words, none of the above mechanisms can describe the ultrafast decay of the signal (like in **Fig. 4-15** and **4-16** ) that we observe in all the measurements of our samples.

Thus, the only way to describe the decay behavior of the signal in our measurements is the real-space kinetics (diffusion) of the carriers and the association with the presence of the defects (As precipitates) in our crystals. In order to deconvolve the influence of the As precipitates with the kinetic behavior of the carriers we first investigate the transient behavior of samples that are grown under normal conditions. Such samples, either GaAs or AlGaAs, are usually grown at 600 $^{o}$C, and the material is stoichiometric, i.e. there is no observable excess As in the semiconductor host. The normal material contains the lowest possible amount of defects-traps. A typical transient transmission spectrum of such a sample (GaAs) is shown in **Fig. 4-30**. As seen, the decay of the signal is very slow compared to the one obtained for LTG-GaAs (**Fig. 4-15**). The characteristic decay time is very difficult to evaluate with a good accuracy and is estimated to be around 40 ps, as mentioned in **Chap. 3**. A similar case for the AlGaAs is shown in **Fig. 4-31**. Here, the decay time is much bigger and the limiting time window of about 150 ps leads us to a rough estimation of $\tau$>100 ps. So, in both GaAs and AlGaAs grown under normal conditions where the only relaxation mechanism of the carriers is real-space kinetics (diffusion) and interaction with the lowest possible amount of traps (absence of As precipitates) the decay of the signal occurs in a time scale in the order of around 50 ps or much higher. Therefore, the much shorter ultrafast signal behavior for the

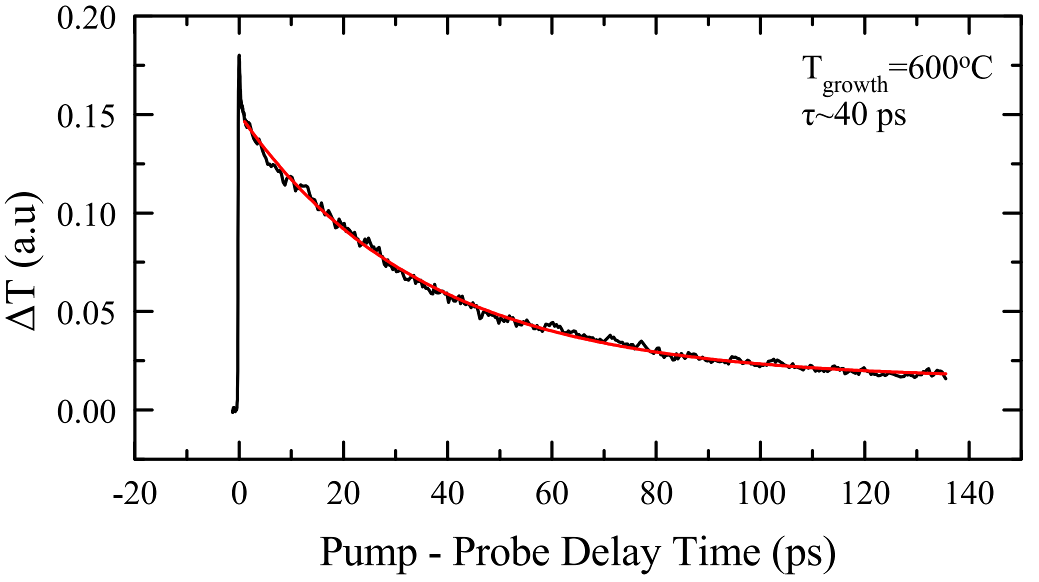

**Figure 4-30** Signal decay for "normal" grown GaAs.

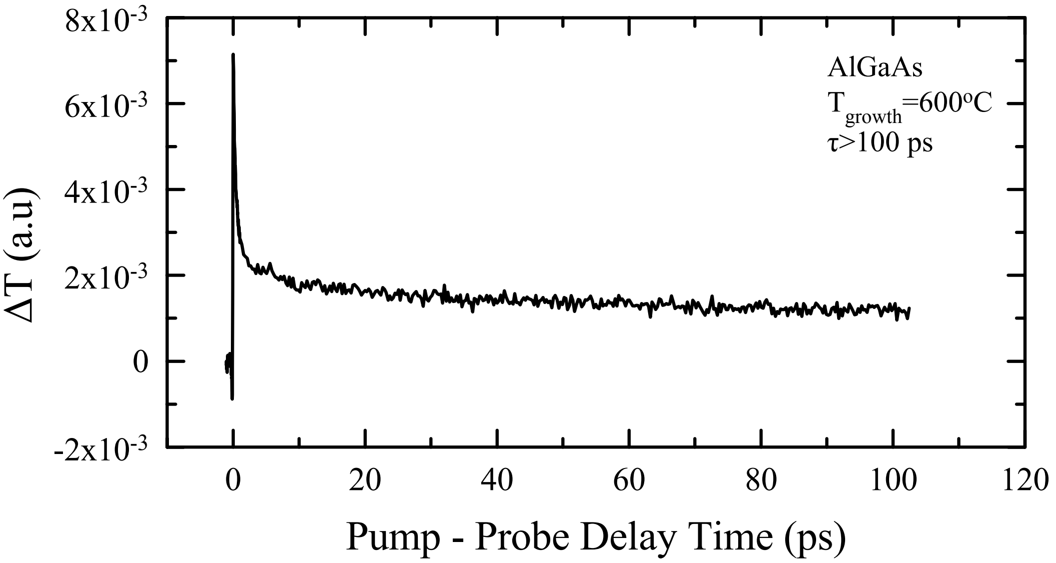

**Figure 4-31** Transient spectrum for "normal" grown AlGaAs.

LTG material as shown in **Fig. 4-15** and **Fig. 4-16** can only be attributed to the presence of the As precipitates. In the discussion to follow, we investigate the exact mechanism with which the excess As influences the ultrafast behavior of the generated electrons.

Two models exist to interpret the semi-insulating (and therefore the associated ultrafast electronic) behavior of LTG-GaAs. The first one, presented by Look et al., [Look] is based on the traps or near midgap states that are formed due to the introduction of excess As in the lattice of GaAs. This excess As is present mainly in the form of $As_{Ga}$ antisites. Other defects such as Ga vacancies are not excluded. These defects introduce energy states near the middle of the band gap. Because of the rather big density of these defects, the midgap energy states may be referred to as a continuum of states rather than discrete levels. However, because of the rather strong thermal treatment of our samples we will not consider this case as the As point defect concentration in our samples can easily be considered to be negligible if not absent. [Melloch]

The second model, introduced by Warren and co-workers, [Warren, Warren2] takes into account the formation of As precipitates. Under the assumptions of this model, the excess As defects are randomly embedded in the semiconductor host. After the thermal treatment (annealing) of the semiconductor, the excess As is found in the form of precipitates or clusters. These precipitates are metallic clusters of crystalline structure. These clusters act as buried Schottky barriers and the interfaces between these clusters and the bulk semiconductor are to be treated as metal-semiconductor contacts. Moreover, in most cases the barrier formation is independent of the type of metal and the doping level of the semiconductor. [Warren, Tersoff] If the annealing conditions are strong enough, then an extended region between the surface of the As precipitates and the bulk GaAs is depleted of carriers and is called the depletion region exactly as it happens in a metal-semiconductor contact. Given the proposal of this model for the semi-insulating behavior of LTG-GaAs, the ultrafast signal decay exhibited by such materials has been attributed to the (accidental)

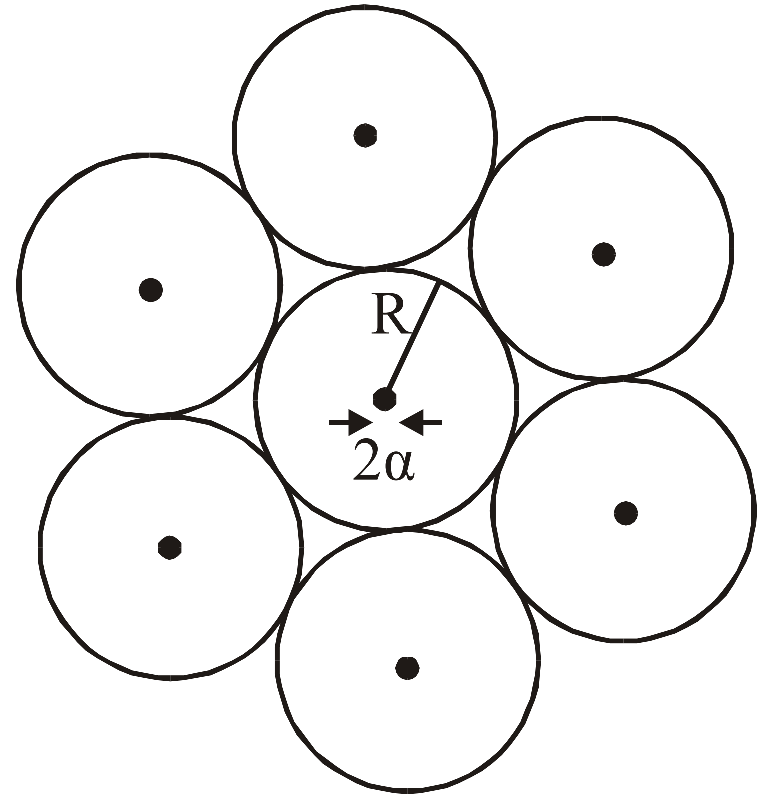

**Figure 4-32** The As precipitates are assumed to form a lattice. The unit cell has one As precipitate in the center. The cell radius is *R*.

capture of electrons (and holes) by the As precipitates. **Schaff, Harmon, Melloch, Lochtefeld, Melloch3** Electrons moving in a random way out of the initial laser-illuminated region, are trapped on the surface of the As precipitates that are found in the electron path. In the discussion to follow, the single exponential behavior observed in our samples for the signal decay rate is thus associated to the above electron trapping mechanism.

Given the results from the structure characterization of the samples one has to evaluate the data obtained for the characteristic electron trapping times with regard to the sample internal structure parameters. These are the As precipitate average spacing and size (radius). The average As precipitate spacing *R* is connected with the average density *n* with the relation:

$$n = \frac{1}{\frac{4\pi}{3} R^3} \qquad (4\text{-}9)$$

This simple formula is deduced assuming a lattice of As precipitates inside the semiconductor host that consists of unit cells that contain one As precipitate on average in the center and with an average radius *R*, **Ruda** as shown in **Fig. 4-32**.

We first attempt to interpret our data through the classical scattering model. Under the assumptions of this model, electrons moving in a straightforward manner, accidentally meet the target which in our case is the As precipitate and get trapped. A visualization is shown in **Fig. 4-33**. In this figure the electrons move in one dimension for simplification but the results given for the three dimensional case are the same. This model predicts that the electron scattering time should be:

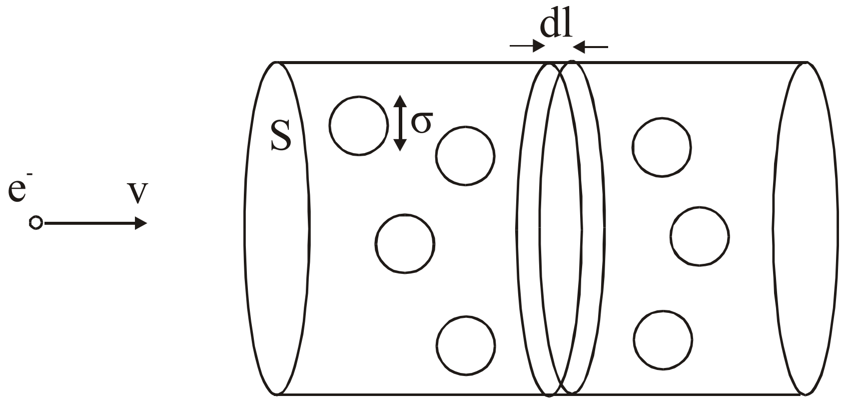

**Figure 4-33** Electrons moving straightforwardly scatter (or get trapped) by the targets (As precipitates) with cross-section $\sigma$.

$$\tau = \frac{1}{n_e \sigma v} \tag{4-10}$$

where $n_e$ is the electron concentration, $\sigma$ the scattering cross section and $v$ the electron velocity that is taken to be the electron thermal velocity for the case that the electrons are excited to levels at or near the bottom of the conduction band. In **Fig. 4-34** it is evident that the electron trapping times for LTG-GaAs do not follow the quantity $\frac{1}{n\sigma}$ (or its analogue

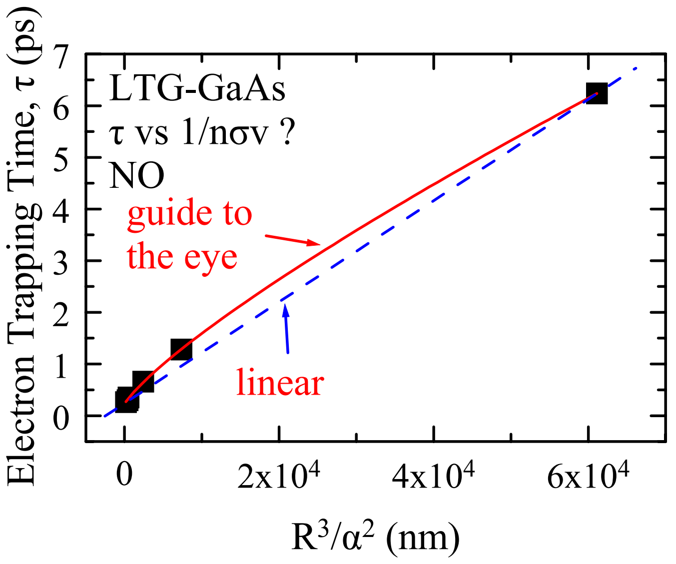

**Figure 4-34** The observed deacy rates versus the quantity $\frac{1}{n\sigma}$ or equivalently $\frac{R^3}{\alpha^2}$. The solid line is a guide to the eye. The decay mechanism cannot be explained by the classical scattering model adapted to out case.

$\frac{R^3}{\alpha^2}$). Melloch et al. **Melloch2, Prabhu** have also attempted to explain their data for the electron trapping times with the same model and have made similar observations to ours that this model cannot describe the electron trapping mechanism. According to this argument, this model describes a system of traps capable of capturing only one electron at a time. After the capture of a carrier the trap is assumed to be neutralized. They further propose that terms of the above model for every ionization level of the traps should be introduced in order to account for traps that can be multiply ionized. Additionally to this argument, the failure of this electron trapping model to describe the observed trend implies that the electron motion cannot be considered as ballistic as this model suggests. In the simple ballistic case above, the electrons moving in a straightforward manner have a certain probability of impact (and trapping) with a defect, in our case the As precipitate. The failure of this model to accommodate the trend of the data suggests that the above assumptions are not valid.

In order to overcome this difficulty Melloch et al. **Melloch2** suggested that the mechanism that could better describe electron trapping should be considered as a diffusive transport and impact on the As precipitates. They observed a superlinear dependence of the electron trapping times on the As precipitate spacing. They used an empirical law in order to describe their data:

$$\tau \propto R^2 \tag{4-11}$$

Even though their measurements indeed seem to follow a $\tau \propto R^2$ dependence, there are still a few points that are not addressed yet. First, in the classical diffusion case where the electrons diffuse out of the high-concentration, laser-excited region and accidentally get trapped by the As precipitates, it should be expected that the electron trapping rate should rise not only with the trap density (inverse trap spacing) but with the trap size as well. Second, the samples that are investigated in that work are subject to rather weak annealing conditions. This fact, as the authors note, might have possibly resulted in a remaining As point defect concentration that influences the mobility in the samples. Point defects also contribute to the ultrafast electron behavior of the material and their contribution should also be taken into account in order to evaluate the data and extract the characteristic electron trapping times. In **Fig. 4-35** we have tried to describe our results for the electron trapping times to the square of the As precipitate spacing. It is evident for $\tau$ that it does not follow the quantity $R^2$ but it exhibits a higher nonlinearity. Our samples on the other hand, are subject to stronger annealing conditions that ensure that any remaining As point defect concentration is minimized.

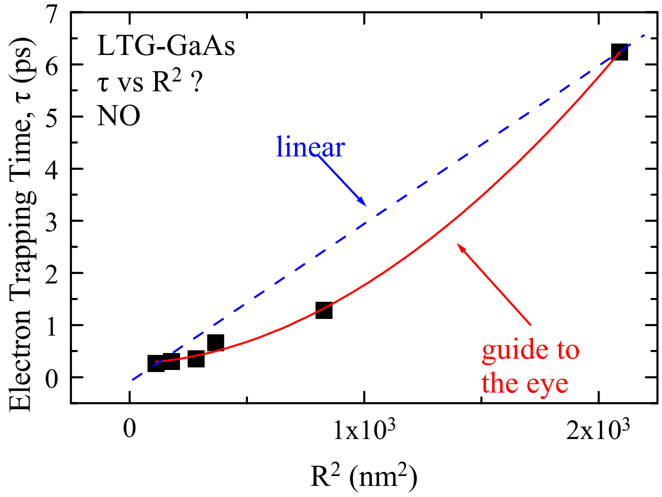

**Figure 4-35** Electron lifetimes versus $R^2$ as proposed by Melloch et al. [Melloch2] Our measurements show that this empirical model is inadequate to describe the electron trapping mechanism.

Ruda and Shik [Ruda] have recently solved the three-dimensional diffusion equation for the carriers and calculated that the electron trapping times should follow the law:

$$\tau = \frac{1}{3D}\frac{R^3}{\alpha} \qquad (4\text{-}12)$$

where $D$ is the diffusion constant, $R$ is the average spacing and $\alpha$ is the mean radius of the As precipitates. The diffusion equation (taking into account the continuity equation) that can describe our case is the following:

$$\frac{dn}{dt} = -D\nabla^2 n + G \qquad (4\text{-}13)$$

where $n$ is the electron concentration, $D$ is the diffusion constant and $G$ is the generation rate that accounts the electrons that are generated by excitation by the laser pulse. Here, we have neglected the recombination rate of the electrons annihilating with a hole since it is a very slow process compared to the generation and the diffusion of carriers and has a negligible contribution. In the state of the system, where $\frac{dn}{dt} = 0$, the equation reduces to:

$$\begin{aligned} &\nabla^2 n = \frac{G}{D} \Rightarrow \\ &\frac{1}{r}\frac{d^2(rn)}{dr^2} = \frac{G}{D} \end{aligned} \tag{4-14}$$

which is valid in the case that the diffusion is symmetric and depends only on the distance from the origin $r$. So the *n(r)* can be shown to be:

$$n(r) = \frac{G}{6D}r^2 + A + B\frac{1}{r} \tag{4-15}$$

where $A$, $B$ are constants. The boundary conditions they have used are that the electron concentration and the electron concentration gradient must vanish at the As precipitate surfaces and the As precipitate cells respectively (trapping information):

$$\begin{aligned} &n(\alpha) = 0 \\ &\left.\frac{dn}{dr}\right|_{r=R} = 0 \end{aligned} \tag{4-16}$$

Thus, the previous equation finally becomes:

$$n(r) = \frac{G}{3D}\left(-\frac{R^3}{\alpha} + \frac{R^3}{r} - \frac{\alpha^2}{2} + \frac{r^2}{2}\right) \tag{4-17}$$

Now, the average time that an electron needs to meet an As precipitate and get trapped can be defined as the fraction of the total number of nonequilibrium electrons in an effective sphere of radius *R* over the total generation rate of electrons in the same sphere (or more simply: what is left over what is initially created):

$$\tau = \frac{\iiint d^3 r n(r)}{G\frac{4\pi R^3}{3}} \Rightarrow$$
$$\tau = \frac{4\pi \int_{\alpha}^{R} n(r) r^2 dr}{G\frac{4\pi R^3}{3}} \tag{4-18}$$

Using the expression for *n(r)* and performing the integration, one can obtain:

$$\tau = \frac{\left[ -\left( \frac{R^3}{\alpha} + \frac{\alpha^2}{2} \right) \frac{R^3 - \alpha^2}{3} + R^3 \frac{R^2 - \alpha^2}{2} + \frac{1}{2} \frac{R^5 - \alpha^5}{5} \right]}{DR^3} \tag{4-19}$$

This is the strict expression that gives the electron trapping time with respect to the average As precipitate spacing *R* and its average radius *α*. However, in most cases and in ours in particular, this expression can be simplified if we make the use of the fact that the spacing *R* is much bigger than the radius *α*. For example, as can be derived by **Tab. 4-3** and **Tab. 4-4** for both LTG-GaAs and LTG-AlGaAs, the *R* is at the best case 50 times *α* and at the worst case 10 times *α*. With the above in mind, the last formula can be reduced to the justified approximation:

$$\tau \approx \frac{1}{3D} \frac{R^3}{\alpha} \tag{4-20}$$

In **Fig. 4-36** we have plotted our measurements for the electron trapping time $\tau$ versus the quantity $\frac{R^3}{\alpha}$. Clearly the results show a linear behaviour for $\tau$ versus $\frac{R^3}{\alpha}$. This latter model gives the best prediction for the electron trapping times and it is observed for the first time.[Loukakos] The observed trend leads us to the conclusions that the transport mechanism of the laser excited electrons is three dimensional diffusion and both the density (inverse spacing) and the size of the As precipitates affect the trapping of the electrons.

In **Fig. 4-37** the results of the electron decay times are plotted versus the quantity $\frac{R^3}{\alpha}$ for the

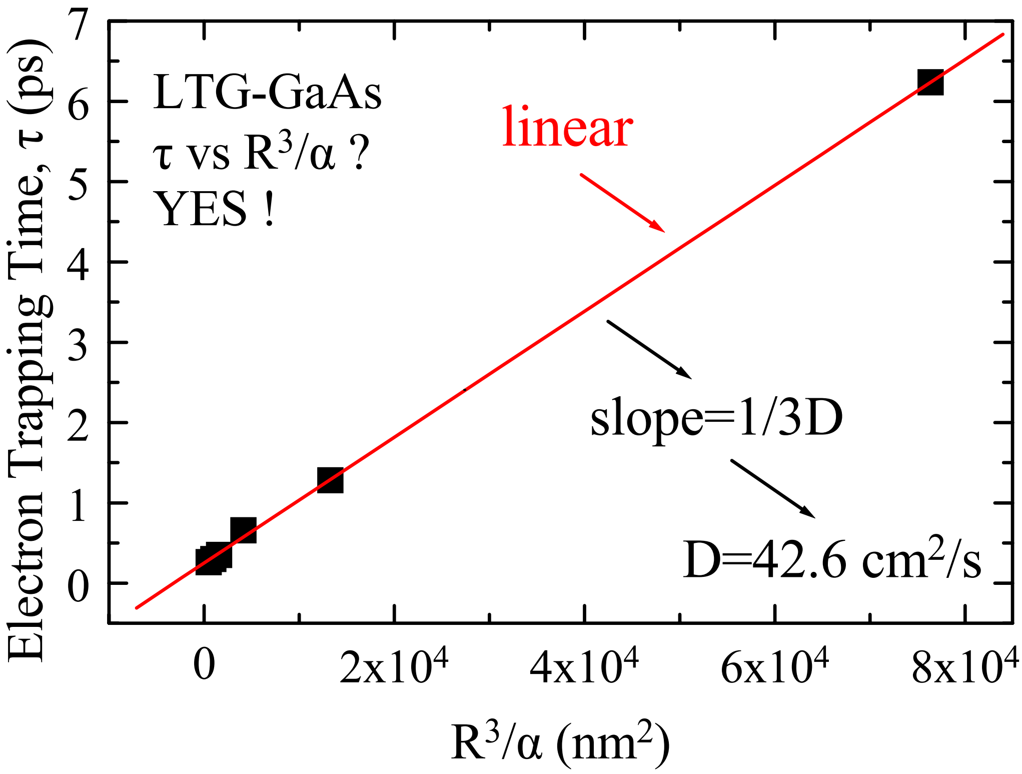

**Figure 4-36** Our results for the electron lifetimes versus the quantity $\frac{R^3}{\alpha}$ as predicted by Ruda et al.[Ruda] This graph shows that the correct mechanism for the electron population decay is diffusion-mediated trapping at the surfaces of the As precipitates.

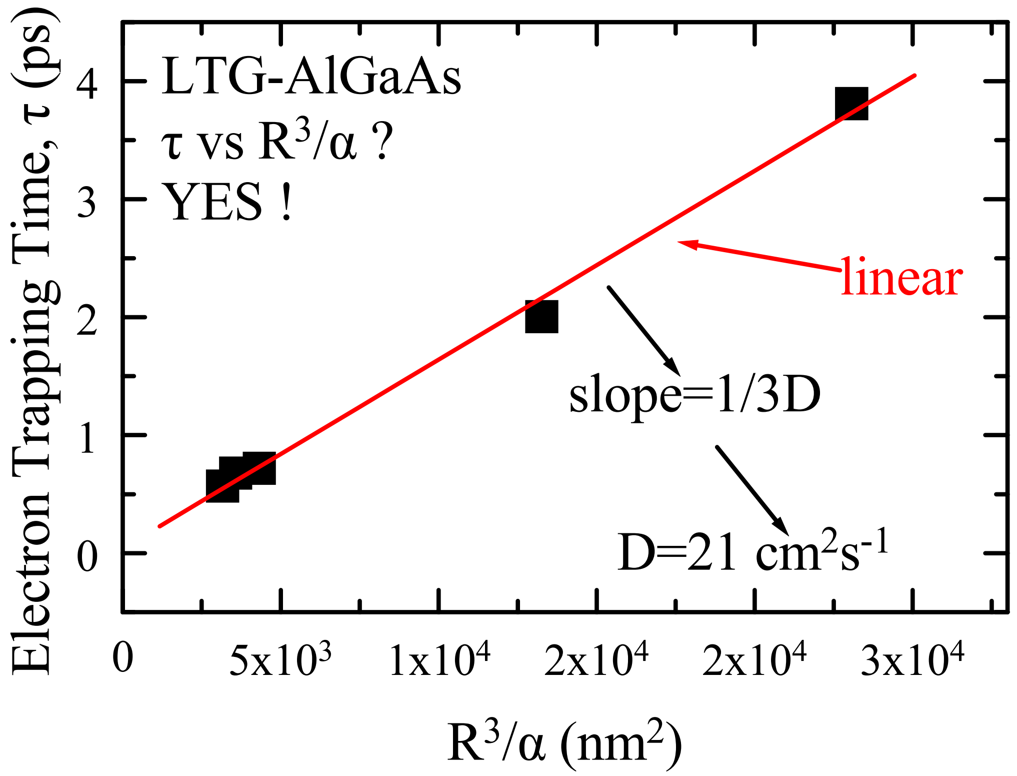

**Figure 4-37** Electron trapping times in AlGaAs versus $\frac{R^3}{\alpha}$. The behavior is similar to GaAs.

LTG-AlGaAs. The data are taken at a pump and probe wavelength of 800 nm (the 800 nm pumping wavelength excites the electrons to an energy about 20 meV above the bottom of the conduction band). The electron decay times clearly exhibit a monotonic behavior with the quantity $\frac{R^3}{\alpha}$.

**Loukakos2**

The result that is to be extracted by the last two figures is that as in the case of LTG-GaAs the electron decay times clearly follow a $\frac{R^3}{\alpha}$ behavior. The deviation of the data points from the linear fitting is negligible. This fact justifies the same considerations that are used for the LTG-GaAs case to be applied here without any modifications: after the excitation by the laser pump pulse the electrons diffuse out of the initially high electron concentration region and get trapped on the As precipitate surfaces. Both the As precipitate average spacing and radius affect the trapping process.

A very interesting point here, is that from the formula that gives the trapping time as a function of $R$ and $\alpha$ and the experimental data it is evident that one can readily obtain the diffusion coefficient $D$. The slope of the linear curve of $\tau$ versus $\frac{R^3}{\alpha}$ is $\frac{1}{3D}$ as predicted by the model. Thus, by ,manipulation of the experimental data, the value obtained for $D$ for the case of LTG-GaAs is $D$=43 $cm^2/s$. **Loukakos2**

Using the Einstein relationship (assuming thermodynamic equilibrium: a rather drastic approximation):

$$\frac{D}{\mu} = \frac{k_B T}{q} \tag{4-21}$$

the mobility of the electrons can also be obtained. The value for the mobility is measured to be $\mu$=1652 $cm^2/Vs$ for LTG-GaAs. This value varies noticeably from the values given by Look et al. **Look** for the mobility of a LTG-GaAs sample grown at 200 $^oC$ and annealed at 600 $^oC$ for 10 min. Moreover as it is obvious by the results in that work, **Look** the mobility (and therefore the diffusion coefficient as well) varies with the annealing temperature and therefore with the As precipitate characteristics. In contrast we give only one value for $\mu$ and $D$ which is common for all samples measured in this work regardless the growth conditions or the As precipitate sizes and densities. We have to note here that the values for the diffusion coefficient $D$ and mobility $\mu$ we obtained are to be treated as "intrinsic" quantities of our samples. The values obtained in a classical Hall experiment are restricted by scattering of the carriers from a great number of various defects. These scattering events take place in a time scale **Seeger** of the order of 1 ps that is the typical time value for electron trapping experiments in LTG-GaAs materials. Our results give values for the mobility and the diffusion coefficient that are restricted by only a few, if not any, scattering events by crystal defects. Moreover, because of the strong annealing conditions we used in the preparation of out samples, all the crystalline defects are minimized and the lattice constant is relaxed to that of the normal grown semiconductor. **Melloch** Therefore we expect the mobility to have the same value for the measured samples in contrast to samples grown and prepared in such way to measure the Hall mobilities. **Look**

For the LTG-AlGaAs case, by the linear fitting in **Fig. 4-37** we obtain the value $D$=21 cm$^2$/s for the diffusion coefficient and using again the Einstein formula the value $\mu$=805 cm$^2$/Vs for the mobility. The same discussion applies here for the LTG-AlGaAs samples as above for the LTG-GaAs samples for the “intrinsic” behavior of the mobility and the diffusion coefficient.

A point that must be addressed concerns the increasing spacing between the data points plotted, especially the last ones in the case of LTG-GaAs (**Fig. 4-36**). This could be a potential problem in determining the correct slope for the linear curve because of the largely increased weight of the last data points. To overcome this problem the linear behavior of the data is examined while progressively omitting the last data point, one at a time. All linear fittings produced had no significant variations in the curve slopes. For example we show that the two fitting results obtained with and without the use of the last data point differ to only an insignificant 1 % as shown in **Fig. 4-38** for the case of LTG-GaAs.

Another consideration to be addressed concerns the dimensionality of the diffusion and specifically whether the latter is 3-dimensional or exhibits a reduced dimensionality due to spatial restrictions of the grown samples. The grown epilayers have a thickness of typically 1 μm. The characteristic diffusion length of the electrons can be estimated using the formula **Seeger**

$$L = \sqrt{D\tau} \qquad (4\text{-}22)$$

where *D* is the diffusion constant and *τ* is the electron lifetime. We use the value of $D$=50 cm$^2$/s (25.9 cm$^2$/s for *D* and 10$^3$ cm$^2$/Vs for *μ* as given by Seeger [Seeger]) for the diffusion constant and the value of 1 ps for the electron lifetime. The diffusion length takes the value of about 70 nm. This value is clearly much smaller from the typical width of the epilayers we use. Thus, the mechanism that the electrons are subject to, may fairly well be considered to be three dimensional diffusion and our results show a consistency with the above arguments. The situation is similar and even better for the LTG-AlGaAs samples since the value we obtained for the diffusion coefficient is smaller that the LTG-GaAs case.

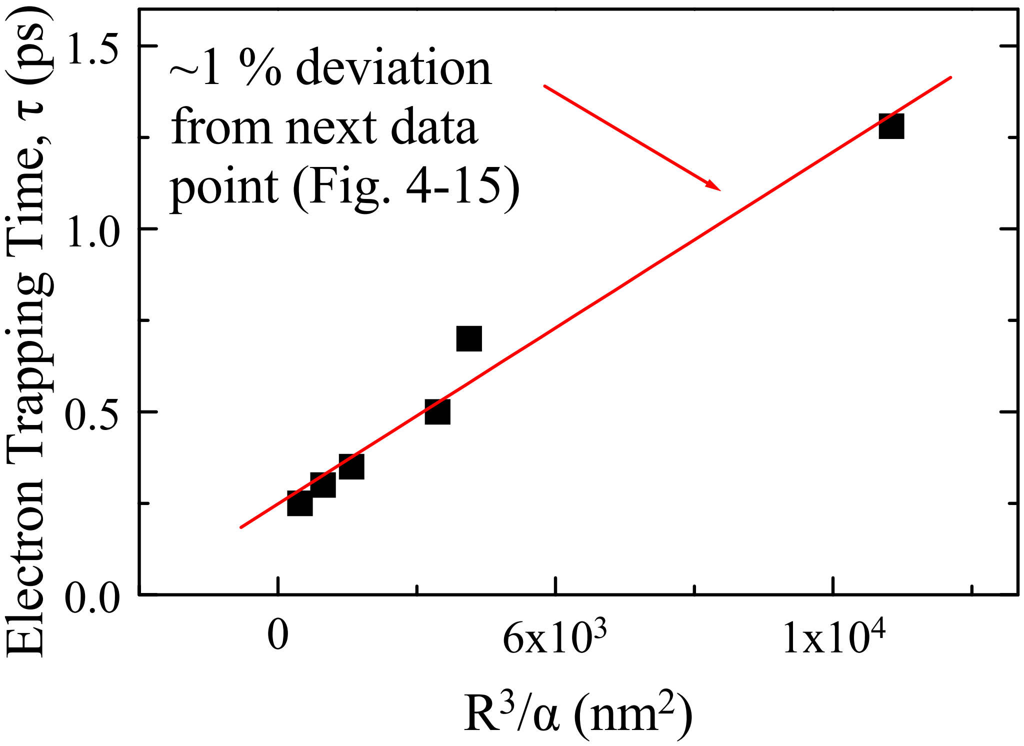

**Figure 4-38** The same results as in Fig. 4-36 except the last data point showing that the linear fitting results do not vary noticeably even by neglection of the last, high-weight data point.

## 4.6 Conclusions

A series of LTG-GaAs and LTG-AlGaAs semiconductors has been grown in order to investigate the ultrafast electronic response of these materials. Optical ultrafast transient spectroscopy has been utilized in order to reveal the ultrafast electronic properties. The results for the LTG-GaAs show that:

- The free conduction band electron internal thermalization times do not depend on the defects of the crystal in the form of the As precipitates in the ~100 fs domain. Also, no deviation between LTG-GaAs and LTG-AlGaAs is found, probably due to the low Al mole fraction.

- The ultrafast conduction band electron population decay is associated to the presence of the excess As when this is found in the form of As precipitates in both LTG materials.

- The ultrafast decay of the electron population is due to diffusion mediated trapping of the free electrons to the surfaces of the As precipitates in both materials.

- For the preparatory conditions of our sample the buried Shottky barrier model is the one that can describe the ultrafast electron kinetics and their associated trapping caused by the excess As.

- The trapping times of the free electrons depend on both the As precipitate density and size. The interplay of these parameters and the corresponding time dependence is given by the $\tau \approx \frac{1}{3D}\frac{R^3}{\alpha}$ law, which is analytically predicted by a simple electron diffusion model. The absolute values of the electron trapping times differ between

LTG-GaAs and LTG-AlGaAs due to the different mobility of carriers, but the trend with respect to the As precipitate characteristics is the same.

We are also able to extract the "intrinsic" values for the mobility and the diffusion coefficient that are not restricted by scattering events caused by defects in the semiconductor matrix. We will continue with further investigation to other III-V semiconductors and related alloys with various structure parameters in order to generalize and elucidate the ultrafast electron trapping mechanisms.

The conclusions made for AlGaAs alloys and especially the anticipated values for the electron trapping times with respect to the As precipitate characteristics become very important when one needs to engineer tunable materials for use in high-speed optoelectronic devices.

## 4.7 References

**Allali** M. El Allali, C. B. Sorensen and E. Veje, Phys. Rev. B **48**, 4398 (1993).

**Benjamin** S. D. Benjamin, H. S. Loka, A. Othonos, and P. W. E. Smith, Appl. Phys. Lett. **68**, 2544 (1996).

**Blakemore** J. S. Blakemore, J. Appl. Phys. **53**, R123 (1982).

**Fauchet** P. M. Fauchet, G. W. Wicks, Y. Kostoulas, A. I. Lobad, and K. B. Ucer, Mat. Res. Soc. Symp. Proc. **378**, 171 (1995).

**Feng** W. Feng, Z. G. Zhang, Y. Yu, Q. Huang, P. M. Fu, and J. M. Zhou, J. Appl. Phys. **79**, 7404 (1996).

| | |
|---|---|
| **Gupta** | S. Gupta, M. Y. Frankel, J. A. Valdmanis, J. F. Whitaker, G. A. Mourou, F. W. Smith, and A. R. Calawa, Appl. Phys. Lett **59**, 3276 (1991). |
| **Harmon** | E. S. Harmon, M. R. Melloch, J. M. Woodall, D. D. Nolte, N. Otsuka, and C. L. Chang, Appl. Phys. Lett. **63**, 2248 (1993). |
| **Kaminska** | M. Kaminska "Defects in non-stoichiometric III-V compounds", in Semi-Insulating III-V Materials, Warsaw, Poland 1994, p.327. |
| **Lahiri** | I. Lahiri, D. D. Nolte, E. S. Harmon, M. R. Melloch, and J. M. Woodall, Appl. Phys. Lett. **66**, 2519 (1995). |
| **Liliental** | Z. Liliental-Weber, W. Swider, K. M. Yu, J. Kortright, F. W. Smith, and A. R. Calawa, Appl. Phys. Lett. **58**, 2153 (1991). |
| **Liliental 2** | Liliental-Weber et al. Semi-insulating III-V materials (1994) 305. |
| **Liliental3** | Z. Liliental-Weber, H. J. Cheng, S. Gupta, J. Whitaker, K. Nichols, and F. W. Smith, J. Electron. Mater. **22**, 1465 (1993). |
| **Lin** | W-Z. Lin, R. W. Schoenlein, J. G. Fujimoto, and E. P. Ippen, IEEE J. Quant. Electr. **24**, 267 (1988). |
| **Lochtefeld** | A. J. Lochtefeld, M. R. Melloch, J. C. P. Chang, and E. S. Harmon, Appl. Phys. Lett. **69**, 1465 (1996). |
| **Loka** | H. S. Loka, S. D. Benjamin, and P. W. E. Smith, Opt. Commun. **161**, 232 (1999). |
| **Look** | D. C. Look, D. C. Walters, G. D. Robinson, J. R. Sizelove, M. G. Mier, and C. E. Stutz, J. Appl. Phys. **74**, 306 (1993). |

| | |
|---|---|
| **Loukakos** | P. A. Loukakos, C. Kalpouzos, I. E. Perakis, Z. Hatzopoulos, M. Logaki, and C. Fotakis, Appl. Phys. Lett. **79**, 2883 (2001). |
| **Loukakos2** | P. A. Loukakos, C. Kalpouzos, I. E. Perakis, Z. Hatzopoulos, M. Sfendourakis, G. Konstantinidis, and C. Fotakis, accepted for publication in J. Appl. Phys., scheduled publication date June 15, 2002. |
| **McIntosh** | K. A. McIntosh, K. B. Nichols, S. Verghese and E. R. Brown Appl. Phys. Lett. **70**, 354 (1997). |
| **Mahalingam** | K. Mahalingam, N. Otsuka, M. R. Melloch, J. M. Woodall, and A. C. Warren, J. Vac. Sci. Technol. **B9**, 2328 (1991). |
| **Marcinkevicius** | S. Marcinkevicius, C. Jagadish, H. H. Tan, M. Kaminska, K. Korona, R. Adomavicius, and A. Krotkus, Appl. Phys. Lett. **76**, 1306 (2000). |
| **Marcinkevicius2** | S. Marcinkevicius, A. Krotkus, R. Viselga, U. Olin, and C. Jagadish, Semicond. Sci. Technol. **12**, 396 (1997). |
| **Melloch** | M. R. Melloch, D. D. Nolte, J. M. Woodall, J. C. P. Chang, D. B. Janes, and E. S. Harmon, Critical Reviews in Solid State and Materials Sciences **21**, 189 (1996). |
| **Melloch2** | M. R. Melloch, J. M. Woodall, E. S. Harmon, N. Otsuka, F. H. Pollak, R. M. Feenstra, and M. A. Lutz, Annu. Rev. Mater. Sci. **25**, 547 (1995). |
| **Melloch3** | M. R. Melloch, J. M. Woodall, E. S. Harmon, N. Atique, D. D. Nolte, J. C. P. Chang, and N. Otsuka, Semi-insulating III-V Materilas, World Scientific, Warsaw, Poland, 319 (1994). |

**Melloch4** M. R. Melloch, N. Otsuka, J. M. Woodall, A. C. Warren, and J. L. Freeouf, Appl. Phys. Lett. **57**, 1531 (1990).

**Murotani** T. Murotani, T. Shimanoe, and S. Mitsui, J. Cryst. Growth **45**, 302 (1978)

**Othonos** A. Othonos, J. Appl. Phys., **83**, 1789 (1998).

**Prabhu** S. S. Prabhu, S. E. Ralph, M. R. Melloch and E. S. Harmon, Appl. Phys. Lett. **70**, 2419 (1997).

**Schaff** W. J. Schaff, S. D. Offsey, X. J. Song, L. F. Eastman, T. B. Norris, W. J. Sha, and G. A. Mourou, Mat. Res. Soc. Symp. Proc. **241**, 51 (1992).

**Seeger** See for example K. Seeger, Semiconductor Physics, Springer (1997).

**Siegner** U. Siegner, R. Fluck, G. Zhang, and U. Keller, Appl. Phys. Lett. **69**, 2566 (1996)

**Sosnowski** T. S. Sosnowski, T. B. Norris, H. H. Wang, P. Grenier, J. F. Whitaker, and C. Y. Sung, Appl. Phys. Lett. **70**, 3245 (1997).

**Tersoff** J. Tersoff, Phys. Rev. Lett. **52**, 465 (1984).

**Warren** A. C. Warren, N. Katzenellenbogen, D. Grischkowsky, J. M. Woodall, M. R. Melloch, and N. Otsuka, Appl. Phys. Lett. **58**, 1512 (1991).

**Warren2** A. C. Warren, J. M. Woodall, P. D. Kirchner, X. Yin, F. Pollak, M. R. Melloch, N. Otsuka, and K. Mahalingam, Phys. Rev. B **46**, 4617 (1992).

**Witt** G. L. Witt, Semi-insulating III-V Materials, World Scientific, Warsaw, Poland 1994, p. 297.

# Chapter 5 Metallic Nanocomposites: Background

## 5.1 Introduction

The scope of this chapter is to present the basic optical properties that make the metal nanocrystalls distinct from the bulk and the fundamental procedures that take place in the ultrafast domain. The theory presents the main modifications that the electronic system undergoes and are invoked by the confinement. The effect of the confinement on the optical and electronic properties of nanocrystalline materials is discussed. Also, the steps in analyzing the ultrafast electron dynamics are presented. It is not our intention to present a rigorous mathematical description rather than the basic formalism that describes the fundamental mechanisms.

## 5.2 Structure of Au

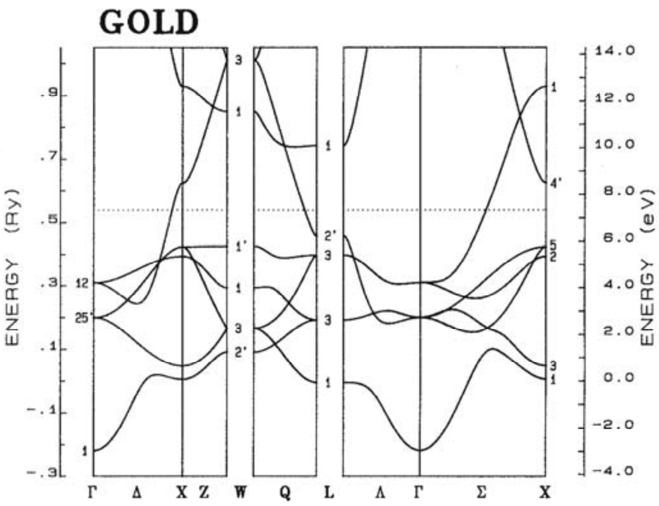

**Figure 5-1** The complete band diagram for the Au crystal, as taken from Papaconstantopoulos. [Papaconstantopoulos]

The atom of Gold (Au) belongs to the first column of elements. Its electronic structure [Elements] is (Xe) $6s^1$ $4f^{14}$ $5d^{10}$. In solid state, Au can form a periodic lattice. The last occupied state in the Au atom, as can be seen by its electronic structure, is 6s. It has only one electron while it can accept two. Thus, in its solid state, the Au crystal will have a conduction band that is half filled. The immediately lower band, the d-band, is going to be completely full, since it derives from the interference of the 5d atomic zones that are completely full of electrons. In **Fig. 5-1** the band structure [Papaconstantopoulos] of Au is presented.

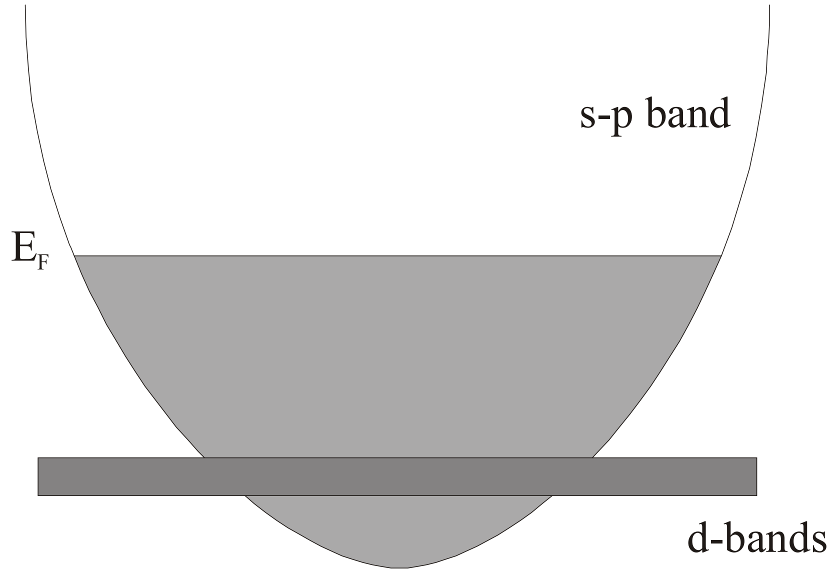

**Figure 5-2** Simplified *E-**k*** diagram of the energy bands of the Au crystal. The overlapping of the s-p and the d-bands is only schematic.

In **Fig. 5-2** the reader can see a simplified illustration of the last two bands in crystalline Au. [Voisin] The last bands, the valence (d-bands) and the conduction (s-p) band are presented. The valence band is completely full with electrons. The conduction band is semi-full. At $T=0$ °K, the last energy state occupied by electrons in the conduction band is called the Fermi state and its corresponding energy the Fermi energy, $E_F$. For Au, $E_F$=5.51 eV. At higher temperatures, the energy rises because of thermal excitation of electrons. For the sake of simplicity we are going to use this picture to describe the optical properties in Au and the relevant nanometric dimension materials. In this view, the conduction band can be assumed to have parabolic shape and the dispersion relation reads:

$$E(\vec{k}) \approx \frac{\hbar^2 k^2}{2m} \tag{5-1}$$

where $k$ is the wave number and $m$ is the effective mass of the electrons, given by: **Kittel**

$$m = \frac{\hbar^2}{\frac{\partial^2 E}{\partial k^2}} \tag{5-2}$$

The probability of occupation by electrons of an state with energy $E$ at temperature $T$ (occupation number) follows a Fermi-Dirac distribution:

$$f_T(E) = \frac{1}{e^{\frac{(E-E_F)}{k_B T}} + 1} \tag{5-3}$$

The density of states in an energy $E$ of the conduction band is:

$$\frac{dN}{dE} = \frac{V}{2\pi^2}\left(\frac{2m}{\hbar^2}\right)^{3/2}\sqrt{E} \tag{5-4}$$

where $V$ is the total volume of the system and the Fermi energy $E_F$, is given by:

$$E_F = \frac{\hbar^2}{2m}\left(3\pi^2 n_c\right)^{2/3} \tag{5-5}$$

where $n_c$ is the conduction band density of electrons.

For a review of the structure of metals in general, the reader can refer to Solid State Physics by Kittel. **Kittel**

## 5.3 Optical Properties

The optical properties of Au and related nanocrystalls are affected by the quantum structure of the system and the frequency of the illuminating radiation. For this study, the simple model already presented in **Fig. 5-2** will be considered, and optical and near infrared frequencies will also be considered because this is the range of frequencies used in this work. Regarding the initial and the final state of the electrons, all light-electron interactions can be divided in two major categories:

- inter-band procedures: they involve an initial and a final state in different bands (d-bands to s-p band).
- intra-band procedures: they involve initial and final states inside the same band (s-p band) for the electronic energy states.

Optical excitation with the use of an ultrashort laser pulse having wavelengths used in this work can cause both intra- or interband excitation of electrons.

Thermal excitation is the product of collisions between electrons due to elevated temperature and thus due to increased kinetic energy. In normal room-temperature conditions (around 300 $^{o}$K) the thermal energy is adequate only for intraband excitation of electrons, since the thermal energy is about 26 meV in room temperature and the threshold for interband transitions in Au is 2.4 eV. **Voisin** The elevated temperature affects the position of the Fermi level.

The most interesting feature in confined metallic system like the Au nanocrystals is the appearance of a resonance in the absorption spectrum that is called the Surface Plasmon Resonance (SPR). This resonance is the result of the confinement of the system either dielectric or quantum. **Kawabata, Halperin, Genzel** Roughly, in the quantum case, the particle is so small in dimensions that it contains a rather small number of atoms that is so small that the energy continuum breaks into discrete energy levels since the system starts to behave as a small ensemble of atoms. In the dielectric case, the particles are not that small and contain a much bigger amount of atoms so that the continuum of energy still persists, but the confinement source is the localized Maxwell electric field that results in the morphological resonance. We will consider the second case in this work, since the smallest particle investigated (1 nm radius) contains about 62 Au atoms while for a 2 nm radius the number of Au atoms is about 493 (lattice constant of Au: $\alpha$=4.08 Å $^{\textbf{Kittel}}$).

The specimens that we are going to use in this work are comprised of a dielectric matrix of dielectric constant $\varepsilon_m$ that contain spherical metallic clusters of dielectric constant $\varepsilon$ and radius $\alpha$ that is much smaller than the excitation wavelength $\lambda$. For comparison, the clusters have a typical

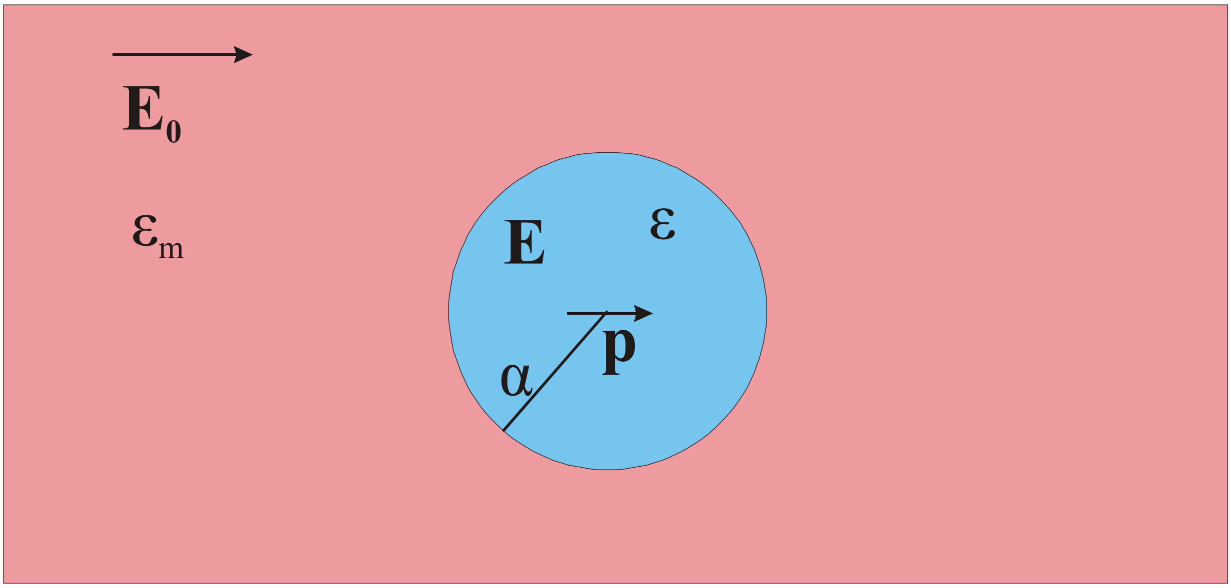

**Figure 5-3** A metallic sphere of dielectric constant $\varepsilon$ is embedded inside a material of dielectric constant $\varepsilon_m$.

radius of a few nm while the excitation wavelength is typically about 0.5 μm. The volume $p = \frac{V_{metal}}{V_{total}}$ is small, in the order of $10^{-2}$ to $10^{-4}$. The applied (external filed) is $\vec{E}_0$. A schematic representation is shown in **Fig. 5-3**.

A macroscopic field $\vec{E}$ is induced inside the metallic sphere. However, the local field $\vec{E}_l$ that an atom of the sphere is subject to, will be connected with the macroscopic field $\vec{E}$ and the polarization $\vec{P}_S$ of the spheres with: **Kittel**

$$\vec{E}_l = \vec{E} + \frac{\vec{P}_S}{3\varepsilon_m \varepsilon_0} \tag{5-6}$$

The polarization $\vec{P}_S$ is induced by the external field $\vec{E}_0$. $\vec{P}_S$ is connected to the macroscopic field $\vec{E}$ with the relation:

$$\vec{P}_S = \varepsilon_0 \chi \vec{E} \tag{5-7}$$

where $\chi = \varepsilon - 1$ is the susceptibility. Using the relation between $\vec{E}$ and $\vec{E}_l$ (**Eq. 5-6**), one can get:

$$\vec{P}_S = 3\varepsilon_0 \varepsilon_m \frac{\varepsilon - \varepsilon_m}{\varepsilon + \varepsilon_m} \vec{E}_l \tag{5-8}$$

The last relation gives the total polarization of the whole sphere with the local field $\vec{E}_l$ that each atom of the sphere feels. The total polarization will be the sum of those of the metallic nanoparticles and the dielectric matrix (taking also in account the proportionality factor, or volume fraction $p$):

$$\vec{P}_T = p\vec{P}_S + \vec{P}_0 \tag{5-9}$$

where $\vec{P}_S$ is given by **Eq. 5-8** and

$$\vec{P}_0 = \varepsilon_0 (\varepsilon_m - 1) \vec{E}_0 \tag{5-10}$$

We are going to define a new effective dielectric constant $\widetilde{\varepsilon}$ by the total dielectric displacement vector:

$$\vec{D}_T = \varepsilon_0 \widetilde{\varepsilon} \vec{E}_0 = \varepsilon_0 \vec{E}_0 + \vec{P}_T \tag{5-11}$$

Then, taking into account that [Kittel] $\vec{E}_l = \vec{E}_0$, we get:

$$\widetilde{\varepsilon} = \varepsilon_m + 3p\varepsilon_m \frac{\varepsilon - \varepsilon_m}{\varepsilon + 2\varepsilon_m} = \widetilde{\varepsilon}_1 + i\widetilde{\varepsilon}_2 \tag{5-12}$$

with:

$$\begin{cases} \widetilde{\varepsilon}_1 = \varepsilon_m + 3\pi\varepsilon_m \dfrac{\varepsilon_1{}^2 + \varepsilon_m \varepsilon_1 - 2\varepsilon_m{}^2 + \varepsilon_2{}^2}{(\varepsilon_1 + 2\varepsilon_m)^2 + \varepsilon_2{}^2} \xrightarrow{p<<1} \varepsilon_m \\ \widetilde{\varepsilon}_2 = 9p\varepsilon_m{}^2 \dfrac{\varepsilon_2}{(\varepsilon_1 + 2\varepsilon_m)^2 + \varepsilon_2{}^2} \end{cases} \tag{5-13}$$

which is valid for low volume fractions $p << 1$.

Now, the absorption coefficient $\alpha$ is defined by the formula:

$$I = I_0 e^{-\alpha x} \tag{5-14}$$

The global absorption coefficient of the composite material can be shown [Voisin] to take the form:

$$\alpha(\omega) = \frac{9p\varepsilon_m{}^{3/2}}{c} \frac{\omega \varepsilon_2(\omega)}{[\varepsilon_1(\omega) + 2\varepsilon_m]^2 + \varepsilon_2{}^2(\omega)} \tag{5-15}$$

From the denominator of the last formula it can be seen that there exists a frequency $\Omega_R$ such that

$$\varepsilon_1(\Omega_R) + 2\varepsilon_m = 0 \qquad (5\text{-}16)$$

that magnifies the absorption coefficient $\alpha$. $\Omega_R$ is called the Surface Plasmon Resonance (SPR) frequency and is the result of the dielectric confinement discussed above. For example, absorption spectra for Ag and Au nanoparticles of radius $R$=2.2 nm and $R$=5 nm respectively are shown in **Fig. 5-4** and **Fig. 5-5**. In a classical point of view , the SPR corresponds to a collective oscillation of the electron population.

Furthermore, taking into account the Drude approximation (see **APPENDIX**) $\varepsilon_1 \approx \varepsilon_1^{ib} - \frac{\omega_p{}^2}{\omega}$ we can get:

$$\Omega_R = \frac{\omega_p}{\sqrt{\varepsilon_1^{ib}(\Omega_R) + 2\varepsilon_m}} \qquad (5\text{-}17)$$

Using the global electronic collision rate $\gamma'(\omega)$ we can write (see **APPENDIX**):

$$\begin{cases} \varepsilon_1(\omega) = \varepsilon_1^{ib}(\omega) - \dfrac{\omega_p{}^2}{\omega^2} \\ \varepsilon_2(\omega) = \varepsilon_2^{ib}(\omega) + \dfrac{\omega_p{}^2}{\omega^3}\gamma(\omega) = \dfrac{\omega_p{}^2}{\omega^3}\gamma'(\omega) \end{cases} \qquad (5\text{-}18)$$

And in the case that the dispersion of $\varepsilon_1^{ib}$ and $\gamma'$ is negligible (when the SPR and the interband transition threshold are well separated, i.e. Ag, **Fig. 5-4**) the absorption coefficient obtains a Lorentzian shape:

$$\alpha(\omega) \approx \frac{9p\varepsilon_d^{\;3/2}}{C_0\omega_p^{\;2}} \frac{\omega^2 \Omega_R^{\;4} \gamma_R'}{\left(\omega^2 - \Omega_R^{\;2}\right)^2 + \left(\dfrac{\gamma_R' \Omega_R^{\;2}}{\omega}\right)^2} \tag{5-19}$$

However, in Au, the SPR and the interband transition threshold frequency are not separated at all and the above approximation is not valid (**see Fig. 5-5**).

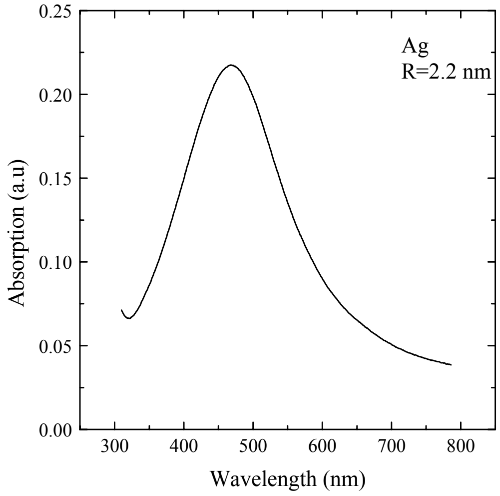

**Figure 5-4** The absorption spectrum of Ag nanoparticles in the vicinity of the SPR.

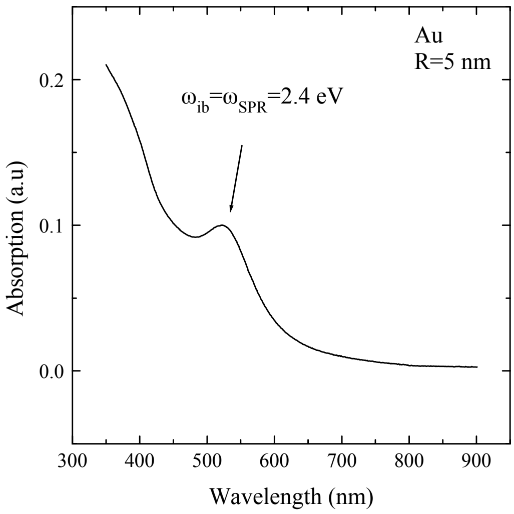

**Figure 5-5** The absorption spectrum of Au nanoparticles in the vicity of the SPR. The SPR and the threshold for interband transitions overlap.

## 5.4 Relaxation Mechanisms

After the "instant" of perturbation the initial electron population starts to evolve back towards equilibrium. Two are the main mechanisms that take place during the relaxation of the electron population towards equilibrium: electron-electron and electron-phonon interactions. Both mechanisms are nonradiative procedures. They occur during diffusion of the electron population from the initial laser excited area of the metal towards surrounding areas where the density of carriers is smaller. (see also **Chap. 3**)

We are going to use the approach that the evolution of the occupation number for a particle is given by a Boltzmann-like equation:

$$\frac{df(\vec{k},t)}{dt} = \left.\frac{df(\vec{k},t)}{dt}\right|_{e-e} + \left.\frac{df(\vec{k},t)}{dt}\right|_{e-ph} + L(\vec{k},t) \qquad (5\text{-}20)$$

where $L(\vec{k},t)$ is the excitation by the laser pump pulse for the state $\vec{k}$ at the instant *t*. The first term represents the variation of the occupation number due to electron-electron collisions and the second term due to electron-phonon collisions. The above equation describes the simple fact that the total change in the number of electrons will be the sum of the changes due to the distinct processes that change the number of electrons. These are the loss due to electron-electron collisions, the loss due to electron-phonon collisions and the gain due to excitation by the laser pulse. The theoretical problem to be solved here is to try to calculate the three terms in the right-hand side of **Eq. 5-20**, so as to model the kinetics of the electron population after the laser excitation, either analytically, or numerically with the use of powerful computer systems. We are not going to concern ourselves with the exact solution, however the basic guidelines will be presented that lead to the numerical modeling of the electron kinetics that are associated with the first term of **Eq. 5-20**, namely the

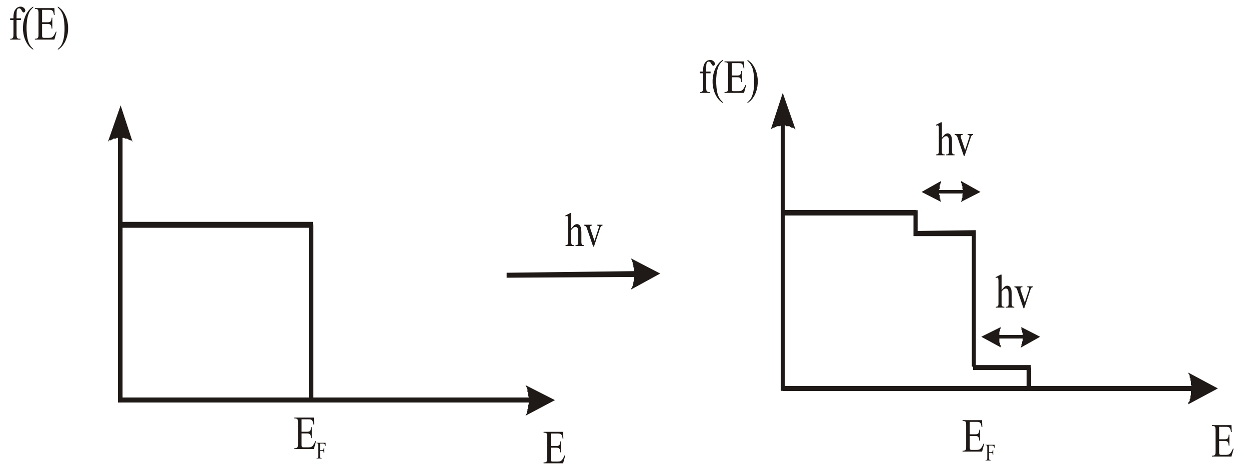

**Figure 5-6** (a) the electron distribution just before excitation. (b) the change in the electron distribution just after excitation.

internal thermalization of the electron population.

Before proceeding to the study of the first term on the right-hand side of the Boltzmann equation one must first calculate the initial change in the electron population just after the laser excitation. The initial athermal electron population can be visualized in **Fig. 5-6**. Electrons absorbing a photon of energy hω can either arrive to energy *E* from a state of energy $E-\hbar\omega$ or depart from the state *E* towards a state with energy $E+\hbar\omega$. Assigning the arriving number of electrons with $dN_{+}(E)$ and the departing number of electrons with $dN_{-}(E)$, and using $dN=\rho(E)f(E)$, where *ρ(E)* is the density of states, we get:

$$\begin{aligned} dN_{+}(E) &= A\left\{\sqrt{E-\hbar\omega}\, f_0(E-\hbar\omega)\sqrt{E}\left[1-f_0(E)\right]\right\} \\ dN_{-}(E) &= A\left\{\sqrt{E}\, f_0(E)\sqrt{E+\hbar\omega}\left[1-f_0(E+\hbar\omega)\right]\right\} \end{aligned} \qquad \textit{(5-21)}$$

where $A=\frac{V}{2\pi^2}\left(\frac{2m}{\hbar^2}\right)^{3/2}$ and the total number of electrons with energy *E* will be $dN=dN_{+}-dN_{-}$.

Consequently:

$$dN = A\sqrt{E}\left\{\sqrt{E-\hbar\omega}\, f_0(E-\hbar\omega)\left[1-f_0(E)\right]-\sqrt{E+\hbar\omega}\, f_0(E)\left[1-f_0(E+\hbar\omega)\right]\right\} \qquad \textit{(5-22)}$$

which corresponds to a change in the occupation number due to excitation:

$$df_{exc} = \sqrt{E-\hbar\omega}\, f_0(E-\hbar\omega)\left[1-f_0(E)\right]-\sqrt{E+\hbar\omega}\, f_0(E)\left[1-f_0(E+\hbar\omega)\right] \qquad \textit{(5-23)}$$

which is the initial, athermal electron population and gives the third term in the Boltzmann equation:

$$L(E,t)=\frac{I(t)}{\int_{-\infty}^{+\infty} I(\tau)d\tau}\, df_{exc} \qquad \textit{(5-24)}$$

where *I(t)* is the pump pulse intensity time profile. Because the transition mentioned is an intraband procedure, the total electron population remains constant.

In the view that the electrons just after the laser excitation are subject to a process of diffusion and accidental collisions with other electrons, we can visualize this process in **Fig. 5-7**. Two electrons of initial states $\left|\vec{k}_1\right\rangle$ and $\left|\vec{k}_2\right\rangle$ collide and scatter into two new states $\left|\vec{k}_3\right\rangle$ and $\left|\vec{k}_4\right\rangle$. The probability of such a collision is given by (Fermi's Golden Rule): **Seeger**

$$\left.\frac{df(\vec{k}_1)}{dt}\right|_{e-e} = \frac{2\pi}{\hbar}\sum_{\vec{k}_2,\vec{k}_3,\vec{k}_4}\left|M\right|^2 F(\vec{k}_1,\vec{k}_2,\vec{k}_3,\vec{k}_4)\delta(\vec{k}_1+\vec{k}_2-\vec{k}_3-\vec{k}_4)\delta(E_1+E_2-E_3-E_4) \qquad (5\text{-}25)$$

where $M\left(\vec{k}_1,\vec{k}_2,\vec{k}_3,\vec{k}_4\right)$ is the interaction matrix and the $\delta$-functions represent the conservation of momentum and energy and where $F$ represents the Pauli exclusion principle, i.e. the fact that for a transition to be possible the initial states must be filled and the final states must be empty:

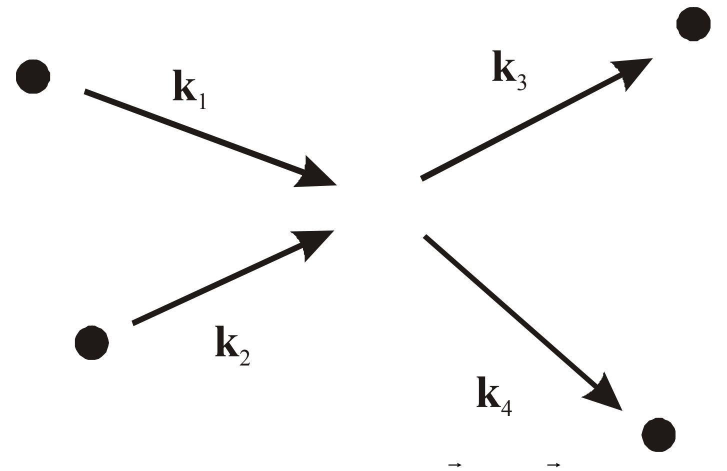

**Figure 5-7** Two electrons with $\vec{k}_1$ and $\vec{k}_2$ collide and scatter to two new $\vec{k}_3$ and $\vec{k}_4$.

$$F(\vec{k}_1,\vec{k}_2,\vec{k}_3,\vec{k}_4) = f(\vec{k}_3)f(\vec{k}_4)\left[1-f(\vec{k}_1)\right]\left[1-f(\vec{k}_2)\right] - f(\vec{k}_1)f(\vec{k}_2)\left[1-f(\vec{k}_3)\right]\left[1-f(\vec{k}_4)\right] \qquad (5\text{-}26)$$

**Eq. 5-25** can be reduced to:

$$\left.\frac{df(\vec{k}_1)}{dt}\right|_{e-e} = \frac{2\pi}{\hbar}\sum_{\vec{k}_2,\vec{k}_3}\left|M(\vec{k}_4=\vec{k}_1+\vec{k}_2-\vec{k}_3)\right|^2 F(\vec{k}_1,\vec{k}_2,\vec{k}_3,\vec{k}_4)\delta(E_1+E_2-E_3-E_4) \qquad (5\text{-}27)$$

We can define a new variable $\vec{q} = \vec{k}_1 - \vec{k}_3 = \vec{k}_4 - \vec{k}_2$, as imposed by the problem, which represents the change in the electron momentum. We are going to transform the summation into integration with the use of the common relationship $\sum \longrightarrow \frac{V}{(2\pi)^3}\int$ :

$$\left.\frac{df(\vec{k}_1)}{dt}\right|_{e-e} = \frac{2\pi}{\hbar}\frac{V^2}{(2\pi)^6}\iint d^3k_3 d^3k_2 \left|M(\vec{q})\right|^2 F(\vec{k}_1,\vec{k}_2,\vec{k}_3,\vec{k}_4)\delta(E_1+E_2-E_3-E_4) \qquad (5\text{-}28)$$

Assuming a parabolic conduction band: $E_i = \frac{\hbar^2}{2m}k_i^{\ 2} \Rightarrow \frac{dE_i}{d(k_i^{\ 2})} = \frac{\hbar^2}{2m}$ and making use of the *δ*-function properties, **Eq. 5-28** can be reduced to: **Snoke, Voisin2, DelFatti**

$$\left.\frac{df(\vec{k}_1)}{dt}\right|_{e-e} = \frac{V^2 m^3}{\hbar^7 2^3 \pi^3 k_1}\int dE_2 dE_3 F(\vec{k}_1,\vec{k}_2,\vec{k}_3,\vec{k}_4)\int_{q_{\min}}^{q_{\max}} dq\left|M(\vec{q})\right|^2 \qquad (5\text{-}29)$$

with:

$$\begin{cases} q_{\max} = \min\{(k_2+k_4);(k_1+k_3)\} \\ q_{\min} = \max\{|k_2-k_4|;|k_1-k_3|\} \end{cases} \qquad (5\text{-}30)$$

So, the problem is reduced in determining the proper interaction matrix and solving **Eq. 5-29**.

The interaction matrix has the form: $|M|^2 = \left|\left\langle \vec{k}_3,\vec{k}_4\left|\Phi\right|\vec{k}_1,\vec{k}_2\right\rangle\right|^2$. The tensor *Φ* is the interaction potential and in this circumstance it is a Coulomb potential reduced however, by screening, taking the form: **Kittel**

$$\Phi(r) = \frac{e}{4\pi\varepsilon_0\varepsilon}\frac{e^{-k_S r}}{r} \qquad (5\text{-}31)$$

where $k_S$ is the characteristic screening wavenumber that corresponds to the inverse screening length. In the ***k***-space, the above potential is Fourier-transformed to take the form:

$$\tilde{\Phi}(\vec{k},\omega) = \frac{e^2}{\varepsilon_0 \varepsilon(\vec{k},\omega)} \frac{1}{k^2 + {k_S}^2} \tag{5-32}$$

so that the interaction matrix becomes: **Snoke, Voisin2**

$$\left| M(q) \right|^2 \propto \left( \frac{e^2}{\varepsilon_0 \varepsilon_0^{ib} V} \frac{1}{q^2 + {q_S}^2} \right)^2 \tag{5-33}$$

where $q_S$ is a quantity that controls the magnitude of the Coulomb screening, V is arbitrary volume and $\varepsilon_0^{ib}$ is the static interband dielectric constant (see APPENDIX). Adjusting only the parameter $q_S$, it is possible through numerical calculations, as will be shown in **Chap. 6**, to numerically reproduce the electron internal thermalization and thus show that it can be described by an increased screening due to confinement.

However, we can move one step further. An approximate analytic expression for the $\left. \frac{df(\vec{k}_1)}{dt} \right|_{e-e}$ can be found when assuming the following approximations:

- First: That the two electrons that are subject to scattering between each other begin and arrive from and to states with energy close to the Fermi energy:

$$E_1 \approx E_2 \approx E_3 \approx E_4 \approx E_F \tag{5-34}$$

- Second: That the second term in the expression for $F$ is neglected so that only scattering events that lead to departure from the state $k_1$ are taken into account and that repopulation of this state is neglected:

$$F = -F_- + F_+ \approx -F_- = -f(\vec{k}_1)f(\vec{k}_2)\left[1 - f(\vec{k}_3)\right]\left[1 - f(\vec{k}_4)\right] \tag{5-35}$$

The characteristic electron-electron scattering rate can thus be shown to be: **Voisin2, DelFatti, Ogawa, Voisin3**

$$\gamma_{e-e}(E) \propto \left(E - E_F\right)^2 n_c^{-5/6} \varepsilon_0^{ib^{-1/2}} \tag{5-36}$$

where $n_c$ in the electron concentration of the conduction band and $\varepsilon_0^{ib} = \varepsilon^{ib}(\vec{q}, \omega = 0)$ (see APPENDIX) is the static interband dielectric constant that involves transitions from the d-bands towards the conduction band. This formula first indicates that the electron-electron scattering rate is proportional to the square of the difference of their energy from the Fermi energy. Thus, electrons excited higher in the conduction band are subject to stronger and faster scattering. Second, and more important for the purposes of this work, the electron scattering rate depends on both the conduction band electron density and the static interband dielectric constant. These last parameters, in usual cases are considered to be space invariant and constant throughout the bulk metal and thus are usually treated as “hidden” in the proportionality factor. However, in our case, as we will see in **Chap. 6**, these two parameters are of crucial importance because in contrast to the bulk, these parameters are not constant at all near the surfaces of the nanoparticles but exhibit a space-dependent variance. (This fact is true even for the bulk case near the surfaces of the metal).

As for the electron-phonon interaction, the evaluation of the second term of the Boltzmann equation can also be treated but it is not going to concern us here since this is not the main goal of the experiments presented in **Chap. 6**.

# APPENDIX

In the Drude model, the dielectric constant is described by:

$$\varepsilon(\omega) = 1 - \frac{\omega_p^{\ 2}}{\omega(\omega + i\gamma)}$$

where $\omega_p = \frac{ne^2}{\varepsilon_0 m}$ is the plasma frequency and $\gamma = \frac{1}{\tau}$ is the optical scattering rate. In general, it is frequency dependent: $\tau(\omega)$, and it involves a three body interaction i.e. photon-electron-phonon or photon electron-electron.

However, the Drude model can only describe intraband procedures. So, a quantum approach is more appropriate in order to take into account the interband procedures as well. Under a quantum description, the dielectric constant is given by: **Ziman**

$$\varepsilon(\vec{q},\omega) = 1 - \frac{e^2}{q^2\varepsilon_0} \sum_{\vec{k},n,n'} \left| \left\langle \vec{k} + \vec{q}, n' \right| e^{i\vec{q}\cdot\vec{r}} \left| \vec{k}, n \right\rangle \right|^2 \frac{f(\vec{k},n) - f(\vec{k}+\vec{q},n')}{E_{\vec{k},n} - E_{\vec{k}+\vec{q},n'} + \hbar\omega - i\hbar\alpha}$$

where $\alpha$ is defined in the formula that gives the change in the potential energy for the electrons when illuminated by an electromagnetic wave:

$$\delta U(\vec{r},t) = Ue^{i(\vec{q}\cdot\vec{r}-\omega t)}e^{-\alpha t} + c.c.$$

The interband contribution to the dielectric constant is obtained if we suppose that the arrival and destination bands are distinct:

$$\delta\varepsilon^{ib}(\omega,\vec{q}) = -\lim_{\alpha\to 0} \frac{e^2}{q^2\varepsilon_0} \sum_{\vec{k},n,n'} \left| \left\langle \vec{k} + \vec{q}, n' \right| e^{i\vec{q}\cdot\vec{r}} \left| \vec{k}, n \right\rangle \right|^2 \frac{f(\vec{k},n) - f(\vec{k}+\vec{q},n')}{E_{\vec{k},n} - E_{\vec{k}+\vec{q},n'} + \hbar\omega - i\hbar\alpha}$$

The intraband (*n*=*n'*)contribution to the dielectric constant is given by:

$$\varepsilon^{intra}(\omega,\vec{q}) = 1 - \frac{e^2}{q^2 V\varepsilon_0} \sum_{\vec{k}} \frac{f(\vec{k}) - f(\vec{k}+\vec{q})}{E_{\vec{k}} - E_{\vec{k}+\vec{q}} + \hbar\omega - i\hbar\alpha}$$

So, the total dielectric constant becomes:

$$\varepsilon(\omega,\vec{q}) = \varepsilon^{intra} + \delta\varepsilon^{ib}$$

For the optical frequencies that we are interested in this work, i.e. $\omega >> \gamma$ the last formula becomes approximately:

$$\varepsilon^{intra}(\omega,\vec{q}) = 1 - \frac{\omega_p{}^2}{\omega^2}$$

which is similar to the expression given by the Drude model.

So, for the optical wavelengths that are used in this work we approximate the intraband contribution with the results of the classical Drude model:

$$\varepsilon^{intra} = \varepsilon^{f} = 1 - \frac{\omega_p{}^2}{\omega(\omega + i\gamma)}$$

and the total dielectric constant of the metal can be written as ($\omega >> \gamma$):

$$\varepsilon = \varepsilon_1 + i\varepsilon_2 \text{, with: } \varepsilon_1 = 1 - \frac{\omega_p{}^2}{\omega^2} + \delta\varepsilon_1{}^{ib} = \varepsilon_1{}^{ib} - \frac{\omega_p{}^2}{\omega^2} \text{, and: } \varepsilon_2 = \frac{\omega_p{}^2}{\omega^3}\gamma + \delta\varepsilon_2{}^{ib}$$

## 5.5 References

**DelFatti** N. Del Fatti, C. Voisin, M. Achermann, S. Tzortzakis, D. Christofilos, and F. Vallee, Phys. Rev. B **61**, 16956 (2000).

**Elements** Periodic Table of Elements.

**Genzel** L. Genzel, T. P. Martin, U. Z. Kreibig, Phys. B **21**, 339 (1975).

**Halperin** W. P. Halperin, Rev. Mod. Phys. **58**, 533 (1986).

**Kawabata** A. Kawabata, R. J. Kubo, Phys. Soc. Jpn. **21**, 1765 (1966).

**Kittel** C. Kittel, Introduction to Solid State Physics, J. Wiley & Sons Inc.

**Ogawa** S. Ogawa, H. Hagano and H. Petek, Phys. Rev. B 55, 10869 (1997).

**Papaconstantopoulos** D. A. Papaconstantopoulos, Handbook of The Band Structure Of Elemental Solids, Plenum Press, New York (1986).

**Seeger** K. Seeger, Semiconductor Physics, in Solid-State Sciences, Springer.

**Snoke** D. W. Snoke, W. W. Ruehle, Y.-C. Lu, and E. Bauser, Phys. Rev. B **45**, 10979 (1992).

**Voisin** C. Voisin, N. Del Fatti, D. Christofilos, and F. Vallee, J. Phys. Chem. B **105**, 2264 (2001).

**Voisin2** C. Voisin, D. Christofilos, N. Del Fatti, F. Vallee, B. Prevel, E. Cottancin, J. Lerme, M. Pellarin, and M. Broyer, Phys. Rev. Lett. **85**, 2200 (2000).

**Voisin3** C. Voisin, PhD Thesis presented in Universite Paris XI Orsay, January 5, 2001.

**Ziman** J. M. Ziman, Principles of the Theory of Solids, Cambridge University Press.

# Chapter 6 Au Nanocrystals: Electron Dynamics

## 6.1 Introduction

Composite materials containing metallic systems confined in nanoscale dimensions are a current subject of intensive research. The interesting optical properties of such systems due to their reduced dimensionality give rise to potential applications in the optoelectronic industry. Therefore, research is needed in order to understand the mechanisms that are responsible for the optical properties.

One field of growing interest is the dynamic behavior of these systems that follows their excitation by ultrafast light sources. The evolution of the perturbed system back towards its equilibrium can be roughly separated in three regimes:

- the initial electron-electron interaction

- electron-phonon interaction
- phonon-host interaction.

Although the electron-phonon and phonon-host interactions have been extensively investigated, **Perner, Perner2, Hamanaka, Zhang, Nisoli, Roberti, Inouye, DelFatti, DelFatti2, Hodak, Smith, Smith2, Hodak2, Halte, Link, Link2, Stella, Tokizaki, Logunov, Ahmadi** reports on the initial electron-electron interaction in metallic nanoparticles are rather scarce **Stella, DelFatti2, Link, Link2, Perner2, Bigot** and the dependence of this mechanism to the dimensionality of the system in not yet clear. It is only recently that a report appeared in the literature giving the dependence of the internal electron thermalization dynamics with respect to the size for silver (Ag) nanoparticles. **Voisin, Voisin2** Since there are no other reports for the internal electron thermalization trend, it is very important to perform similar experiments in other noble metals as well, like Gold (Au), in order to investigate if the trend is similar.

In this chapter, the reader can find the experimental details of the study on the ultrafast electronic behavior of Au samples that are confined to nanometer dimensions. Our goal here is to analyze the effect of size reduction on the electronic interactions in Au nanoparticles, and in particular to investigate the transition from a bulk like behavior to a strongly confined material. Metal nanoparticles in general and Au nanoparticles in particular constitute an interesting type of material since, in contrast to semiconductors, quantum confinement effects are relatively weak even for few nanometer nanoparticles. **Voisin** The impact of confinement on the electronic interactions can thus be introduced as correction to the bulk properties. The electron-electron interactions lead to energy exchanges between electrons and are responsible for the establishment of an electron temperature. They can thus be monitored by analyzing the internal thermalization of the metal conduction electrons after perturbation of their distribution by a fs pulse. The electron-phonon interaction leads to electron-lattice energy redistribution and can thus be followed by monitoring the electron-energy losses to the lattice.

The sample preparatory conditions are mentioned in the beginning of the chapter. The ultrafast behavior of the thermalized and the nonthermalized electron population is then studied and a model is presented that describes the experimental measurements and explains the procedures that lead the nonthermal electron population towards internal thermalization.

## 6.2 Sample Preparation

The samples that are studied in this chapter are divided in two categories: the alumina-matrix-deposited samples and the colloidal solution samples. All samples are comprised of metallic clusters with nanometer dimensions and as can be verified by x-ray diffraction measurements they are single-crystalline. **Uchida** Their size distribution is measured with Transmission Electron Microscopy (TEM). More information about this characterization method can be found in **Chaps. 2&4**.

The alumina-matrix-based samples are fabricated by the Laboratoire de Spectroscopie Ionique et Moleculaire (M. Broyer, M. Gaudry, E. Cottancin and M. Pellarin) and the Departement de Physique des Materiaux (B. Prevel) de l' Universite de Lyon I. The samples are obtained by co-deposition of the clusters and the matrix on a suprasil (fused silica) substrate. **Milani, Vialle, Perez** The metal is vaporized by a focused laser beam on a barrel of Au. The condensation occurs in an atmosphere of a rare gas. The temperature and the pressure determine the average size of the particles and their distribution. At the exit of the chamber, this gas plays the role of the gas that carries and allows one directional cluster jet. If the energy (velocity) of the cluster is sufficiently

| Sample code name | Radius (nm) |
|---|---|
| | |
| Au film | 27 |
| Au colloid R=10 nm | 10 |
| Au colloid R=5 nm | 5 |
| Au colloid R=2.5 nm | 2.5 |
| AuAlDyn4-sup | 1.7 |
| AuAlDyn2 | 1.125 |
| AuAlDyn2bis | 1.125 |
| AuAlDyn1bis | 1.075 |
| AuAlFI | <1 |

**Table 6-1** The code names for all the used samples and their corresponding radii in nm.

weak, the deposition on the substrate occurs without destruction of the cluster and the clusters obtained during the phase of condensation will be re-obtained as they are on the substrate (method LECBD: Low Energy Cluster Beam Deposition).

The matrix ($Al_2O_3$ or $MgF_2$ for the samples we have investigated) is vaporized by bombardment of a target with the help of a beam of electrons and is deposited simultaneously with the clusters. This method provides the samples whose matrix is the more often porous, which introduces an inhomogeneous dispersion of the optical characteristics. This method of evaporation and condensation does not permit the production of clusters of big sizes; the mean radii are of 1 and 3 nm with a dispersion on the size of the order of 10%.

The colloidal specimens of Au are commercially available (Sigma). These are the aqueous solutions of the Au nanoparticles whose mean radii are in the range of 2.5 and 10 nm. The dispersion of the sizes varies between 7 % and 10 %. The particles are surrounded by molecules of the tensioactive of the nature non indicative to assure their stability (avoiding aggregation of the particles). [Roth]

Typical value for the volume fraction $p$ of the samples is $p=10^{-3}$.

The samples used in this chapter are listed in **Tab. 6.1**.

## 6.3 The pump – probe experiment

The technique used to study the ultrafast electron dynamics in Au nanocrystalls is shown in **Fig. 2-14**. It is a differential pump-probe transient setup. The pump pulse excites a population of electrons at time *t=0*. The definition of time *t=0* is chosen as the instant of the perturbation. The main differences of this setup with respect to the one used in **Chap. 4** is first the use of the reference beam for better signal to noise contrast and second the difference in the wavelengths of the pump and the probe beams. The reader must always have in mind that the choice of the word "instant" is rather tricky. It would be absolutely justified only in the case that the laser pulse time profile would be a $\delta$-function in time. Typical values for the laser CW power is about 30 mW for the pump beam and 100 μW for the second-harmonic probe beam. The laser spot diameter has a typical value of 50 μm at the focus (for the IR-beam). The wavelength regime that is used ranges from 930 nm – 1070 nm for the infra-red beam and the second harmonic frequencies for the probe beam.

### 6.3.1 Typical measurements and phenomenological description

A typical measurement is shown in **Fig. 6-1**. The cross-correlation (CC) of the two pulses is also plotted. Time *t=0* coincides with the peak value of the CC curve which is assumed to have instantaneous response to the laser pulse and is the "instant" of perturbation. As can be observed the

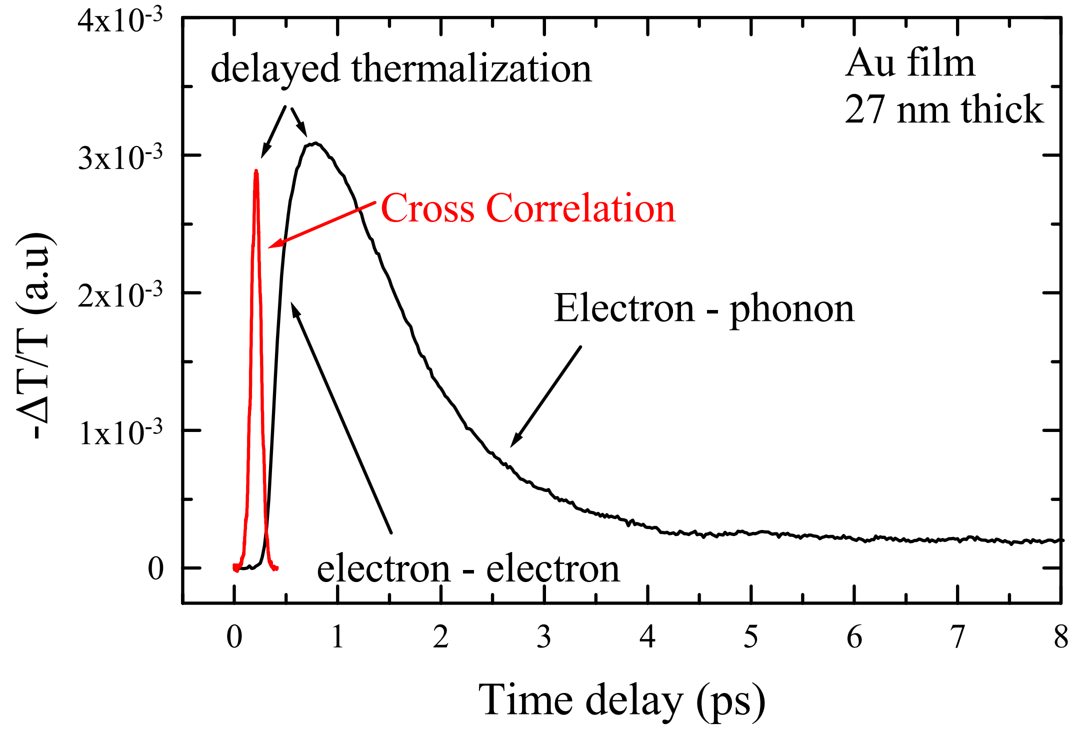

**Figure 6-1** Typical transient transmission spectrum of an Au thin film. The CC curve is also shown.

peak signal is shifted towards greater time delays with respect to the CC curve. This is a result of the slower rise of the signal with respect to the CC, which follows exactly the laser pulse time profile. This delayed rise of the signal has been observed previously in bulk noble metals, [Schoenlein] and has been attributed to the noninstantaneous internal thermalization of the initial athermal electron population. [Fann, Fann2, Sun, Sun2, DelFatti3, DelFatti4] The signal at longer time delays "slowly" decays and reflects the relaxation of the energy (temperature) of the thermalized electron population towards the lattice background value. [Schoenlein, Fann, Fann2, Sun, Sun2, DelFatti3, DelFatti4]

In order to interpret the observed behavior of the signal, a phenomenological model has been utilized. This model has been used with success to describe the same procedures in bulk metals. [Sun2] Three distinct deposits of energy have been considered and are depicted in **Fig. 6-2**:

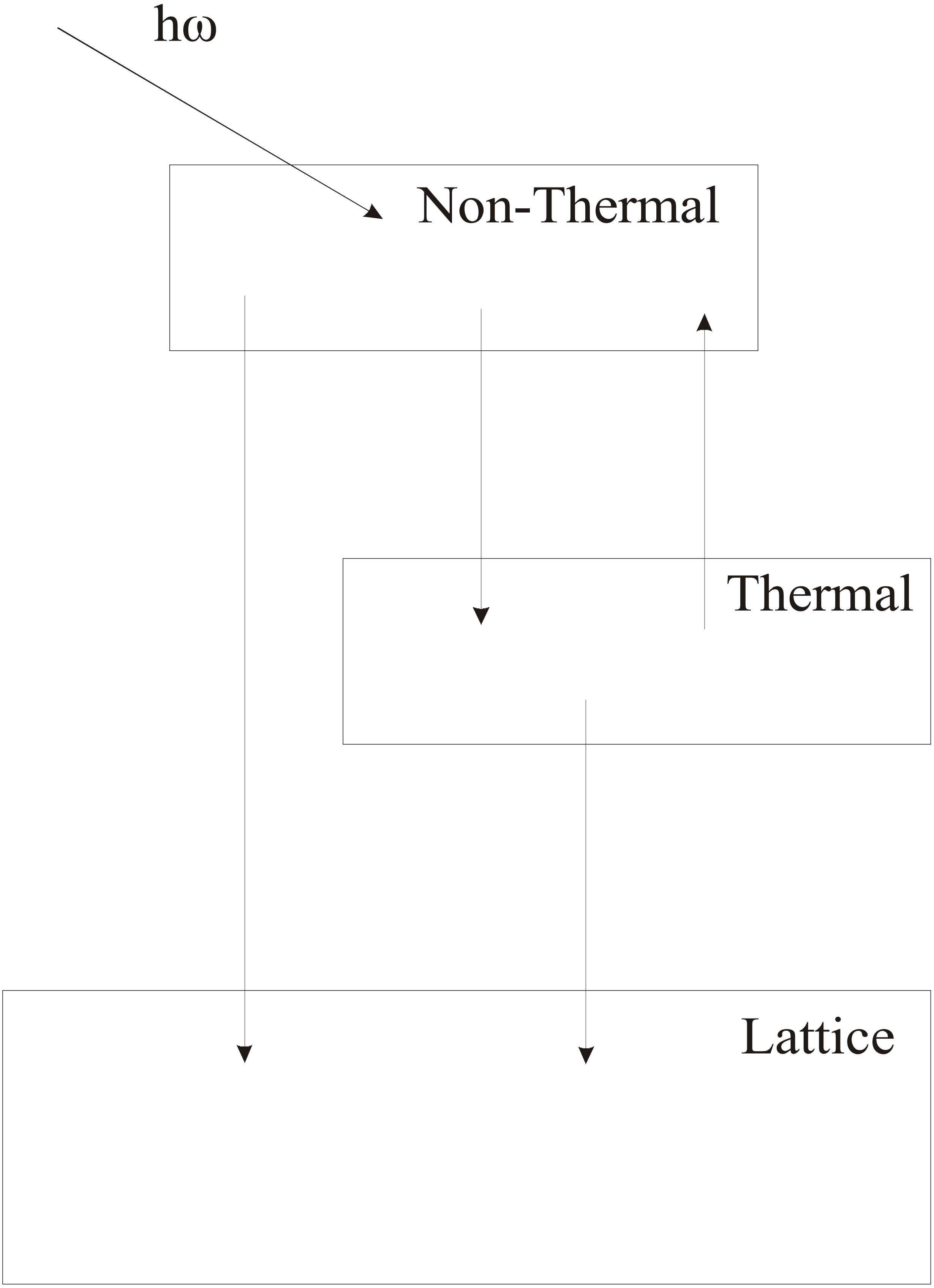

**Figure 6-2** The phenomenological model used to interpret the interactions in the system; we assume three deposits: the athermal and the thermalized electron population and the lattice.

- The first one is the initial athermal or non-thermal electron population. This is the initial stage of the metallic system immediately after the excitation. All the absorbed energy from the laser pulse is initially stored in this deposit.

- The second one is the electron population that follows a Fermi-Dirac distribution. This is the second stage of the metallic system after the excitation. The temperature that characterizes this Fermi-Dirac distribution corresponds to the excess energy of the electrons out of their equilibrium state that has been gained by the absorption of the infra-red (pump) laser pulses.

- The third deposit is the lattice. This is the third and last stage of the metallic system evolution in the means that all the externally injected energy is finally after a long time period stored here.

The phenomenological model described above introduces distinct deposits although this is not exactly true. The first two deposits, namely the athermal electron population and the thermalized electron distribution are not separated in space at all. They can be considered distinct in the sense that the first one cannot be characterized by a certain energy or temperature and not even by a certain momentum as in semiconductors (in contrast to interband absorption like in LTG-GaAs or LTG-AlGaAs, the momentum here is lost in intraband absorption because it is assisted by a phonon: so the momentum information disappears). They correspond to the initially excited electrons. This fraction of electrons is very small (typically in bulk metal $<10^{19}$ compared to the total $\sim 6\times10^{22}$ cm$^{-3}$) and as a first approximation, their number can be neglected and they can be considered as an energy reservoir, i.e., only the energy flow to the second type of electrons (majority electrons) is considered, their number being assumed constant. This is a way to mimic energy storing and delayed heating: energy is first given to few electrons by the pump pulse and slowly redistributed to the others.

The second deposit is characterized by a certain temperature and their distribution, namely the number of electrons vs. temperature (occupation number) follows the Fermi-Dirac law (**Eq. 5-3**):

$$f(E) = \frac{1}{e^{\frac{(E-E_F)}{k_B T}} + 1}$$

where $k_B$ is the Boltzmann constant, $T$ the temperature of the electronic gas and $E_F$ the Fermi energy.

The above described deposits do not evolve independently. They interact starting from time zero, i.e. the “instant” of the initial perturbation by the laser pulse. The following are the interactions between these three deposits as are also shown with arrows in **Fig. 6-2**:

- The first deposit (the non-thermal electron population) gains energy only from the laser pulse. It loses energy with a rate $\alpha$ towards the second deposit (the thermalized electron distribution) via electron-electron scattering. It also loses energy with a rate $\beta$ towards the third deposit (the lattice) via electron-phonon interaction.

- The second deposit (the thermalized electron distribution) can be characterized by a temperature $T_e$. It gains energy only from the first deposit as already mentioned. It loses energy only towards the third deposit with a rate $G$, via electron-phonon interactions.

- The third deposit (the lattice) does not lose any energy since this is the final and most capacive deposit of the metallic system. It only gains energy from both the first and second deposits as previously mentioned. This leads to electron-lattice thermalization at a higher temperature than the initial one. The temperature rise of the thermalized system is however small (about 1 K) since the lattice heat capacity is much larger than the electron one (about 100 times). Actually, the excited metal returns to its initial temperature by losing energy to the surrounding matrix (nanoparticle case) or by heat diffusion to the substrate (film case) but on a very long time scale (typically 100 ps **Ahmadi**). This is why we are neglecting this effect here.

In mathematical form, all the above can be described by the following set of three coupled equations: **Sun2**

$$\begin{aligned} \frac{\partial N}{\partial t} &= -\alpha N - \beta N \\ C_e \frac{\partial T_e}{\partial t} &= -G(T_e - T_l) + \alpha N \\ C_l \frac{\partial T_l}{\partial t} &= G(T_e - T_l) + \beta N \end{aligned} \qquad (6\text{-}1)$$

where $N$ is the initial non-thermal electron population (energy density stored in the nonthermalized part of the electron population), $\alpha$ is the rate of the loss of electrons from the first deposit towards the second deposit, $\beta$ is the rate of the loss of electrons from the first deposit towards the third deposit, $C_e$ and $C_l$ are the electronic and lattice heat capacities respectively, $T_e$ and $T_l$ are the electronic and lattice temperatures respectively and $G$ is the rate of loss of energy (temperature) from the second towards the third deposit. The heat capacities as a first approximation are considered not to significantly vary and be almost equal to their values for T=300 $^{o}$K, since the temperature changes that are induced by the laser pulses in our experiment is of the order of $\Delta T_e^{me}$~50 $^{o}$K for a particle size $R$=3 nm.

The gain of energy of the first deposit is omitted deliberately as can be seen by the first equation. It is omitted here in order to make calculations simpler but it is going to be introduced appropriately later (with the convolution of the system response function with the CC of the laser pulses; see also **Chap. 2**, **Eq. 2-6**).

The solution of the above system of coupled differential equations for *N* and $\Delta T_e$ is:

$$\begin{aligned} N &\propto \Theta(t) e^{-\frac{t}{\tau_{th'}}} \\ \Delta T_e &\propto \Theta(t)\left(1 - e^{-\frac{t}{\tau_{th}}}\right) e^{-\frac{t}{\tau_p}} \end{aligned} \qquad (6\text{-}2)$$

where *Θ(t)* is the Heaviside function, $\frac{1}{\tau_{th}} = \alpha$, $\frac{1}{\tau_p} = \beta$, $\frac{1}{\tau_{th'}} = \alpha + \beta$.

Now, we assume for the system response function to be the sum of the non-thermalized part and the thermalized Fermi-Dirac part: **Sun2**

$$\frac{\Delta T}{T}(\hbar\omega) = \Theta(t)\left[\left.\frac{\Delta T}{T}(\hbar\omega)\right|_{NT} e^{-\frac{t}{\tau_{th'}}} + \left.\frac{\Delta T}{T}(\hbar\omega)\right|_{Th}\left(1 - e^{-\frac{t}{\tau_{th}}}\right) e^{-\frac{t}{\tau_p}} + \left.\frac{\Delta T}{T}(\hbar\omega)\right|_{L}\right] \qquad (6\text{-}3)$$

The third part of **Eq. 6-3** is introduced to account for the slight heating of the lattice, i.e., relaxation of the system to a slightly different state than before the external perturbation by the laser source. The labels *NT*, *Th* and *L* correspond to the solutions for the non-thermal population, the thermalized electron distribution and the introduced different relaxation state respectively.

**Eq. 6-3** describes the response of the metallic system after the "instant" of the perturbation by the laser pulse. However, since the laser pulse is not finite, the word "instant" is rather tricky in describing the duration of the perturbation. Therefore, one also needs to introduce the laser pulse duration in describing the signal function. With the above in mind, the signal function $\frac{\Delta T}{T}$ is the convolution of the response function of the sample with the CC of the laser pump and probe pulses, and can be calculated to be (see also **Eq. 2-6**):

$$
\begin{aligned}
&Signal(t) = \\
&Ae^{-\left(\frac{1}{\tau_{th}}+\frac{1}{\tau_p}\right)t}\left[1+Erf\frac{t-w^2\left(\frac{1}{\tau_{th}}+\frac{1}{\tau_p}\right)}{\sqrt{2}w}\right]+ \\
&Be^{-\frac{t}{\tau_p}}\left(1+Erf\frac{t-\frac{w^2}{\tau_p}}{\sqrt{2}w}\right)+ \\
&C\left(1+Erf\frac{t}{\sqrt{2}w}\right)
\end{aligned}
\qquad (6\text{-}4)
$$

where $w$ is a constant that is related to the width of the laser pulse and is (see **Eq. 2-18**):

$$w = \frac{T}{\sqrt{2\ln 2}} \qquad (6\text{-}5)$$

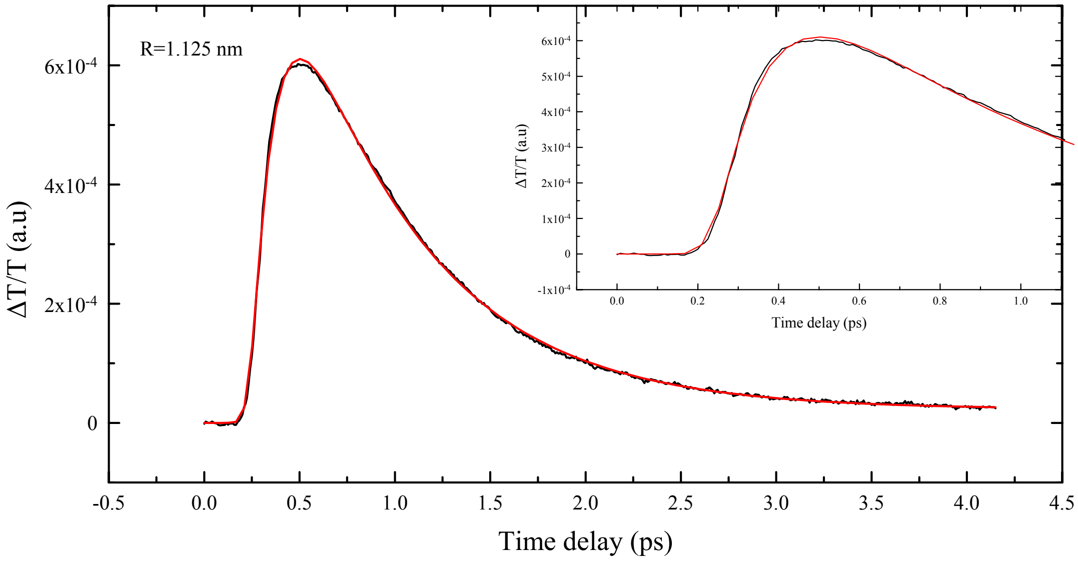

**Figure 6-3** A typical $\frac{\Delta T}{T}$ for an Au nanoparticle of radius $R$=1.125 nm. The curve fitting is produced by the phenomenological model. Inset shows the good reproducibility of the experimental data in an early time-window.

and is separately measured by a CC of the pump and probe pulses. $A$, $B$ and $C$ are constants.

The above function is used to reproduce the transient pump-probe spectra of all the measured samples. The good fit of the above model to the data is based on the good definition of parameters $w$ and $\tau_p$. Parameter $\tau_p$ which represents the characteristic electron-phonon interaction time or energy decay time is also measured separately, as shown in the next paragraph. Both parameters $w$ and $\tau_p$ are held fixed during the reproduction of the data with the function of **Eq. 6-4** so that the only parameter to be extracted by the fitting procedure apart from the constants $A$, $B$ and $C$ is the characteristic internal electron thermalization time $\tau_{th}$. The good reproduction with the use of the above considerations is shown in **Fig. 6-3**.

### 6.3.2 Electron-lattice thermalization: Results

We are first going to discuss the electron-phonon interaction (electron-lattice energy exchange) that takes place in the nanoparticle Au systems. This interaction is monitored by the late stages of the signal where it “slowly” decays to the background value. Although this mechanism takes place in the late stages of light and nanoparticle interaction, being responsible for the signal decay, we are going to discuss it first because the characteristic decay times are the first to be extracted in the signal analysis procedure and used in order to move on to the extraction of the electron internal thermalization times (delayed signal rise). The wavelengths used for pumping the samples range from 930 nm to 1070 nm. The wavelengths used to probe the induced changes in the optical and electronic properties of the samples are the second harmonic frequency of the pump

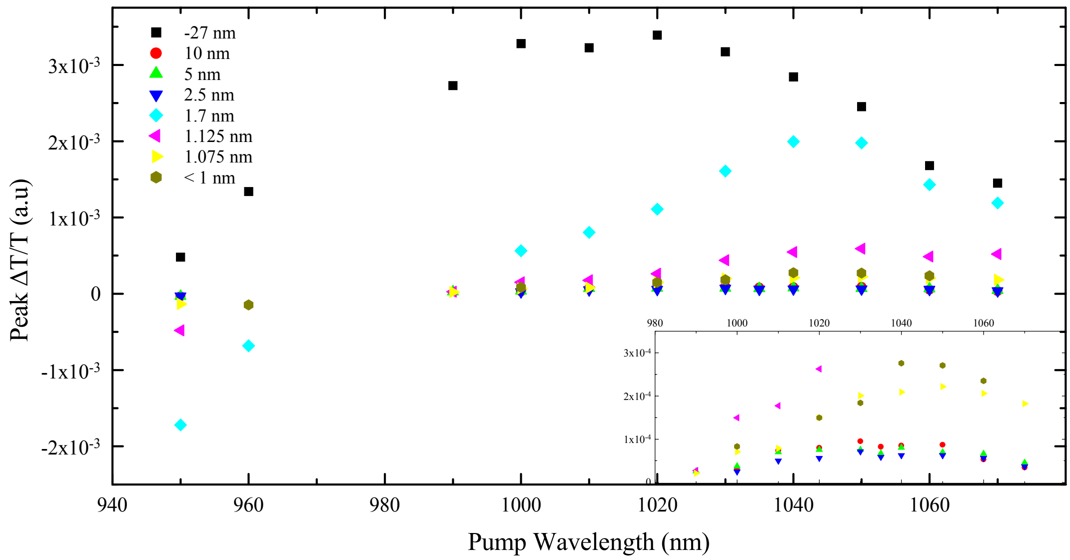

**Figure 6-4** The peak $\frac{\Delta T}{T}$s for all the used sizes with respect to the laser wavelength.

beam, thus ranging from 465 nm to 535 nm, a region that contains the characteristic frequency of the SPR which is about 520 nm (with small deviations depending on the size of the particle).

In **Fig. 6-4** the peak signal versus pump wavelength for all samples is plotted. Depending on the size of the nanoparticles, the peak signal appears at different wavelengths depending on the position of the SPR. The thin film sample with a width of 27 nm exhibits its peak signal at 1020 nm pump wavelength while all the other samples with radii from <1 nm up to 10 nm exhibit their peak signals at 1040 nm – 1050 nm pump wavelength or 520 nm – 525 nm of the probe wavelength, that is in the vicinity of the SPR wavelength for each nanoparticle. This is a consequence of resonance enhancement of the optical nonlinear response around the SPR frequency in the nanoparticle systems. [Flytzanis]

The characteristic decay (as well as rise times, shown later) of the electronic population for each sample are measured at all wavelengths. The more accurate measurements are performed at the vicinity of the SPR because of the higher signal. The characteristic energy decay times are measured in such time-windows so that only experimental data points about 0.5 ps – 1 ps after the peak of the signal are taken into account. This time-window is chosen in order to ensure that the only mechanism remaining is the electron-phonon interaction and that contributions from the electron-electron interaction convolved with the laser pulse CC are minimized. If the electron-phonon mechanism is the only one to be present, then the transient transmission spectra should exhibit a single exponential behavior. In **Fig. 6-5** a ln-linear plot of one transient transmission spectrum is shown. As can be seen, the behavior of the signal becomes single-exponential after about 1 ps from the peak and this is the time window from which the characteristic electron-phonon interaction times are obtained either by linear fitting in a ln-linear plot or by a single-exponential

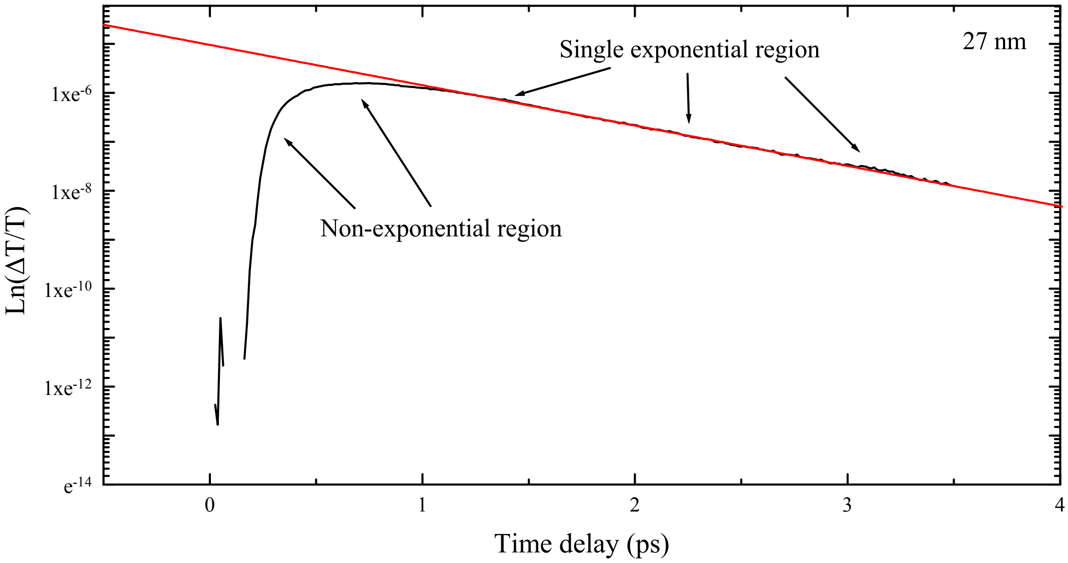

**Figure 6-5** The single-exponential region of the signal decay (after about 1 ps from the peak).

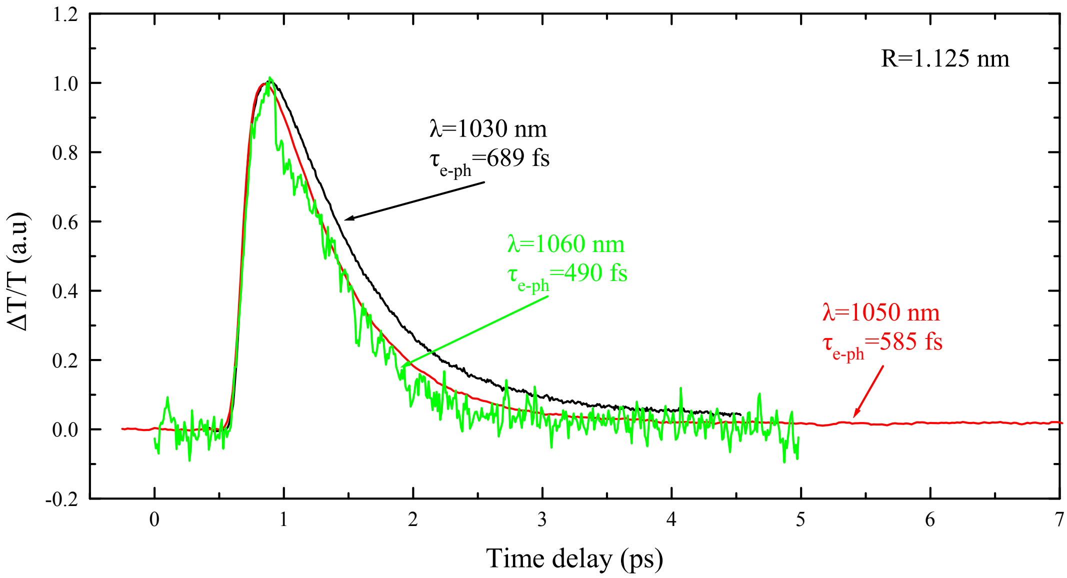

**Figure 6-6** Transient $\frac{\Delta T}{T}$s for an Au nanoparticle sample of $R$=1.125 nm at three different wavelengths.

fitting in a linear-linear plot.

The characteristic decay times which concern us in this paragraph, are found to vary with respect to the excitation and therefore the probing wavelength (since the probe $\lambda$ is the half of the pump). In **Fig. 6-6** transient spectra for the nanoparticle sample with radius $R$=1.125 nm are exhibited for three different wavelengths. The decay time constants are found to be 689 fs for 1030 nm, 585 fs for 1050 nm and 490 fs for 1060 nm. Thus, in order to obtain reliable conclusions about the relative decay rates for the electron-phonon interaction among all the samples, only measurements performed in the same wavelength are used, in order to make comparisons between every sample's electronic behavior.

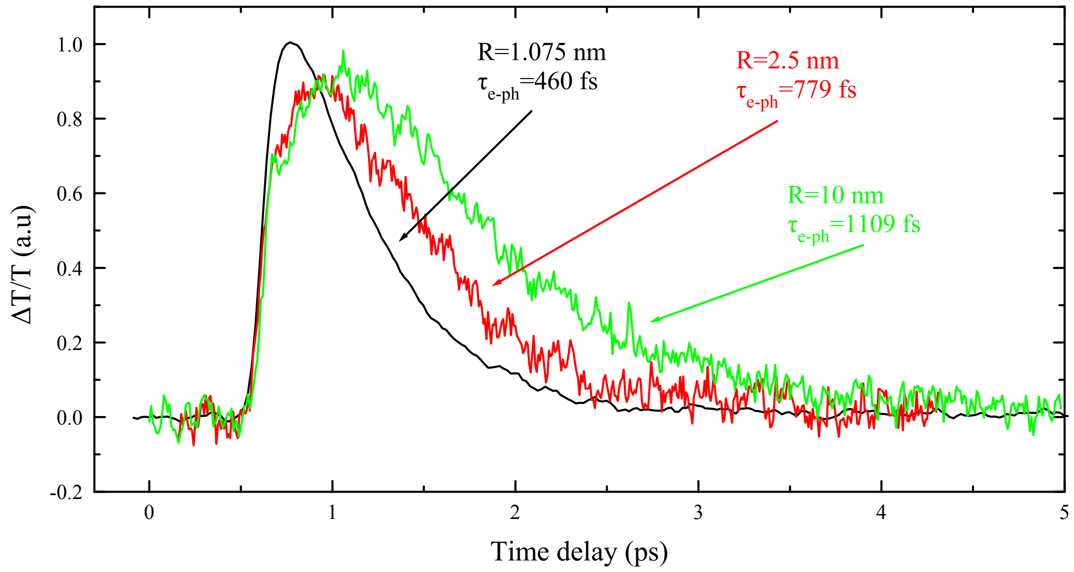

**Figure 6-7** Transient spectra of three different nanoparticle sizes at the SPR frequency $\Omega_R$ (same as threshold for interband transitions $\Omega_{ib}$).

In **Fig. 6-7** the signal of three samples with radii $R$=1.075 nm, $R$=2.5 nm and $R$=10 nm at their corresponding peak response wavelengths versus pump and probe time delay is plotted. The corresponding electron-phonon decay times are 460 fs, 779 fs and 1109 fs and can be clearly distinguished as can be seen by the different curvatures in the decay rates for times about 1 ps after the peak.

### 6.3.3 Electron-lattice thermalization: Discussion

By single exponential fits of the measurements at a relatively long time-window the electron-phonon interaction times are extracted. The results versus nanoparticle size are plotted in **Fig. 6-8**. As can be observed, the electron-phonon times are a rising function of the nanoparticle size. For relatively large nanoparticles, the electron-phonon time practically coincides with that of the bulk Au material. For the smaller particles there is a strong deviation of the bulk material (film) characteristic time. The trend that is observed is that the smaller the particle, the shorter the characteristic decay times.

The electron-lattice interaction and the concomitant thermalized electron cooling towards the lattice has been extensively investigated in the past. However, many problems still persist. First, there seems to be a strong dispersion in the absolute values reported by other groups. [Link, Link2, Zhang, Inouye] Second, there has been a debate in the literature on whether the thermalized electron-lattice dynamics are size dependent or not, [Link. Link2, Zhang, Smith2, Halte, Roberti] and if there exists a size dependence, what is the size range that it becomes considerable. Third, the electron-lattice cooling

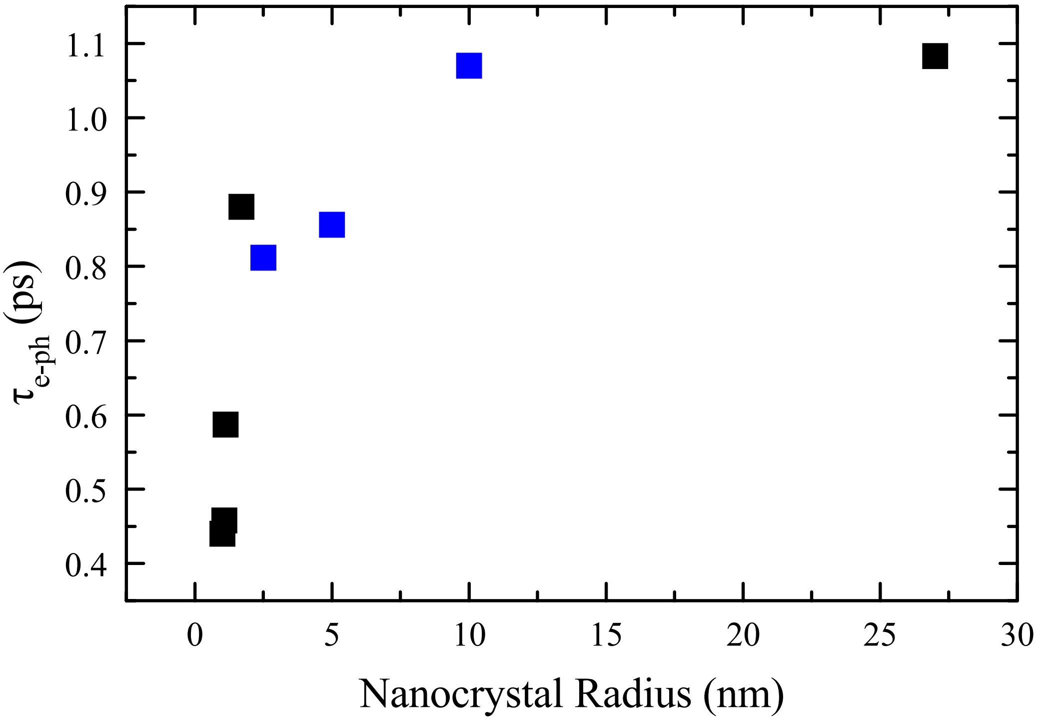

**Figure 6-8** The results for the electron-lattice thermalization times with respect to the nanoparticle radius. Blue corresponds to samples in a liquid dielectric host.

is depending on the excitation strength, [Hodak, Hodak2, Hamanaka, Halte, Tokizaki] a fact that is very important in investigating dynamical effects and one must be very careful with the manipulation of this parameter when comparing results obtained by various experiments. Lastly, it is also not clear if the environment affects the electron cooling dynamics. [Roberti, Nisoli]

In our experiment, the results show a clear modification of the electron-lattice cooling from the size of the nanoparticles for Au. The measurements are performed in the low-perturbation regime (as will be further analyzed later). Furthermore, our results for the measured times for both the nanocrystal environments show a consistency and thus the times seem to be independent of the nanoparticle environment (glass or ligand + water) showing that its dependence on the nanoparticle size is an intrinsic effect due to confinement. Its physical origin has not yet been elucidated, but is probably due to modification of the electron-ion interaction due to surface effect (similarly to the electron-electron case, shown later) and/or modification of the vibration spectrum. [Del Fatti, Nisoli]

A similar behavior to our experiments (Au) has been observed in Ag [Del Fatti, Halte] and Ga. [Nisoli] with the most extensive work in the Ag case where the size dependence of the electron-lattice dynamics becomes evident. That work is the only one in the literature that examines the dynamic behavior over a quite big range of nanoparticle sizes and environments in order to obtain the first unambiguous results in the literature, however only for Ag. Since this is the only work covering a big nanoparticle size range, there is still uncertainty for the noble metal nanoparticles in general and Au nanoparticles in particular. Thus, our results for the electron-lattice dynamics are of great value when used in addition with the previous results for Ag.

As will be shown later, these results exhibit a striking similarity with the results obtained for the electron internal thermalization dynamics versus the particle size. This fact suggests a confinement-induced acceleration of the electron-lattice mode coupling. However, the interpretation of the trend that is observed with respect to the nanoparticle size is still not clear.

For a more exact examination of the energy decay relaxation rate a degenerate pump probe setup would rather be more appropriate (degenerate means the same pump and probe wavelengths). The two infrared pump and probe beams would be far from the interband transition threshold, thus simplifying the interpretation of the results, the measured signal being then almost proportional to the energy stored in the electron gas.

### 6.3.4 Electron-electron thermalization: Results

The internal electron relaxation dynamics in a system out of equilibrium are procedures generally faster than the electron-phonon interaction. They are the first stages of the evolution of the electron population and therefore they contribute in the first temporal stages of the evolution of the

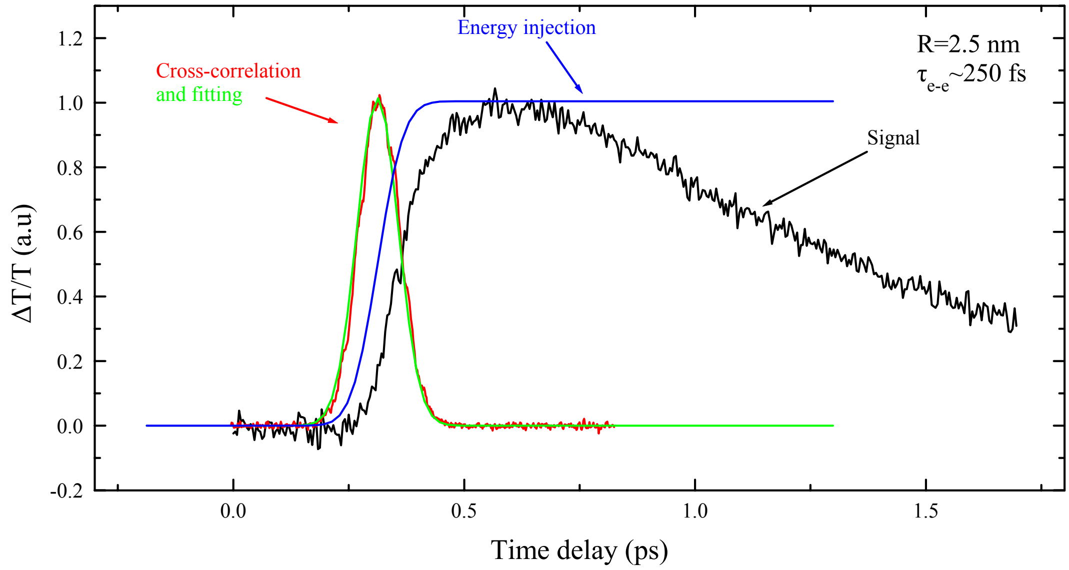

**Figure 6-9** Early stages of the signal evolution in an Au nanoparticle of *R*=2.5 nm. The CC curve and the energy injection curve are also shown for comparison.

signal function $\frac{\Delta T}{T}$. [Voisin, Voisin2] In order to reveal the early dynamics of the electron population, one has to obtain transient transmission spectra with the best possible temporal resolution of the experimental setup and to limit the time window of the measurements to small time-windows.

A typical transient transmission spectrum is shown in **Fig. 6-9**. The measured sample has a radius of 2.5 nm. For comparison, the CC curve of the pump and probe pulses and the energy injection from the laser source to the electron are also plotted in **Fig. 6-9**.

The behavior is observed more clearly if compared to the energy injection. As can be seen in **Fig. 6-9**, the rise of the signal is delayed with respect to that of the energy injection. As a consequence, the peak of the signal does not coincide in time with that of the energy injection curve but is positively shifted.

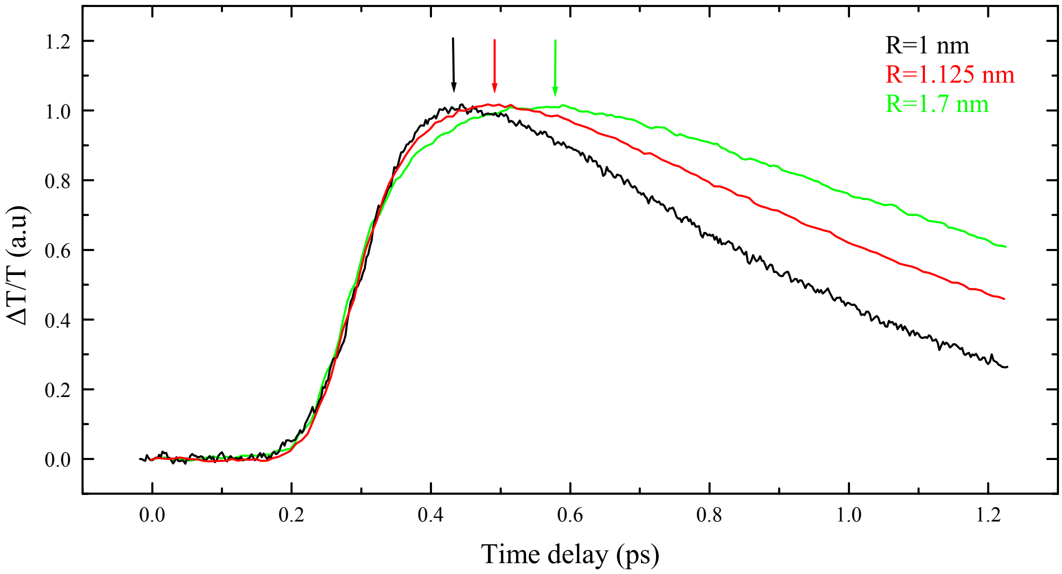

**Figure 6-10** Transient $\frac{\Delta T}{T}$s for 3 different Au nanocrystal sizes.

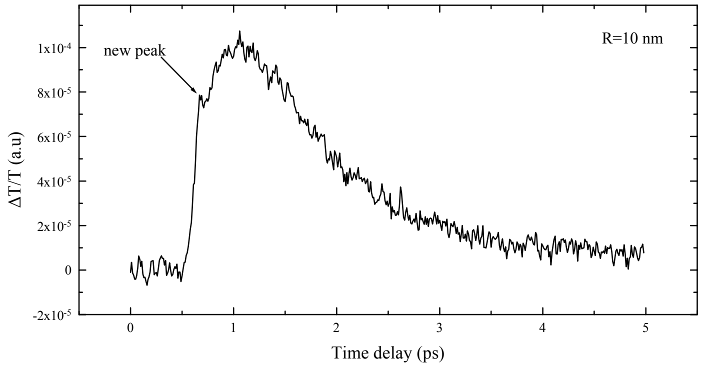

**Figure 6-11** A $\frac{\Delta T}{T}$ for a colloidal sample with *R*=10 nm.

The delay in the rise of the signal and the time-shifted peak with respect to the energy injection is a consequence of the delayed internal thermalization of the electron population in the nanoparticle. [Voisin, Voisin2] Energy redistribution among the electrons and the concomitant establishment of an electron temperature is due to the electron-electron Coulomb interactions. [Voisin] In contrast to semiconductors, where relatively low (photoexcited) carrier densities (< $10^{18}$ - $10^{19}$cm$^{-3}$) are considered and electron-electron scattering increases with electron density, the efficiency of the interactions in metals is strongly reduced by the very strong electron density (6 $10^{22}$ cm$^{-3}$ in Au).

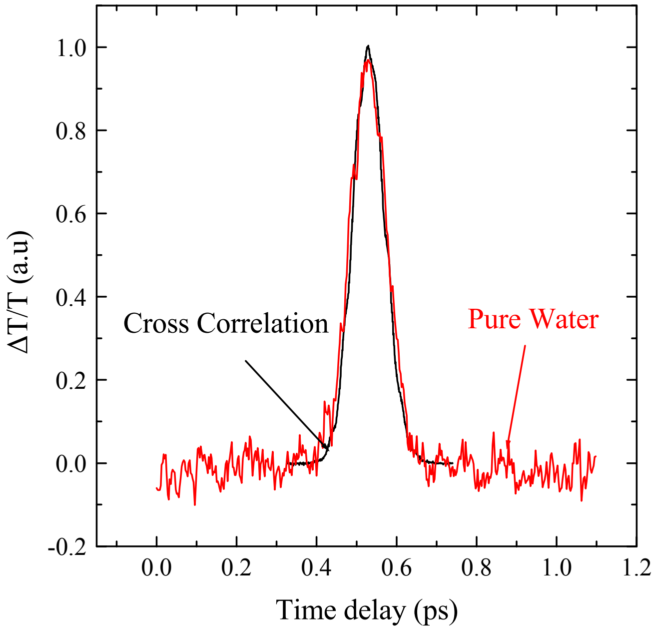

**Figure 6-12** $\frac{\Delta T}{T}$ for pure-distilled water, in which the nanocrystalls are dissolved, in comparison with the CC curve.

Transient transmission spectra obtained by measurements of three other samples with various radii are shown in **Fig. 6-10**. As can be observed, there is a clear variation of the signal rise rate and the time-position of the peak of the signal with the size of the nanoparticles. While the nanoparticle size becomes bigger, the signal rise rate becomes slower and the signal peak shifts to greater time delay values.

A typical transient transmission spectrum for a nanoparticle solution of radius *R*=10 nm, in a distilled water solution is shown in **Fig. 6-11**. The general behavior of the spectrum for this sample is the same as the one previously discussed for the samples that contained nanocrystals embedded in solid matrices. Apart from this general trend, there is a new, interesting feature observed for the colloidal sample. A new very transient peak is clearly observed. This transient peak is always observed in the left of the signal peak. In order to locate and interpret the origin of this new transient peak, transient transmission spectra are obtained for a sample of pure distilled water. The

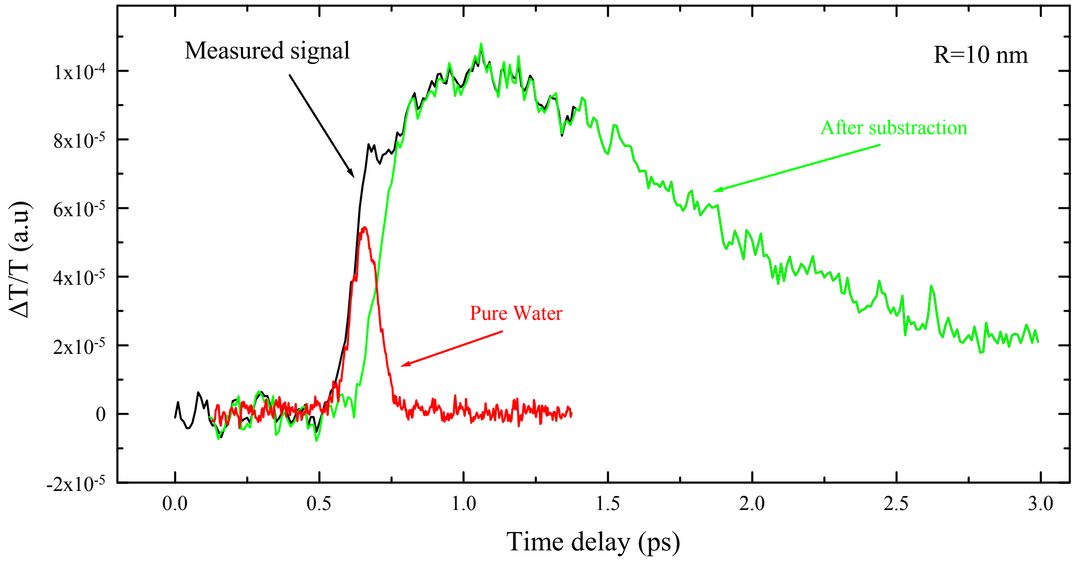

**Figure 6-13** $\frac{\Delta T}{T}$ for a colloidal sample (*R*=10 nm) before (black) and after (green) the correction with the use of a $\frac{\Delta T}{T}$ obtained by distilled water.

results are shown in **Fig. 6-12**. The CC of the pump and probe pulses is also exhibited as obtained with exactly the same experimental conditions. As can be observed, the transient transmission spectrum of pure distilled water is a fully symmetrical curve with the same time profile with the laser pulse. Although the origin of this contribution from water to the signal is not clear, by measuring the contribution of pure water it is possible to isolate it from the contribution of the nanoparticles in the signal. By performing measurements to water samples and measuring the amplitude of the water contribution it is possible to obtain the corrected transient transmission spectra for colloidal nanoparticle samples, as shown in **Fig. 6-13**.

Corrected transmission spectra obtained for three colloidal nanoparticle solutions are shown in **Fig. 6-14**. The trend observed for these samples is the same that can be observed for the nanoparticles embedded in solid matrices. As can be seen in **Fig. 6-14**. nanoparticles with bigger

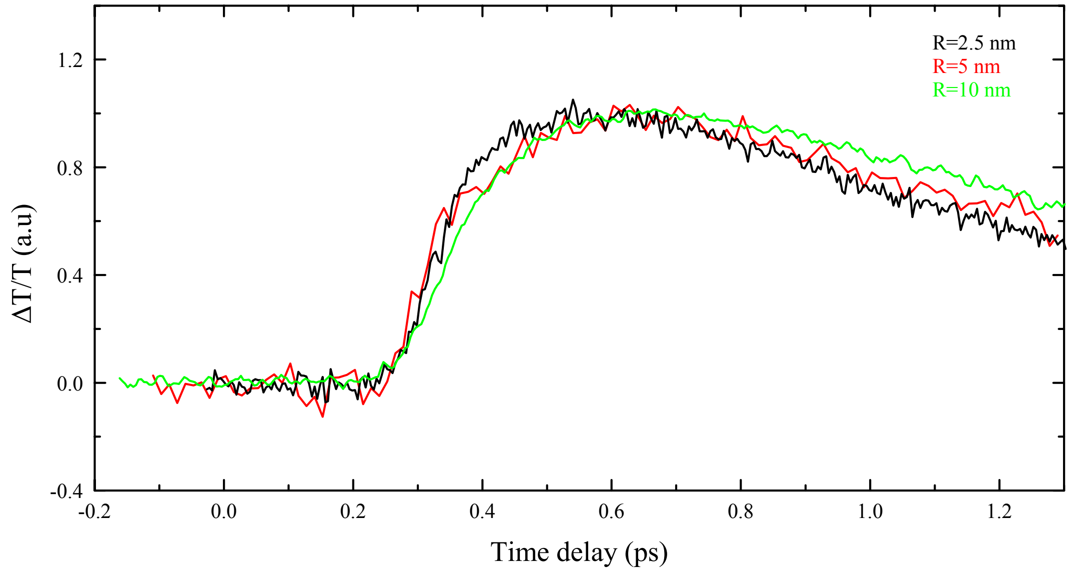

**Figure 6-14** $\frac{\Delta T}{T}$s for colloids after the correction from "water spectra".

sizes exhibit slower rates in the rise of the signal. For the biggest nanoparticles, it becomes difficult to distinguish between their early transient behavior. For the smallest of the three (*R*=2.5 nm) the difference is more clear.

### 6.3.5 Electron-electron thermalization: Discussion

The electron-electron internal thermalization contributes to the signal before as well as after the peak of the signal. **Eq. 6-4** (result of the phenomenological model) is used to reproduce the measured $\frac{\Delta T}{T}$ and extract the characteristic internal thermalization times. In the fitting procedure, the CC duration is measured separately and held fixed in the fitting procedure (parameter *w*). The long scan, single-exponential electron-phonon characteristic interaction time ($\tau_{e\text{-}ph}$) is also measured separately with exactly the same experimental conditions and held fixed during this fitting procedure.

The results concerned with the internal thermalization characteristic time versus the radius of the nanoparticle are summarized in **Fig. 6-15**. As can be seen for big nanoparticle radius, the characteristic time reaches the one for the bulk metal. The time measured for the biggest nanoparticles (*R*=10 nm) is 400 fs which is very close to the time measured for the thin Au film, i.e. 450 fs. As the radius of the nanoparticles becomes smaller, the characteristic time decreases. For the biggest measured nanoparticle, the characteristic time is 400 fs and for the smallest one (*R*<1 nm) it is about 110 fs.

As is seen by our measurements, the characteristic thermalization times for the biggest nanoparticles are practically equal to the ones measured for the Au thin film. The latter can be assumed to exhibit the same electronic behavior with the bulk metal. **DelFatti3** This bulk metal case is the starting point in the interpretation of our results. In the bulk metal case, the thermalization process of the electron population is governed by the collision of conduction band electrons with each other. The initially perturbed electrons redistribute their energy to the other electrons (and phonons). **Voisin2, Voisin, DelFatti3, Sun2** Note here that, no electrons are excited, in the means that their number is constant in the band because of the intraband nature of the procedure. The excited electrons are only gaining energy. The electron density is thus constant in the sample. Two mechanisms are responsible for slowing down the electron-electron scattering rate. The Pauli exclusion principle and the reduced Coulomb interaction among electrons due to screening effects

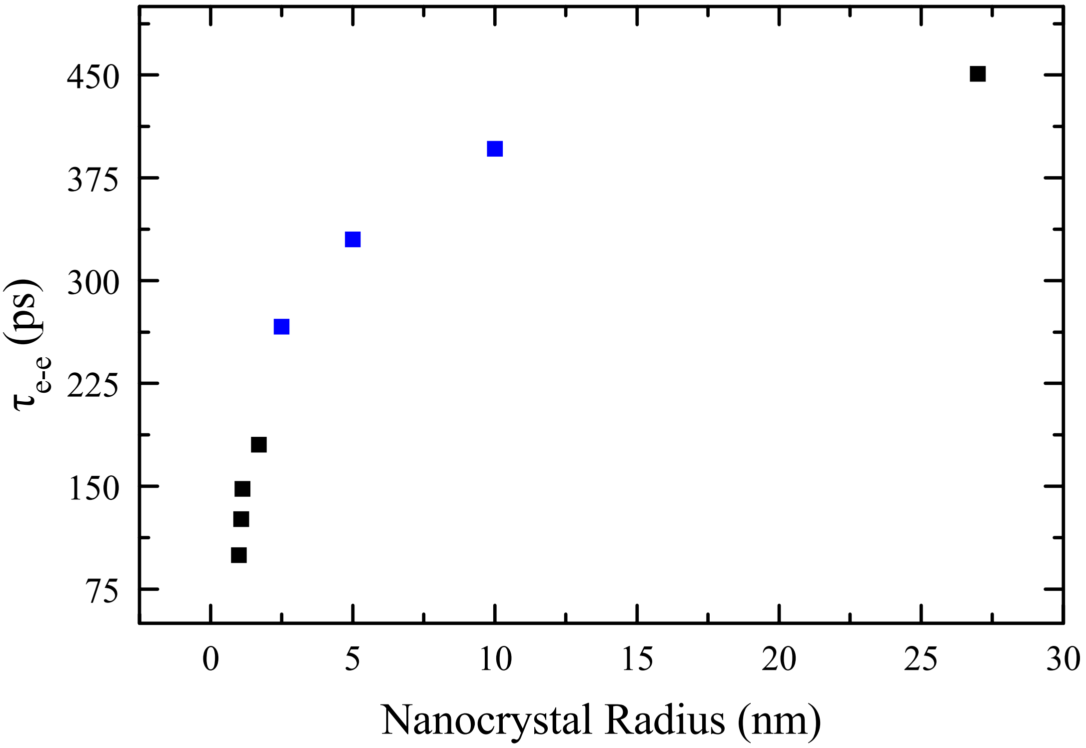

**Figure 6-15** The characteristic electron-electron internal thermalization times versus the radius of the nanocrystals. Blue corresponds to samples in the liquid dielectric host.

**Voisin, Voisin2** as previously discussed in **Chap. 5**.

In order to interpret the electronic behavior of small nanoparticles one has to evaluate the effects of the size reduction and the effects of the confinement in the above mechanisms. As far as the Pauli exclusion principle is concerned, the size reduction is not expected to have any influence or modification on this mechanism. According to the Pauli law, two electrons must scatter into two empty electronic states regardless the size or the confinement of the system. As it is concerned with the screening of the electronic Coulombic interaction, it is expected to be modified by the size reduction. Two facts are responsible for leading to this modification in the Coulombic interaction among the conduction electrons:

- First, the wave functions of the conduction band electrons have been shown **Ekardt** to extend beyond the surface limits of the nanoparticle. This effect, (called the spill-out effect), reduces the electron density in the region inside the nanoparticle and close to its surface and increases the electron density outside the nanoparticle and close to the surface. This way, there exists a non-zero probability in finding an electron out of the nanoparticle leading to a reduction in the inside electronic density.

- Secondly, the d-band electrons are localized to an internal zone away from the vicinity of the surface. This way, the d-band electrons have an insignificant contribution to the screening of the Coulomb interaction of the conduction electrons in a layer close to the surface. **Liebsch, Lerme, Ekardt**

In order to make the above discussion more quantitative on has to evaluate the amplitude of the mentioned effects on the electronic diffusion times. **Eq. 5-36** (see also **Chap. 5**): **Voisin, Voisin2**

$$\gamma_{e-e} \propto n_e^{-5/6} \varepsilon_d^{-1/2}$$

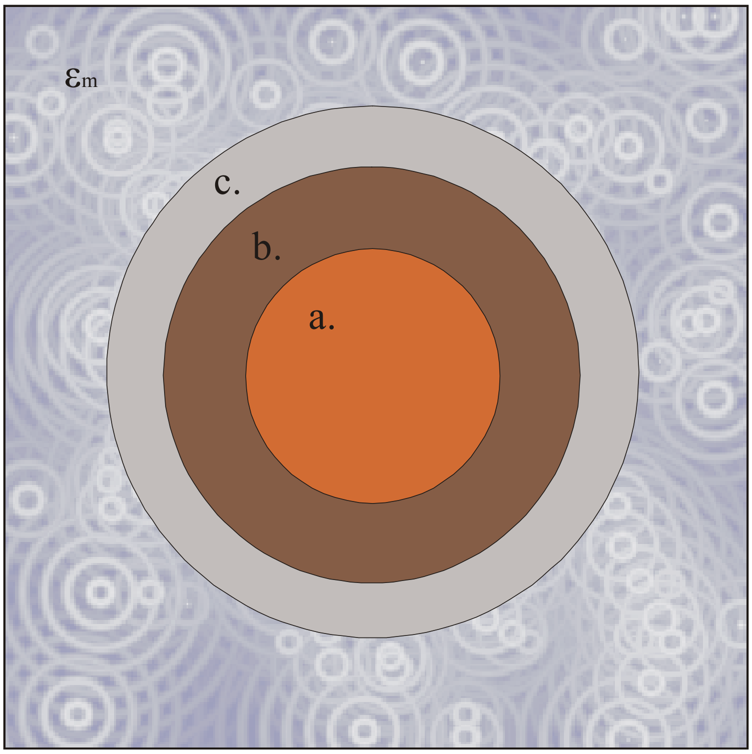

**Figure 6-16** A visualization of the nanocrystal as it is assumed by the model. Area (a) denotes the bulk where the d-band electrons are found. Area (b) is the intermidiate area where the density $n$ and the dilectric constant $\varepsilon$ exhibit a dependence on the distance from the center of the particle. Area (c) is only schematic and is the area outside the nanoparticle where $\varepsilon=\varepsilon_m$.

gave an expression for the electron diffusion rate assuming a constant electron distribution $n_e$ and a constant dielectric constant $\varepsilon_d$ for a bulk metal. Here, $\varepsilon_d$ describes the contribution of the bound d electrons to the screening of the electron Coulombic interaction. Since these two parameters are now considered not to be space-invariant but to have a spatial gradient, then the diffusion rate given by the above equation is assumed to be valid only locally. The total diffusion rate should now be the integrated spatial average of the spatially varying $n_e(r)$ and $\varepsilon_d(r)$. The above can be mathematically depicted as: **Voisin, Voisin2**

$$\bar{\gamma}_{e-e} \propto \frac{1}{N}\iiint_{\Omega} n_e(r)\left[n_e^{-5/6}\varepsilon_d^{-1/2}\right]4\pi r^2 dr \tag{6-6}$$

where $N$ is the total number of electrons on the nanoparticle.

In order to evaluate the scattering rate given by **Eq. 6-6** one must introduce the spatial variations of $n_e(r)$ and $\varepsilon_d(r)$. The last, is due to exclusion of the d-electron from the surface region and have been modeled by W. Ekardt **Ekardt** using a simple model of two concentric spheres **Fig. 6-16**. **Liebsch, Ekardt, Lerme** The nanoparticle is simply described as a sphere of radius $R$ (zone a+b), which correspond to the sphere defined by the ions. (The zone c in **Fig. 6-16** is only schematic. There is no zone c, since we are using the calculated conduction electron density. A third zone has to be introduced for describing the spill out effect if we describe this last effect by a simple model of a constant electron density in a nanoparticle, with a radius larger than the ionic radius.) A smaller concentric sphere inside the former of radius *R-b* represents the region where the d-electrons are present and the dielectric constant takes the value of the bulk metal (zone a). The d-electrons are excluded from the crown of thickness *b* and the dielectric constant takes the value $\varepsilon_d=1$. The value of *b* is set by precisely measuring the size dependence of the SPR frequency in Au and Ag nanospheres. **Lerme**

Outside the sphere of radius *R*, there is a zone where the probability in finding a conduction band electron is non-zero. A thin region at that point can be introduced but it is schematic: finally three different zones have to be considered , the first one which is bulk like, a second one where the d-electrons are absent and the conduction electron density is slightly altered, and a third one, out of the ion core, where only conduction electron are present (spill-out). The calculated by J. Lerme et al. **Lerme** spatial dependence of $n_e(r)$ is depicted in **Fig. 6-17**. This figure shows the non-zero probability for the conduction electrons to spill-out of the spherical nanoparticle region (the surface is denoted as the dotted line). The plotted results are for a Ag nanoparticle radius of 1.9 nm with a similar situation in Au as well.

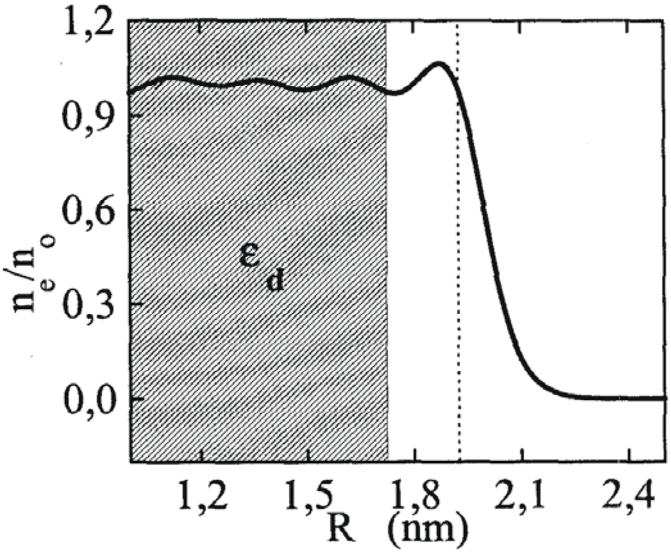

**Figure 6-17** Calculated normalized electron density with respect to the radius for a nanoparticle with *R*=1.9 nm.

Using the above considerations

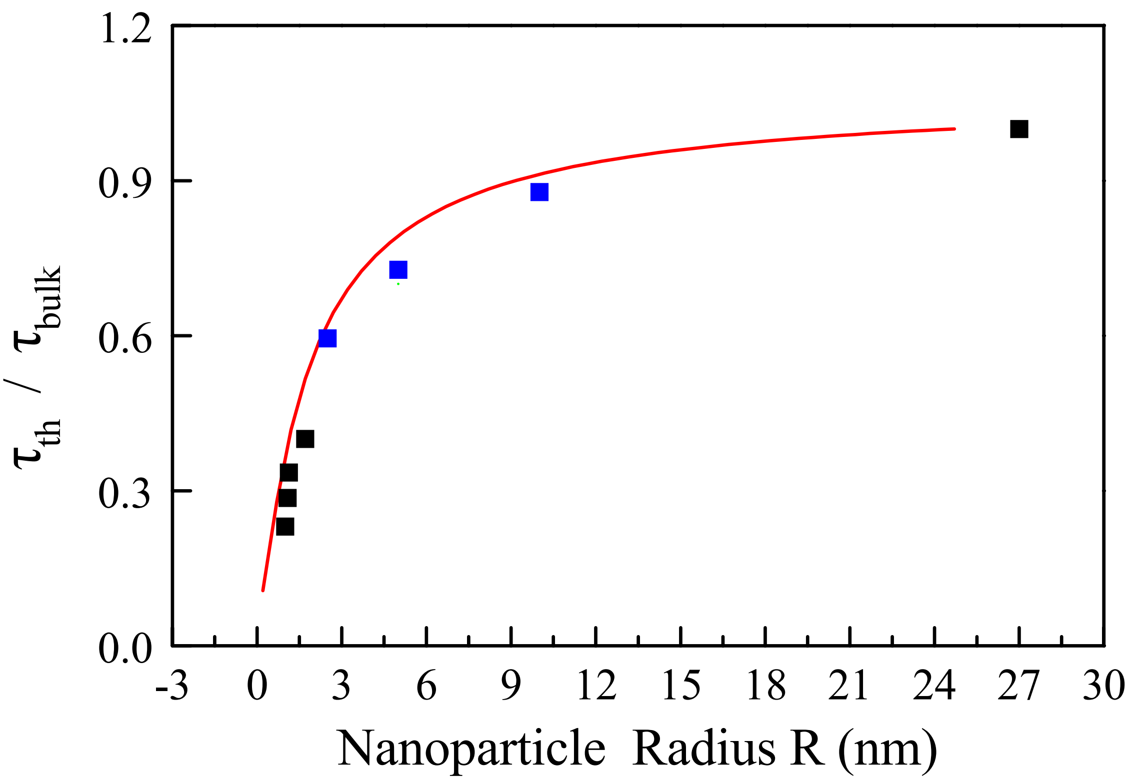

**Figure 6-18** The internal electron thermalization times normalized to the bulk (thin film) value versus the nanoparticle radius *R*. The results of the numerical calculations are also plotted showing the consistency with the experiment.

for the spatial variations for $n_e$ and $\varepsilon_d$, numerical calculations can be performed in order to obtain the electron thermalization rates for Au nanoparticles with radii between 1 nm and 10 nm, following the model developed for Ag. Results of such numerical calculations [Vallee] together with the experimental data are plotted in **Fig. 6-18**. In the numerical evaluations, the value for the thin film (bulk) sample (27 nm) has been fixed to the measured value (450 fs) by the experiment. Though there is no parameter, the numerically calculated curve and the experimental data points are in a very good agreement, as seen in Fig. **6-18**.

Link et al. [Link, Link2] have also attempted to investigate the effects of size to the ultrafast electronic properties of nanoparticles (Au). However, they examined only three nanoparticle sizes: *R*=9, 22 and 48 nm. They observed no trend for the internal electron thermalization with respect to the size. Their measurements (with small deviations of their absolute values with respect to ours) are consistent with ours, since our experiment shows that for nanoparticle radii greater than about 10 nm the internal electron-electron interactions and the corresponding thermalization is comparable if not identical to the bulk (or the thin film). In this sense, there is an agreement between our results and theirs. Stella et al. [Stella] have performed measurements on Tin (Sn) nanoparticles. In their experiments they used three different sizes: $R$=2, 4 and 6 nm. Their results showed no trend for the electron thermalization with respect to the nanoparticle size which is in contradiction to our results. However, they used a degenerate pump and probe setup. In a setup like that, both pump and probe beams having the same wavelength perturb the same energy area around the Fermi level. The probe beam probes the transitions that are “launched” from an already perturbed energy area thus possibly making the results more complex than in the case of a non-degenerate setup (like ours) where the probe beam probes transitions that are “launched” from an unperturbed area zone (d-bands) towards the perturbed area around the Fermi allowing us to monitor the athermal or thermalized character of the last alone, since the “starting point (d-bands) is unperturbed (at equilibrium). Thus in our work the results that are obtained in a relatively big range of nanoparticle sizes, in supplement to recent results obtain for Ag [Voisin2] confirm the observed internal electron thermalization dynamics and extend the validity to a very important noble metal (Au) and in noble metals in general.

A point that must be addressed here concerns the excitation density of the experiment and the corresponding electronic rise in the nanoparticles. In order to have reliable results, one must perform the experiments in the low perturbation regime. In particular, it has been shown [DelFatti4] that for a substantial initial rise in the electronic temperature, the electron-electron interactions and the concomitant internal electron thermalization accelerates due to increased smearing of the Fermi distribution and thus due to relaxation of the limits imposed by the Pauli exclusion principle. DelFatti et al. [DelaFatti4] have shown that there is an observable acceleration of this type for initial increase in the temperature of the electrons higher than about 500 $^{o}$K that results in a deviation of about 40 fs compared to the corresponding thermalization time in the low-perturbation limit. In order to selectively study the dependence of the electron internal thermalization times on the reduced screening effect, one must "freeze" the Pauli exclusion effect, i.e. to make the experiment in an excitation regime where the Pauli exclusion contribution to the electron-electron scattering rates is constant (as stated previously without however, associating the connection of this effect with the excitation density). Elsewise, the results would be unclear and the interpretation more complicated. For the above reasons, we define a temperature rise $\Delta T_{me}$ for the athermal electrons in the sense that $\Delta T_{me}$ is going to be the temperature that is going to characterize the electron Fermi distribution after the internal thermalization. This way we are able to "mimic" the energy (temperature) that is initially stored in the nonthermal electron population. So, taking into account that the electronic heat capacity is temperature dependent, we have:

$$C(T) = \alpha T \tag{6-7}$$

with **Οικονόμου**

$$\alpha = \frac{\pi^2}{2}\frac{Nk_B}{T_F} \tag{6-8}$$

where $N$ is the electron number, $k_B$ the Boltmann constant and $T_F$ the Fermi temperature. For a very small amount of energy $dE$, the corresponding small change in temperature of the system $dT$ will be:

$$dE = C(T)dT = \alpha T dT \Rightarrow \Delta E = \frac{\alpha}{2}\left(T_{\max} - T_0\right) \tag{6-9}$$

where $T_{max}$ is the equivalent maximum temperature of the electrons and $T_0$ is the initial electron temperature before perturbation (300 $^{o}$K). Therefore:

$$\Delta T_{me} \equiv T_{\max} - T_0 = \left( \frac{2\Delta E}{\alpha} + T_0^{\,2} \right)^{1/2} - T_0 \qquad (6\text{-}10)$$

Here, *ΔE* is the energy that is initially given by the laser pump pulse in the nanoparticle. For the samples we investigated the volume fraction of the nanoparticles is very small (typically $10^{-3}$) resulting in an average absorption of less than one photon per nanoparticle. Thus, the energy initially stored in a nanoparticle that happens to absorb is solely determined by the pump photon energy $\Delta E = \hbar\omega$. In our case, typically a pump photon wavelength is of $\lambda$=1050 nm or equivalently *ΔE*=1.18 eV. Taking into account the volume of the nanoparticles $V = \frac{4\pi}{3} R^3$, the effective mass of electrons in Au $m$=$9.1\times10^{-31}$ kgr (=$m_0$ :mass of a free electron) and the Au electron density

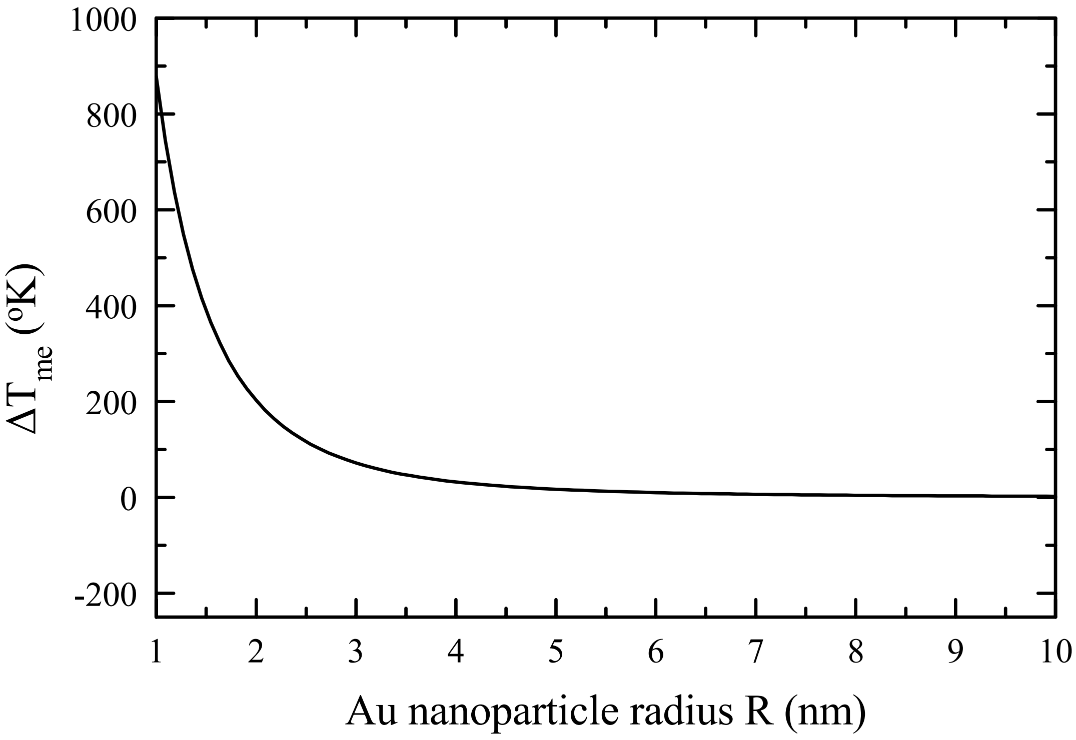

**Figure 6-19** The maximum change in the equivalent temperature of the non-thermalized electron population as a function of the nanoparticle radius.

$n$=5.9×$10^{28}$ $m^{-3}$, we calculate and plot in **Fig. 6-19** the results of the above discussion for the equivalent maximum electron temperature rise versus the nanoparticle radius. As can be seen by **Fig. 6-19**, only for nanoparticles close to 1 nm and lower, the temperature rises above 500 $^{o}$K and the thermal contribution to the characteristic thermalization time is an additional about 40 fs (which is not a very big error – it is in the limits of our setup time resolution). Therefore, for the rest of the examined sizes and especially for $R$>1.7 nm the results are quite reliable. For the very small nanoparticles one would expect a further acceleration of the electron-electron scattering rates due to the reasons already discussed and in this regime, in order to make a better model, one has to calculate the effects of the relaxation of the Pauli blocking as well and not only the effects of the screening reduction.

There exists one report in the literature [Bigot] for experiments in the high perturbation regime (for Cu) but in that work only one nanoparticle size is examined and therefore we are not able to compare our results in the low-perturbation regime with others in the high-perturbation regime.

Returning back to **Fig. 6-18** we can see that only a very small deviation is observed for the very small nanoparticle sizes (if not any) in the sense that the experimental data are a little bit shifted to the right of the numerical curve. Such a deviation (that is also observed in Ag [Voisin2]) would be attributed to the fact that for very small radii, the number of electrons is very small and the electronic temperature rise becomes more significant as discussed previously. In order to be more reliable in this size range and lower, one has to perform measurements with even less excitation density (longer wavelengths), however the trend given even for these small nanoparticles is still clear. Furthermore, for the examination of smaller size-particles, one has to take into account that the number of atoms in the particle reduces so much that approaches the quantum confinement vicinity. Experiments in this regime will be very interesting and will need further theoretical support in order to account for these quantum size effects as well.

## 6.4 Conclusions

The purpose of work is to study the impact of confinement on the electron interactions in Au and to study the transition from the bulk metal to the molecular behavior.

- The results give the size dependences of the electron-electron and electron-phonon times and show the fact that they are environment independent.
- A model has been presented for the electron-electron reduction of the screening close to the surface. For the electron-phonon energy exchanges the results are not yet clear, but a clear trend, similar to the electron-electron one has been observed.
- The novelty of this work is that for electron-electron scattering, results are only obtained before in Ag, and it is important to investigate an other noble metal, to see if the size dependences are consistent. And they are.
- Concerning the electron-phonon interaction, there are many results in different metals, but the size dependence is not clear, even experimentally, i.e., some authors say that there is no size variation, others that it is increasing and others that it is decreasing with size. Environment dependent electron-phonon interaction time are also reported. Low perturbation regime measurements in Ag show a reduction of the interaction time with size and no environment effect for the electron internal thermalization procedure. It is very important to confirm these results in Au because this consistency extends the validity of the observed trends and the used models to noble metal nanoparticles in general

## 6.5 References

**Ahmadi** T. S. Ahmadi, S. L. Logunov and M. A. El-Sayed, J. Phys. Chem. **100**, 8053 (1996).

**Bigot** J.-Y. Bigot, J.-C. Merle, O. Cregut, and A. Daunois, Phys. Rev. Lett. **75**, 4702 (1995).

**DelFatti** N. Del Fatti, C. Flytzanis and F. Vallee, Appl. Phys. B **68**, 433 (1999).

**DelFatti2** N. Del Fatti, F. Vallee, C. Flytzanis, Y. Hamanaka, and A. Nakamura, Chem. Phys. **251**, 215 (2000).

**DelFatti3** N. Del Fatti, R. Bouffanais, F. Vallee, and C. Flytzanis, Phys. Rev. Lett. **81**, 922 (1998).

**DelFatti4** N. Del Fatti, C. Voisin, M. Achermann, S. Tzortzakis, D. Christofilos, and F. Vallee, Phys. Rev. B **61**, 16956 (2000).

**Ekardt** W. Ekardt, Phys. Rev. B **29**, 1558 (1984).

**Fann** W. S. Fann, R. Stortz, H. W. K. Tom, and J. Bokor, Phys. Rev. Lett. **68**, 2834 (1992).

**Fann2** W. S. Fann, R. Stortz, H. W. K. Tom, and J. Bokor, Phys. Rev. B **46**, 13592 (1992).

| | |
|---|---|
| **Flytzanis** | C. Flytzanis, F. Hache, M. C. Klein, D. Ricard, and P. Roussignol, "Nonlinear optics in composite materials" in Progress in optics XXIX, ed. by E. Wolf, Elsevier Science Publishers (1991) pp. 321. |
| **Halte** | V. Halte, J.-Y. Bigot, B. Palpant, M. Broyer, B. Prevel, and A. Perez, Appl. Phys. Lett. **75**, 3799 (1999). |
| **Hamanaka** | Y. Hamanaka, A. Nakamura, S. Omi, N. Del Fatti, F. Vallee, and C. Flytzanis, Appl. Phys. Lett. **75**, 1712 (1999). |
| **Hodak** | J. H. Hodak, I. Martini and G. Hartland, J. Phys. Chem. B **102**, 6958 (1998). |
| **Hodak2** | J. Hodak, I. Martini and G. V. Hartland, Chem. Phys. Lett. **284**, 135 (1998). |
| **Inouye** | H. Inouye, K. Tanaka, I. Tanahashi, and K. Hirao, Phys. Rev. B **57**, 11334 (1998). |
| **Lerme** | J. Lerme, B. Palpant, B. Prevel, M. Pellarin, M. Treilleux, J. L. Vialle, A. Perez, and M. Broyer, Phys. Rev. Lett. **80**, 5105 (1998). |
| **Liebsch** | A. Liebsch, Phys. Rev. B **48**, 11317 (1993). |
| **Link** | S. Link and M. A. El-Sayed, J. Phys. Chem. B **103**, 8410 (1999). |
| **Link2** | S. Link, C. Burda, Z. L. Wang, and M. A. El-Sayed, J. Chem. Phys. **111**, 1255 (1999). |
| **Logunov** | S. L. Logunov, T. S. Ahmadi, M. A. El-Sayed, J. T. Khoury, and R. L. Whetten, J. Phys. Chem. B **101**, 3713 (1997). |
| **Milani** | P. Milani and W. A. de Heer, Rev. Sci. Instrum. **61**, 1835 (1990). |

**Nisoli** M. Nisoli, S. Stagira, S. De Silvestri, A. Stella, P. Tognini, P. Cheyssac, and R. Kofman, Phys. Rev. Lett. **78**, 3575 (1997).

**Οικονόμου** Ε. Ν. Οικονόμου, Ασκήσεις Στατιστικής Φυσικής, Πανεπιστημιακές Εκδόσεις Κρήτης, 1994.

**Perez** A. Perez, P. Melinon, V. Dupuis, P. Jensen, B. Prevel, J. Tuaillon, L. Bardotti, C. Martet, M. Treillaux, M. Broyer, M. Pellarin, J. L. Viale, B. Palpant, and J. Lerme, J. Phys. D: Appl. Phys. **30**, 709 (1997).

**Perner** M. Perner, T. Klar, S. Grosse, U. Lemmer, G. von Plessen, W. Spirkl, and J. Feldmann, J. Lumin. **76-77**, 181 (1998).

**Perner2** M. Perner, P. Bost, U. Lemmer, G. von Plessen, J. Feldmann, U. Becker, M. Mennig. M. Schmitt, and H. Schmidt, Phys. Rev. Lett. **78**, 2192 (1997).

**Roberti** T. W. Roberti, B. A. Smith and J. Z. Zhang, J. Chem. Phys. **102**, 3860 (1995).

**Roth** J. Roth, Techniques in Immunocytochemistry, p. 217-284.

**Schoenlein** R. W. Schoenlein, W. Z. Lin, J. G. Fujimoto, and G. L. Easley, Phys. Rev. Lett. **58**, 1680 (1987).

**Smith** B. A. Smith, D. M. Walters, A. E. Faulhaber, M. A. Kreger, T. W. Roberti, and J. Z. Zhang, J. Sol-Gel Sci. Techn. **9**, 125 (1997).

**Smith2** B. A. Smith, J. Z. Zhang, U. Giebel, and G. Schmid, Chem. Phys. Lett. **270**, 139 (1997).

**Stella** A. Stella, M. Nisoli, S. De Silvestri, O. Svelto, G. Lanzani, P. Cheyssac, and R. Kofman, Phys. Rev. B **53**, 15497 (1996).

| | |
|---|---|
| **Sun** | C.-K. Sun, F. Vallee, L. Acioli, E. P. Ippen, and J. G. Fujimoto, Phys. Rev. B **48**, 12365 (1993). |
| **Sun2** | C.-K. Sun, F. Vallee, L. H. Acioli, E. P. Ippen, and J. G. Fujimoto, Phys. Rev. B **50**, 15337 (1994). |
| **Tokizaki** | T. Tokizaki, A. Nakamura, S. Kaneko, K. Uchida, S. Omi, H. Tanji, and Y. Asahara, Appl. Phys. Lett. **65**, 941 (1994). |
| **Uchida** | K. Uchida, S. Kaneko, S. Omi, C. Hata, H. Tanji, Y. Asahara, A. J. Ikushima, T. Tokisaki, and A. Nakamura, J. Opt. Soc. Am. B **11**, 1236 (1990). |
| **Vallee** | Private communication with Fabrice Vallee and Cristophe Voisin. |
| **Vialle** | J. L. Vialle, B. Baguenard, A. Bourgey, E. Cottancin, J. Lerme, B. Palpant, M. Pellarin, F. Valadier, and M. Broyer, Rev. Sci. Instrum. **68**, 2312 (1997). |
| **Voisin** | C. Voisin, N. Del Fatti, D. Christofilos, and F. Vallee, J. Phys. Chem B **105**, 2264 (2001). |
| **Voisin2** | C. Voisin, D. Christofilos, N. Del Fatti, F. Vallee, B. Prevel, E. Cottancin, J. Lerme, M. Pellarin, and M. Broyer, Phys. Rev. Lett. **85**, 2200 (2000). |
| **Zhang** | J. Z. Zhang, Acc. Chem. Res. **30**, 423 (1997) and references therein. |

# Chapter 7 Summary

This work dealt with the investigation of the effects of structure on the ultrafast electrnonic properties of semiconductors like GaAs and the relevant AlGaAs alloy and Au nanocomposites.

Despite the extensive work that has performed in LTG-GaAs, the ultrafast electronic properties are not yet clear. Although that it is now well established that the inclusion of As spheres with nanometric dimensions in the GaAs host is responsible for the ultrafast electronic behavior of the material, it is not yet known what exactly is the law that governs the contribution of the As precipitate characteristics on the electron trapping times. This work proved that the electron behavior is governed by diffusion mediated trapping on the surfaces of the As precipitates and that the electron trapping times depend on both the As precipitate size and density as it is theoretically predicted by the solution of the diffusion equation, when it is applied for this certain system. This work gives a powerful tool in the engineering field in fabricating ultrafast optoelectronic devices that are based on this material.

The ultrafast electronic properties of alloy semiconductors like AlGaAs are much less studied yet. This work uses AlGaAs as a test material to study whether the phenomena that are observed in its relevant GaAs semiconductor, also apply here. It is found that the same mechanism governs the ultrafast electronic trapping as in the GaAs case. Deviations only in the values of the trapping times are observed that are due to the difference in the lattice structure. The observations made for AlGaAs have their unique importance, distinct from GaAs, because with the variation of the Al mole fraction in the semiconductor, a tunability of the material to a specific desired wavelength is possible, and so, engineers now have a unique material to use in the fabrication of ultrafast optoelectronic devices because of its now known ultrafast electronic trapping behavior.

Apart from the influence of the nanometric scale inclusions of semiconductors to their electronic properties, it is of technological as well as fundamental interest to study the effect of the size reduction to the electronic properties inside the nanoparticle. For this reason, and for their unique importance in optoelectronics, nanoparticles of Au are also studied in this work. Although that study of the ultrafast thermalized electron dynamics has been carried out before in nanoparticles, very little is known for the internal electron thermalization and only for Ag. Thus, this work is needed in order to verify previous results in Ag and to extend the validity of the observations to noble metals in general. The electronic properties of Au nanoparticles are found to depend on the confinement of the system. This confinement in nanometric dimensions is found to enhance (accelerate) the internal electron thermalization and a model is presented to describe the enhancement. Also, the electron-lattice thermalization is found to accelerate with the reduction of the particle dimensions but the interpretation is not yet clear and more theoretical work is needed. These observations made for Au nanoparticles are useful because now with the intentional alteration of the dimensionality of the system, engineers have the ability to control the optical and ultrafast electronic properties of the material to meet the needs of the optelectronic device fabrication industry and nanotechnology.

Apart from the study of ultrafast electronic dynamic phenomena in matter, this thesis proves the applicability of tunable ultrafast laser pulsed sources and of the ultrafast pump and probe spectroscopy in the selective investigation of very fast phenomena and demonstrates how such techniques can be manipulated and optimized in order to meet a specific experiment’s requirements.